Tuning of Scattering Properties by Periodic Modulation

Diplomarbeit
in
Theoretischer Physik

von
Christoph Dauer

durchgeführt am
Fachbereich Physik
der Technischen Universität Kaiserslautern

unter Anleitung von
Prof. Dr. Sebastian Eggert

April 2018

Abstract

Periodic driving of quantum systems gives rise to novel and exciting phenomena. In recent experiments the interaction of particles in a Bose-Einstein condensate has been altered time periodically and as a result the excitation of collective modes has been observed without changing the condensate trap [1]. Furthermore, the emergence of the collective emission of matter-wave jets from a driven condensate has been detected [2].

The aim of this thesis is to observe, how the scattering of particles can be tuned by periodic driving. Therefore, we investigate the two-body problem with a time-periodic interaction potential [3–5]. By the use of Floquet theory the Floquet-partial wave expansion is derived. It is capable of calculating cross sections and steady-state wave functions for scattering by a time-periodic potential. We apply this method to a sinusoidally driven contact potential, which describes the two-body interaction of quantum particles in the regime of s-wave scattering. In this case it is possible to map the driven scattering problem on a recursion relation connecting different Fourier components of the steady-state wave function. By solving this recursion we obtain a time-averaged scattering amplitude and observe resonances, which permit to tune this scattering amplitude to very large positive or negative values, signalling strong enhancement of scattering induced by time-periodic driving. The width of these resonances can be tuned by the driving strength, while the frequency of the drive allows one to control the actual enhancement of scattering. We find position and width of these resonances for a large range of driving strengths and spot that inelastic scattering is suppressed in their vicinity. We can explain these resonances by the phenomenon of Fano resonance involving a bound state in the continuum. In addition, we find a Kramers-Kronig like relation connecting real and imaginary part of the time-averaged scattering amplitude and demonstrate that the shape of these resonances can be approximately described by a two-channel model. Using the Floquet-partial wave expansion in its full extend, we are finally able to overcome the restriction of sinusoidal driving and investigate the influence of higher-Fourier components of the driven contact potential on the resonances.

A possible experimental realisation of our model is a periodically driven magnetic Feshbach resonance [3], which grants the creation of resonances at magnetic field strengths beside the actual magnetic Feshbach resonance. Our method is able to predict the enhancement of scattering in this setting in a wide range of driving strengths.

Zusammenfassung

Periodisch getriebene Quantensysteme weisen neuartige und interessante Phänomene auf. In verschiedenen Experimenten wurde die Wechselwirkungsstärke von Teilchen in einem Bose-Einstein Kondensat zeitlich moduliert [1,2]. Dies führt einerseits zur Anregung kollektiver Moden, ohne dass Änderungen an der Falle vorgenommen werden müssen [1], andererseits wurde das Auftreten kollektiver Emissionen von Materiewellen beobachtet [2].

Das Ziel dieser Arbeit besteht darin, zu untersuchen, wie die Streuung von Teilchen mit Hilfe zeitlich periodischen Treibens verändert werden kann. Daher wird das Zweikörperproblem mit einem zeitlich periodisch modulierten Wechselwirkungspotential [3–5] betrachtet. Mit Hilfe der Floquet-Theorie wird die Floquet-Partialwellenentwicklung hergeleitet, welche die Berechnung von Streuquerschnitten und Wellenfunktionen für beliebig zeitlich periodisch modulierte Potentiale ermöglicht. Diese Methode wird auf ein harmonisch moduliertes Kontaktpotential angewendet, welches die Zweikörperwechselwirkung in der Näherung der s-Wellen Streuung beschreibt. In diesem Fall ist es möglich, das getriebene Streuproblem auf eine Rekursionsrelation zu transformieren. Die Lösung jener Rekursionsrelation, welche verschiedene Fourierkomponenten der Wellenfunktion verknüpft, erlaubt die Berechnung der zeitgemittelten Streuamplitude. Es treten Resonanzen auf, welche es ermöglichen, die Streuamplitude zu sehr großen positiven oder negativen Werten einzustellen und dadurch zu einer starken Erhöhung der Streurate zu führen. Die Breite dieser Resonanzen kann mit Hilfe der Treibamplitude eingestellt werden, während die Treibfrequenz die tatsächliche Erhöhung der Streuamplitude bestimmt. Wir ermitteln Position und Breite dieser Resonanzen für einen großen Bereich von Treibamplituden und beobachten, dass inelastische Streuung in der Nähe der Resonanz unterdrückt ist. Das Auftreten der Resonanzen wird durch das Phänomen der Fano-Resonanz erklärt. Zusätzlich stellen wir fest, dass Real- und Imaginärteil der Streuamplitude durch eine Relation, die den Kramers-Kronig Beziehungen ähnelt, verknüpft sind und zeigen, dass die Form der Resonanz durch ein Zweikanalmodell angenähert werden kann. Unter Verwendung der Floquet-Partialwellenentwicklung sind wir letztendlich in der Lage, die Restriktion des sinusartigen Treibens zu verlassen und die Auswirkungen höherer Fourierkomponenten des zeitlich periodisch modulierten Kontaktpotentials zu untersuchen.

Eine mögliche experimentelle Realisierung unseres Modells ist die periodisch getriebene magnetische Feshbach-Resonanz [3]. Diese erlaubt die Erhöhung der Streuamplitude in einem weiten Bereich um die eigentliche magnetische Feshbach-Resonanz. Unsere Methode erlaubt die Vorhersage von Resonanzen für ein großes Spektrum an Treibamplituden.

Contents

1. Introduction

Although Floquet theory is well established in research dealing with atoms in strong laser fields [6–10], it is in the recent time introduced to various areas of physics in order to describe and propose periodically driven systems with interesting and novel properties. We therefore give in Section 1.1 an overview of driven physical systems and how properties of these systems can be tuned by periodic driving. Section 1.2 provides a short introduction into the tuning of the inter-particle interactions in ultracold quantum gases. Section 1.3 combines both previous Sections and gives a short insight into the setting of our thesis. Section 1.4 is devoted to the outline of the thesis.

1.1. Periodic Driving in Physical Systems

Periodic driving of physical systems gives rise to exciting novel phenomena. A simple and impressing example is the Kapitza pendulum [11–13]. As drawn in Figure 1.1, it consists of a rigid pendulum possessing a pivot, which vibrates in vertical direction. If the vibration is performed with a large enough frequency and amplitude, a counter intuitive behaviour is observed: The upper equilibrium, where the pendulum is inverted, becomes stable and the lower unstable. Kapitza understood this behaviour by separating the angular motion in a fast oscillation and a slow movement. Averaging out the fast motion leads to an effective potential stabilizing the slowly varying angular degree of freedom in the upper equilibrium.

Also in quantum mechanics periodic driving is used in order to induce a behaviour, which is not present in the static case. A simple band structure can be described by the tight-binding model [14] on a lattice. It consists of an array of lattice sites, which are connected by the hopping amplitude J. The hopping amplitude J can be seen as the matrix element for a transition between neighbouring lattice sites. If a time-periodic field with strength $\mathcal{E}$ and frequency ω, which is large in comparison to the bandwidth of the lattice, is applied, the driven system behaves like a static lattice with effective hopping amplitude [15]

$$J_{\text{eff}} = J\mathcal{J}_0\left(\frac{\mathcal{E}}{\hbar\omega}\right), \tag{1.1}$$

which is normalised by the Bessel function of order zero $\mathcal{J}_0(x)$. The effective hopping amplitude depends explicitly on the driving strength $\mathcal{E}$ and driving frequency ω and can therefore be tuned by periodic driving. This has been exploited in order to investigate the quantum phase transition between a Mott-insulator and a superfluid state of a Bose-Einstein condensate loaded in an optical lattice [16–18] in theory and in experiment. The quantum phase transition can be achieved reversibly

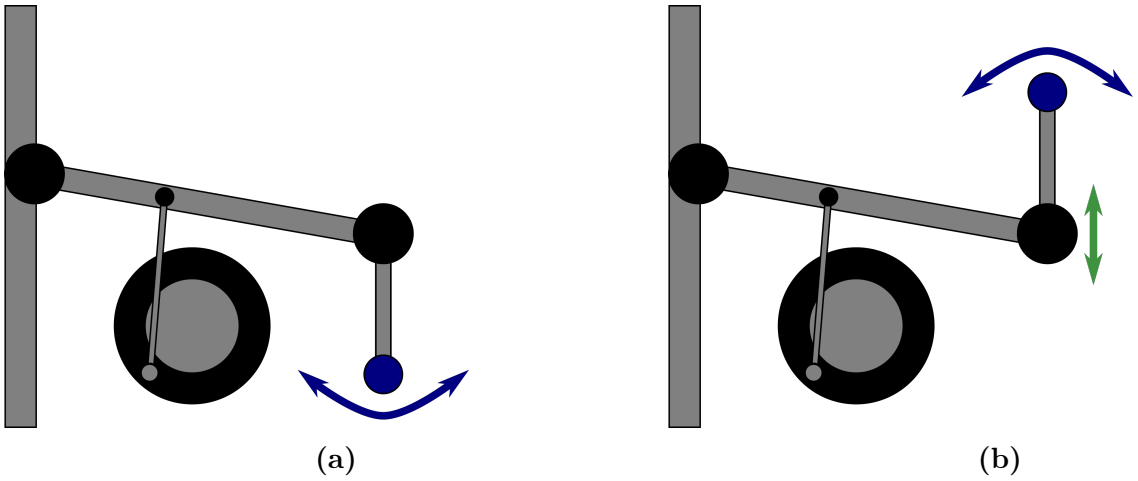

Figure 1.1.: Sketch of the Kapitza pendulum. The rigid pendulum is drawn as a lever with a blue bob, while the suspension can be driven by an eccentric mechanism. Both pivots are drawn as a black circle. In panel **(a)** we show the case without periodic driving, where the lower equilibrium is stable. It is indicated in this Figure by a blue arrow. In panel **(b)** the suspension of the pendulum is altered periodically in vertical direction and the upper equilibrium becomes stable.

by ramping the strength of the effective hopping amplitude. If the argument of the Bessel function reaches one of its zeros, the effective hopping amplitude even vanishes. As in this case particles cannot hop between neighbouring sites, a wave packet will become localised. This effect of dynamic localisation was predicted by Dunlap and Kenkre [19] and experimentally realised in semiconductor superlattices [20], photonic wave-guide arrays [21, 22] and Bose-Einstein condensates in driven optical lattices [23–25]. If the driving is tuned in the right way, the effective hopping amplitude can even become negative and therefore realise a state with negative effective mass [17]. A more complicated driving scheme applied to a hexagonal optical lattice leads to the realisation of the Haldane model for ultracold fermions [26] and the observation of dynamical vortices, which are related to the topology of the driven lattice [27]. One can even go further and induce artificial gauge fields by the periodic modulation of a lattice [28–30].

All the aforementioned examples have in common, that the driving frequency is larger than the energy scales of the corresponding static problem and that their dynamics is governed by an effective Hamiltonian. In the lowest order of the so called Magnus expansion [15], this effective Hamiltonian is the time average of the time-dependent one. But for lower driving frequencies the situation becomes more involved. The method of choice in order to treat periodically driven systems in general is Floquet theory [31–33]. It is named after the French mathematician Gaston Floquet (1848-1920) [34], who came up with a theorem characterizing the solution of ordinary differential equations having time periodic coefficients [35]. Introduced to quantum physics [36], Floquet theory yields the description of time periodic quantum systems in terms of steady states and is capable of investigating any time-periodic system exactly.

Instead of restricting ourselves to the high frequency limit, we consider in this thesis a periodi-

cally driven two-body problem without any restrictions on the driving frequency. We use Floquet theory in order to derive a scattering theory being capable of dealing with time-periodic scattering potentials and calculating time-averaged scattering cross sections. As one possible experimental realisation of our findings lies in the field of ultracold quantum gases, we first give a brief introduction to those and specialise to the tuning of interactions in this setting.

1.2. Tuning the Interaction in Ultracold Gases

Ultracold quantum gases allow a huge amount of experimental controllability [37, 38]. Loaded into an optical lattice, they are used to implement models of solid state physics and provide a playground for the search of new materials [39]. The controllability of ultracold quantum gases is not limited to external potentials like optical lattices, also the interaction between particles can be tuned. In the case of the low energy physics of an ultracold quantum gas, the interaction between two particles is fully characterised in terms of the scattering length a, whose absolute square is proportional to the total cross section. Therefore the scattering length can be viewed as a length scale of the cross-sectional area. Large cross sections correspond to strong inter-particle interactions and are obtained for large scattering lengths. The method of choice in order to obtain experimental control of the scattering length in an ultracold gas experiment is the use of a Feshbach resonance. In case of the widely used magnetic Feshbach resonance a magnetic field is adapted in order to change the energy of a molecular bound state in such a way, that it is resonant with a scattering state of the two colliding particles. As the scattering state couples with the bound state, the inter-particle interaction is changed. The resulting interaction strength and, thus, the scattering length can be altered by adjusting the strength of the magnetic field. The tuning of the interaction using a Feshbach resonance has a wide range of application in ultracold quantum gases. For example, they are used in the controlled attainment of a Bose-Einstein condensate [38, 40, 41], the observation of the BEC-BCS crossover [42–44] and the production of ultracold molecules [45, 46] using an additional time periodic field. Several experiments even included a time-periodic interaction strength, which lead to the excitation of collective modes in a Bose-Einstein condensate without altering the trapping potential [1, 47, 48] and the observation of the collective emission of matter-wave jets from a Bose-Einstein condensate [2] .

1.3. Tuning the Interaction Strength by Periodic Driving

Several theoretical works [3, 4] show that if an inter-atomic potential is driven time-periodically, scattering can be enhanced by tuning the driving frequency near a resonance. Smith [3] proposed a new method for controlling the scattering length by applying a time-dependent magnetic field in the vicinity of a magnetic Feshbach resonance. Also in this thesis we combine both fields of time-periodic driving and the tuning of interactions and investigate the scattering of quantum particles by a time-periodic potential in the low energy limit.

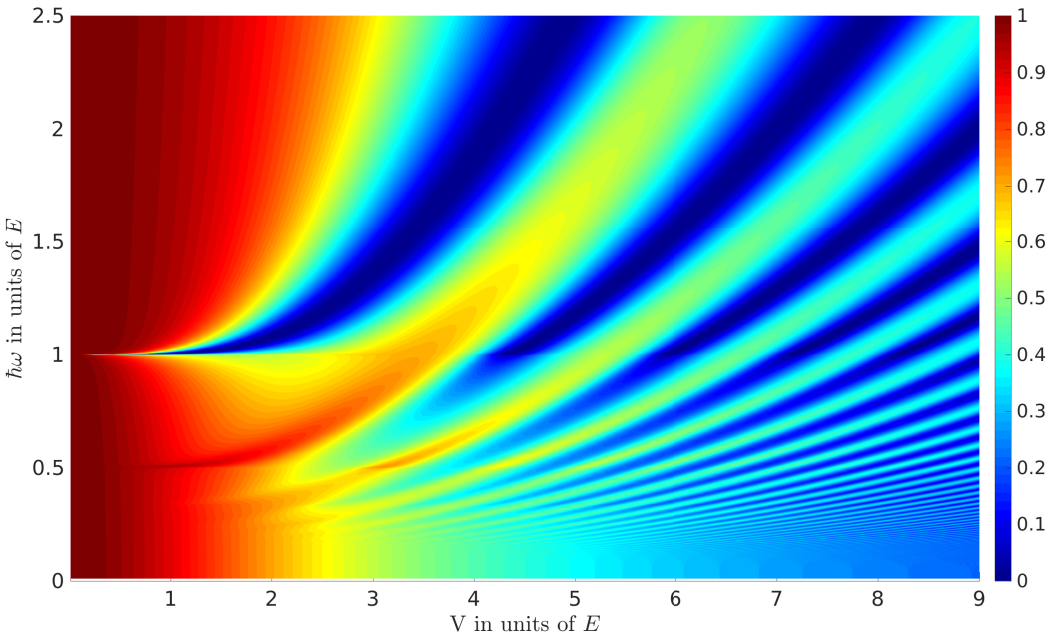

Figure 1.2.: Plot of the time-averaged transmission coefficient of model (1.2) in dependence of the driving frequency $\hbar\omega$ and the driving strength V. The incoming particle is assumed to have the energy E.

Our work originates in a related subject, namely the tunnelling of a quantum particle through a periodically driven barrier in one dimension. In the work of Reyes et. al [49] a Dirac-delta function is considered as a barrier and the problem can be described by the Hamiltonian

$$H(x,t) = -\frac{\hbar^2}{2m}\frac{\partial^2}{\partial x^2} - V\cos(\omega t)\delta(x). \tag{1.2}$$

Here m denotes the particle mass, V the driving strength and ω the driving frequency. With the usage of Floquet theory the time-averaged transmission coefficient is calculated. The result is shown in Figure 1.2. Instead of being finite for all barrier strengths V as for a static barrier, in the driven case there exist lines in the ω-V plane, where the transmission coefficient vanishes exactly. Interestingly, if the frequency is tuned in the right way, this effect occurs even for infinitesimally small barrier amplitudes V. Reyes et al. named this finding a quantum resonance catastrophe and explained the vanishing of the transmission coefficient by a so-called Fano resonance [50, 51].

Motivated by the rich and interesting findings in the one dimensional driven tunnelling problem, the goal of this thesis is to generalise model (1.2) to three dimensions and to observe, under which circumstances resonances occur in the three dimensional case. Instead of calculating a transmission coefficient, the scattering length is the suitable parameter for the new setting. We combine Floquet theory with static scattering theory in order to derive the Floquet-partial wave expansion, which is capable of calculating cross sections and steady state wave functions of a general time-periodic potential. We apply this theory to the contact potential, which expands the Dirac-delta potential

to three dimensions, and observe the emergence of scattering resonances. Those are manifested by a diverging scattering length instead of a vanishing transmission coefficient and allow us to control the scattering length and therefore the inter-particle interaction by time-periodic driving. We are able to describe the shape of these resonances by a simple formula and determine position and width for almost arbitrary driving frequencies.

A possible experimental realisation of our findings is a magnetic Feshbach resonance with a time-periodic magnetic field, which is applied in its vicinity [3]. This driven Feshbach resonance can be induced in wide range of magnetic field strengths and the enhancement can be controlled by the driving frequency. This allows a larger experimental flexibility, as the magnetic field can be set to values away from the actual resonance without loosing the enhancement of scattering. Additionally, our theory can be applied to systems, where a Feshbach resonance is not yet present. This would allow the tuning of the interaction strength in a case, where it is not be possible without periodic driving.

1.4. Outline of the Thesis

This thesis combines the field of scattering physics and time-periodic forcing. While Chapters 2-4 are reviewing relevant topics, Chapters 5-8 contain own work. As an introduction, we review in Chapter 2 the scattering theory for a quantum particle in a time-independent potential, which is able of treating the two-body problem of interacting particles. We discuss how scattering quantities like the scattering amplitude and cross section are calculated using the partial wave expansion.

We apply in Chapter 3 the scattering theory in the context of Feshbach resonances. After a theoretical explanation for the emergence of Feshbach resonances, we survey both experimental realisation and theoretical prediction of those in the regime of ultracold quantum gases.

The focus of Chapter 4 lies on time-periodically driven systems. We introduce Floquet theory, which is capable of solving the time-dependent Schrödinger equation exactly for arbitrarily large driving strengths and frequencies. A key feature of this method is, that it allows us to map the time-periodic Schrödinger equation to a static one in a larger Hilbert space and therefore to calculate steady states.

Using the prior Chapters as fundamentals, we derive in Chapter 5 the Floquet-scattering theory. It is capable of describing the scattering of a quantum particle by a time-periodic potential. We define effective scattering quantities by time averaging and derive the Floquet-partial-wave expansion for calculating these quantities. Similar to Chapter 4, the scattering by a time-periodic potential can be seen as the scattering by a static one in a more complicated Hilbert space. We finish this Chapter by investigating the low energy limit of Floquet scattering.

Chapter 6 applies Floquet-partial wave expansion to the contact interaction, which is able to describe the interaction of ultracold atoms. We show for sinusoidal driving, that the equation describing scattering by the local contact interaction can be mapped to a recursion relation between Fourier

coefficients of the steady state wave function and overview methods of solving it. Despite the recursion being non linear in the Fourier index, it can be solved exactly by numerical methods.

As a key result we discover in Chapter 7 a strong enhancement of scattering, named scattering resonance, which is tunable by the periodic driving of the contact interaction. We explain these scattering resonances by the extended Hilbert space of Floquet theory and show that they emerge if the scattered particle has the same energy as a driving induced bound state. Using this condition we determine the position of the scattering resonances. We then evaluate additional properties of the resonances by fitting simplified formulas to their shape and show that they fulfil the so called anti-Kramers-Kronig relations. At last we investigate the case of small and large driving frequencies, where an analytic solution of the recursion is available.

In Chapter 8 we consider the more complicated case of a time-periodic potential, which is not driven sinusoidally. In this case higher harmonics of the driving frequency occur. We show that also in this case scattering resonances show up and investigate the effect of the more general driving scheme on these resonances.

Chapter 9 is devoted to the Conclusion and the Outlook.

2. Scattering Theory

Scattering theory is a powerful tool in order to understand and characterise the interaction of particles and quantify its strength in easily interpretable quantities like the total cross section. As it is the basis of the following Chapters, a brief overview of the time-independent scattering theory of quantum particles is given. In Section 2.1 we give an introduction in the considered setting, while in Section 2.2 important quantities are introduced. Section 2.2.1 is focused on the partial wave expansion, while Section 2.2.2 discusses the case of low energy physics. As an example we show in Section 2.3 the scattering by a hard-sphere potential.

2.1. Introduction

In this Section we consider the elastic scattering of a particle with mass m and no internal degrees of freedom by a static potential $V(\mathbf{r})$. The problem can be described by the Hamiltonian

$$H = -\frac{\hbar^2}{2m}\Delta + V(\mathbf{r}). \tag{2.1}$$

In order to use the theory below, the potential is assumed to vanish faster than $1/r$

$$\lim_{r\to\infty} V(\mathbf{r})r = 0, \tag{2.2}$$

where by r the modulus of the position vector $\mathbf{r}$ is denoted. Elastic scattering of two distinguishable particles with masses m_1 and m_2 can be mapped to the above setting by transforming to the center-of mass system [52]. The motion of the center-of mass can be separated and only the kinetic energy of the relative motion appears in the Schrödinger equation. The Hamiltonian of relative motion can be mapped to (2.1) by setting the reduced mass $\mu = (m_1 m_2)/(m_1+m_2)$ equal to m and the inter-atomic potential $U(\mathbf{r_2} - \mathbf{r_1})$ equal to $V(\mathbf{r})$ while introducing the particle seperation $\mathbf{r} = \mathbf{r}_2 - \mathbf{r}_1$.

2.2. Asymptotic Form and Scattering Quantities

In order to gain insight over general features of scattering, we assume an incoming plane wave along the z-axis and a potential centred at $\mathbf{r} = 0$. Intuitively, the interaction causes emission of the scattered wave function $\psi_{\mathrm{sc}}(\mathbf{r})$. It adds with the plane wave to the total wave-function

$\psi(\mathbf{r}) = e^{i\mathbf{kr}} + \psi_{\text{sc}}(\mathbf{r})$. As it is the asymptotic solution of the Schrödinger equation (2.1) for large radii [53], the scattered wave can be approximated by $\psi_{\text{sc}}(\mathbf{r}) \approx f(k,\theta,\phi)\frac{e^{ikr}}{r}$. It is a spherical wave with an amplitude only depending on the wave-vector k, the polar angle θ and the azimuthal angle ϕ [54]. Therefore the asymptotic solution of the scattering problem for large r is given by

$$\psi(\mathbf{r}) = e^{i\mathbf{kr}} + f(k,\theta,\phi)\frac{e^{ikr}}{r}. \tag{2.3}$$

The quantity $f(k,\theta,\phi)$ is called scattering amplitude and is the basis for calculating the following cross sections, which can be measured in experiment.

The differential cross section $\frac{d\sigma}{d\Omega}$ is defined as the probability current flowing through an infinitesimal small area $\mathbf{dA} = r^2\mathbf{d\Omega}$ located at the solid angle $\Omega = (\theta,\phi)$ divided by $d\Omega$ and the probability current density of the incoming wave [53]

$$|\mathbf{j}_{\text{in}}|\frac{d\sigma}{d\Omega}d\Omega = \mathbf{j}_{\text{out}}r^2\mathbf{d\Omega}. \tag{2.4}$$

Here $\mathbf{d\Omega}$ points in radial direction outside a sphere. By relating the probability current of the incoming wave $\mathbf{j}_{\text{in}} = \frac{\hbar\mathbf{k}}{m}$ to the one of the outgoing wave $\mathbf{j}_{\text{out}} = \frac{\hbar k}{mr^2}|f(k,\theta,\phi)|^2\hat{e}_r + \mathcal{O}\left(\frac{1}{r^3}\right)$ in the limit of large radii, one gets an equation connecting the differential cross section to the scattering amplitude

$$\frac{d\sigma}{d\Omega} = |f(k,\theta,\phi)|^2. \tag{2.5}$$

The total cross section σ is defined as the integral of the differential one over the full solid angle

$$\sigma = \int_\Omega d\Omega\frac{d\sigma}{d\Omega}. \tag{2.6}$$

Both differential (2.5) and total cross section (2.6) are measurable quantities.

2.2.1. Partial Wave Expansion

In the case of a spherical symmetric potential, the partial wave expansion leads to an intuitive way of rewriting and solving the scattering problem (2.1). A spherical symmetric potential implies a vanishing commutator between the Hamiltonian and the angular momentum operator $\hat{L} = \hat{r}\times\hat{p}$

$$[\hat{H},\hat{L}] = 0. \tag{2.7}$$

Thus angular momentum l is a good quantum number and the solution of the Schrödinger equation can be expressed in terms of the eigenstates of the angular-momentum operator, which are given by the spherical harmonics $Y_l^m(\theta,\phi)$. As the scattering problem has cylindrical symmetry, only the spherical harmonics without ϕ-dependence and therefore the magnetic quantum number $m = 0$ will contribute to the wave function. As the spherical harmonics with $m = 0$ are proportional to Legendre polynomials $P_l(\cos(\theta))$ [53], the wave function can be written in the form

$$\psi(r,\theta,\phi) = \sum_{l=0}^{\infty} R_l(r)P_l(\cos(\theta)). \tag{2.8}$$

By separating the radial and the angular degrees of freedom, the radial-Schrödinger equation for $R_l(r)$ can be derived

$$\left(\Delta_r + k^2 - v_{\text{eff}}(r)\right) R_l(r) = 0. \tag{2.9}$$

Here, $\Delta_r = \frac{1}{r^2}\frac{\partial}{\partial r} r^2 \frac{\partial}{\partial r}$ is the radial-Laplace operator and $v_{\text{eff}}(r) = \frac{l(l+1)}{r^2} + \frac{2m}{\hbar^2}V(r)$ the effective potential including the centrifugal barrier $\frac{l(l+1)}{r^2}$. In order to connect the cross section to the solution of (2.9), only the behaviour of the wave function for large radii is important. In this case the effective potential in equation (2.9) can be neglected and (2.9) is solved by

$$R_l(r) = A_l \frac{e^{-ikr}}{r} + B_l \frac{e^{ikr}}{r}, \tag{2.10}$$

which consist of an incoming and outgoing spherical wave. As the total flux through a sphere around the origin should be zero, both coefficients A_l and B_l have the same absolute value. This condition simplifies the description of the scattering process, as it allows us to introduce the scattering phase δ_l by setting [53]

$$B_l = e^{2i\delta_l} A_l. \tag{2.11}$$

The plane wave $e^{i\mathbf{kr}}$ can be expanded in Legendre polynomials [53]

$$e^{i\mathbf{kr}} = e^{ikr\cos(\theta)} = \sum_{l=0}^{\infty} (2l+1) i^l j_l(kr) P_l(\cos(\theta)). \tag{2.12}$$

Here we introduced the spherical Bessel function $j_l(x)$ [53, 55, 56], whose limit of large argument is given by

$$j_l(x) \approx \frac{\sin(x - l\frac{\pi}{2})}{x}. \tag{2.13}$$

Comparing (2.8) with (2.10) to (2.3), while expressing the occurring plane wave by (2.12) and (2.13), reveals the concrete value of the A_l coefficients

$$A_l = (-1)^l (2l+1) \frac{i}{2k} \tag{2.14}$$

and the asymptotic Form of the wave function

$$R_l(r) \propto \frac{1}{r} \sin(kr - l\frac{\pi}{2} + \delta_l). \tag{2.15}$$

The influence of the potential on the scattered-wave function is solely expressed by the value of the scattering phase, which leads to an additional shift of the wave function for large values of r. It is negative for repulsive potentials and positive for attractive ones.

The scattering amplitude can be calculated by comparing the asymptotic waveform (2.3) using (2.12) with the limit of large radii of the ansatz (2.8) to

$$f(k,\theta) = \sum_{l=0}^{\infty} f_l = \sum_{l=0}^{\infty} \frac{2l+1}{k} e^{i\delta_l} \sin(\delta_l) P_l(\cos(\theta)). \tag{2.16}$$

The total cross section evaluates to

$$\sigma = \frac{4\pi}{k^2} \sum_{l=0}^{\infty} (2l+1) \sin^2(\delta_l) \tag{2.17}$$

This equation shows, that all partial waves contribute to the total cross section and that it can be calculated by knowing all scattering phases. The contribution of the $l = 0$ part is called s-wave scattering, $l = 1$ p-wave scattering and so on. The value of the total cross section depends on the form of the scattering potential as well as the particle energy.

At last, we proof the optical theorem, which expresses the unitary of the scattering process. It links the imaginary part of the scattering amplitude in forward direction $\theta = 0$ to the total cross section and can be derived by evaluating the formulas (2.16) and (2.17) using $\theta = 0$ to

$$\sigma = \frac{4\pi}{k} \text{Im } f(\theta = 0). \tag{2.18}$$

An alternative, but more complicated, derivation [56, p. 26] reveals that it states, that the losses of probability flux through the scattering process, being proportional to σ, are compensated by the interference of incoming plane wave and scattered wave in forward direction. This interference is expressed in equation (2.18) by Im $f(\theta = 0)$.

2.2.2. Scattering Length

In the low energy limit, where the wave vector k of the incoming particle goes to zero, the scattering properties can be characterised by a single parameter, which is independent of the detection angle θ and particle energy. For any potential growing like $\frac{1}{r^s}$, with $s > 2l + 3$, it can be shown [57, pp. 45], [58, p. 306] that

$$\lim_{k \to 0} k^{2l+1} \cot(\delta_l) = -\frac{1}{a_l}, \tag{2.19}$$

where a_l is the energy independent l-wave scattering parameter. Equation (2.19) shows that in the low energy limit s-wave scattering is dominant, as all scattering phases corresponding to higher partial waves are suppressed by a factor of k^{2l}. We therefore can characterise the scattering process at low wave vectors by the s-wave scattering length

$$a = a_{l=0}, \tag{2.20}$$

which does not depend on the energy or the angle θ. Therefore s-wave scattering at low energy is has a simple structure in comparison to higher partial waves or finite energies. The scattering length (2.20) determines the total cross section to

$$\sigma = 4\pi |a|^2. \tag{2.21}$$

This equation gives an intuition for the scattering length, as it relates it to a length scale characterising the cross sectional area.

By inserting equation (2.19) into (2.16) we find that the scattering length can be calculated by performing the limit of vanishing momentum of the scattering amplitude

$$a = -\lim_{k\to 0} f(k,\theta). \tag{2.22}$$

At this point we note, that the scattering length is only the first contribution in the so-called effective range expansion [57, 58]. Equation (2.22) will be generalised in Chapter 5 to the case of scattering by a time-periodic potential and is therefore fundamental to this thesis.

2.3. Scattering by a Hard-Sphere Potential

As it is the most simple and fundamental case of a scattering potential, we discuss the scattering by a hard-sphere potential. It consists of a sphere with infinite large repulsion around the origin

$$V(r) = \begin{cases} \infty \ , r < r_0 \\ 0 \ , r > r_0 \end{cases} . \tag{2.23}$$

Outside the radius r_0 equation (2.9) is solved by spherical Bessel $j_l(kr)$ and spherical Neumann $y_l(kr)$ functions [53, 55, 56]. These functions have the following asymptotic properties for large arguments x

$$j_l(x) \approx \frac{\sin(x - l\frac{\pi}{2})}{x},\ y_l(x) \approx -\frac{\cos(x - l\frac{\pi}{2})}{x} \tag{2.24}$$

and for small arguments

$$j_l(x) \approx \frac{x^l}{(2l+1)!!},\ y_l(x) \approx \frac{(2l-1)!!}{x^{l+1}}. \tag{2.25}$$

The double factorial $n!!$ is defined by only multiplying the odd numbers up to the integer n. The solution outside the sphere can be written in the form

$$R_l(r) = A_l j_l(kr) + B_l y_l(kr). \tag{2.26}$$

With the substitution

$$A_l = C_l \cos(\delta_l),\ B_l = -C_l \sin(\delta_l) \tag{2.27}$$

the asymptotic Form of (2.26) is expressed by the scattering phase δ_l, which can be computed by the continuity condition at the radius r_0 to be

$$\tan(\delta_l) = \frac{j_l(kR_0)}{y_l(kR_0)}. \tag{2.28}$$

Inserting the approximation (2.25) the result for small kr_0 is derived to

$$\delta_l \approx -\frac{(kr_0)^{2l+1}}{(2l+1)!!(2l-1)!!}. \tag{2.29}$$

This result again shows the dominance of the s-wave scattering in the low energy limit: If the parameter kr_0 is small, higher angular momentum contributions drop off very fast and only the s-wave scattering phase with angular momentum $l = 0$ contributes to the scattering. The resulting s-wave scattering length (2.20)

$$a = r_0 \tag{2.30}$$

equals the radius of r_0 of the repulsive potential and in this case the scattering length can be related to the size of the scattering potential.

We now want to summarise this Section shortly. We gave an introduction into static scattering theory and discussed how the measurable scattering cross section can be calculated by the use of quantum mechanics. We defined the s-wave scattering length (2.20), which characterises the scattering process in the case of low-energy physics. Due to its importance we will lay a main focus on investigating the scattering length in the further Chapters. As two-body collisions are a dominant process in interacting many-body systems, the scattering length characterises the interaction strength of such systems at low temperatures [59]. One example are Bose-Einstein condensates, where the scattering length can be tuned by the usage of Feshbach resonances, which we will discuss in the next Section in detail.

3. Feshbach Resonances

This Chapter is devoted to Feshbach resonances. In Section 3.1 we give an introduction into those, while in Section 3.2 we provide an overview over those resonances and summarise their realisation in ultracold gas experiments. In the last part of this Section we survey literature investigating how periodic driving and ac-magnetic fields can be used in order to tune and induce resonances.

3.1. Introduction to Feshbach Resonances

A resonance can be understood as an almost bound state. As it is not truly bound it is associated with a lifetime [56] and is seen in scattering events in a phase shift of approximately π [38] of the scattering phase combined with an enhancement of the scattering amplitude. Resonances can be divided into two groups: The shape resonances occur due to a quasi-bound state, whose energy lies in a continuum. One example is a trapped state behind a potential barrier, which can decay into the continuum due to the finiteness of the barrier. As the properties of these resonances depend on the shape of the potential, they are called shape resonances.

The second type of resonances are the Feshbach resonances, which appear in scatting of multi-channel systems [56]. Within a multi-channel system two scatterers with multiple internal states interact. Each of these internal states is labelled by a channel number or a quantum number of the internal degrees of freedom. An example of a multi-channel system are atoms in a constant magnetic field, where energy levels split due to the Zeeman effect. The internal states of the atom, which can be labelled by the total angular momentum F of the atom and its projection along the spin-quantization axis m_F [60], are the channels, if the atoms are viewed as a multi-channel system. If a channel supports a scattering state, it is said to be open, while closed channels support bound states. In order to observe a Feshbach resonance, a system needs to have both open and closed channels. The coupling between these channels can modify the scattering properties in the open channels significantly, if the energy of the scattering state is close to the energy of a bound state in a closed channel. These resonances are named after Hermann Feshbach, as he developed a resonant scattering scheme in the field of nuclear physics in Refs. [61, 62].

We will now discuss Feshbach resonances in more detail, following Refs. [38, 56, 63, 64] and assume a scatterer with multiple internal states possessing the energy E_i, which equal the threshold energy of the potential $V_i(r)$ in channel i

$$\lim_{r\to\infty} V_i(r) = E_i. \tag{3.1}$$

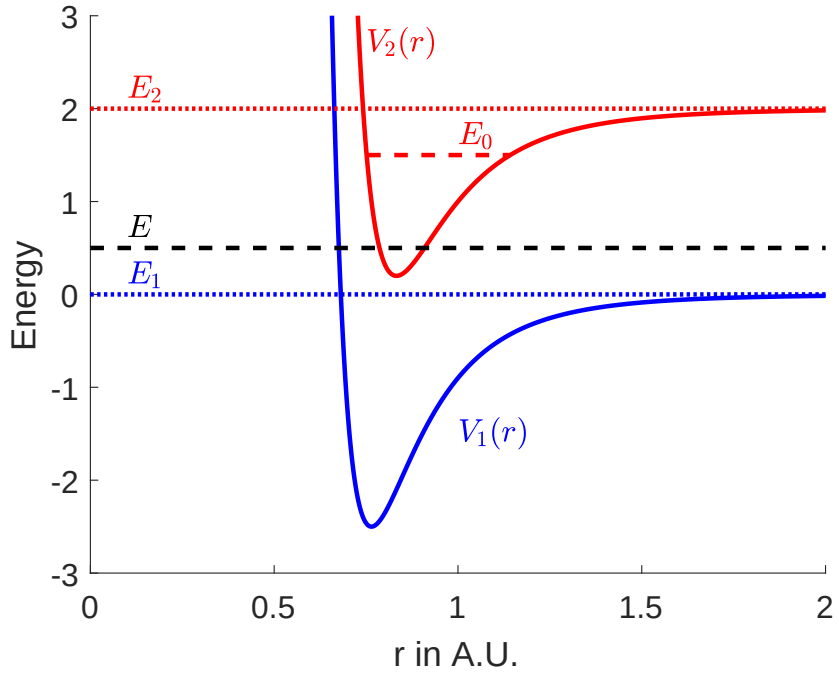

Figure 3.1.: A sketch of the physics behind equations (3.4). The open channel (blue) supports a free solution with energy E, while the closed (red) possesses a bound state with energy E_0. If both energies approach each other, a Feshbach resonance occurs. The respective channel thresholds are included with dashed lines.

We now specialise to a two-channel system with an open and a closed channel. The first channel is defined to be open and the channel thresholds are said to fulfil the relation $E_1 < E_2$. We assume m to be the particle mass or the reduced mass if working in the centre-of mass frame. The scattering state solution of the corresponding uncoupled Schrödinger equation in the first channel

$$\left[-\frac{\hbar^2}{2m}\frac{1}{r^2}\frac{\partial}{\partial r}r^2\frac{\partial}{\partial r}+V_1(r)\right]R_1^{\mathrm{un}}(r)=E\;R_1^{\mathrm{un}}(r) \tag{3.2}$$

is characterised by the background scattering length δ_{Bg}. In order to have a free channel, the energy E must lie above E_1. The second channel is considered as closed. It possesses in the uncoupled case the bound state wave function $R_0(r)$ fulfilling the Schrödinger equation

$$\left[-\frac{\hbar^2}{2m}\frac{1}{r^2}\frac{\partial}{\partial r}r^2\frac{\partial}{\partial r}+V_2(r)\right]R_0(r)=E_0R_0(r). \tag{3.3}$$

As shown in Figure 3.1, the bound state energy E_0 of the second channel is assumed to lie between E_1 and E_2. Introducing inter-channel coupling $V_{12}(r)$ the coupled radial Schrödinger equation for

such a system can be written in the form

$$\left[-\frac{\hbar^2}{2m}\frac{1}{r^2}\frac{\partial}{\partial r}r^2\frac{\partial}{\partial r}+V_1(r)\right]R_1(r)+V_{12}(r)R_2(r)=E\ R_1(r) \tag{3.4}$$

$$\left[-\frac{\hbar^2}{2m}\frac{1}{r^2}\frac{\partial}{\partial r}r^2\frac{\partial}{\partial r}+V_2(r)\right]R_2(r)+V_{12}(r)R_1(r)=E\ R_2(r). \tag{3.5}$$

If the coupling $V_{12}(r)$ between the channels is activated, the bound state $u_0(r)$ can lead to a resonance, as discussed in Ref. [56]. This resonance is seen in the scattering phase δ connected to the unbound wave function, as it splits into two parts

$$\delta=\delta_{\mathrm{bg}}+\delta_{\mathrm{Res}}. \tag{3.6}$$

The background phase δ_{bg} stems from scattering by the potential $V_1(r)$, while the resonant δ_{Res} originates from coupling to the closed channel. Assuming a smooth energy dependence, this resonant phase can be approximated by [56]

$$\tan(\delta_{\mathrm{Res}})=-\frac{\Gamma/2}{E-E_R}, \tag{3.7}$$

where E_R is the position of the resonance and Γ is its width. Both quantities can be expressed as matrix elements involving the channel coupling potential V_{12}, the bound state and the regular solution $u_1^{\mathrm{reg}}(r)$ together with the propagator $\hat{G}$ [56, p. 149] of the free channel. The position E_R equals the energy of the bound state E_0 plus an energy shift δE originating from the interaction with the open channel

$$\delta E=\langle u_0|\hat{V}_{12}\hat{G}\hat{V}_{12}|u_0\rangle. \tag{3.8}$$

The width Γ is associated with a lifetime of the resonance and is calculated to be

$$\Gamma=2\pi|\langle u_0|\hat{V}_{12}|u_1^{\mathrm{reg}}\rangle|^2. \tag{3.9}$$

Especially in the case of ultracold quantum gases the low energy limit of the scattering phase becomes interesting. As shown in Section 2.2.2 the scattering length a is the relevant parameter and is given by [38]

$$a=-\lim_{k\to 0}\frac{\delta}{k}=a_{\mathrm{bg}}+\frac{a_{\mathrm{bg}}\Gamma_0}{-E_R+i\frac{\gamma}{2}}. \tag{3.10}$$

Here k is the relative momentum and $\Gamma_0=\lim_{k\to 0}\frac{\Gamma}{2ka_{\mathrm{bg}}}$ is the low energy limit of the width Γ. The imaginary part $i\gamma/2$ is added by hand in order to describe additional losses, which might occur, if the bound state has an additional decay channel.

3.2. Feshbach Resonances in Ultracold Quantum Gases

We overview the common methods to implement Feshbach resonances in ultracold quantum gases and specialise in the end of the Section to the case of resonances induced by periodic driving. The

scattering length characterises the interaction of ultracold atoms [52, 59]. As Feshbach resonances allow a tuning of the scattering length, they provide a powerful tool for tuning the inter-particle interaction in an ultracold gas, which lead to the discovery of novel and interesting phenomena [38, 44].

3.2.1. Magnetic Feshbach Resonance

Magnetic Feshbach resonances are a common tool in order to control the scattering length [38,63] by adjusting a spatially constant magnetic field. They have been first observed experimentally in a cold gas experiment with ^{23}Na by Ref. [65] and with ^{85}Rb by Ref. [66]. Atoms in a magnetic field obtain a splitting of their energy levels by $\Delta E_i = -\boldsymbol{\mu}_i \mathbf{B}$ due to the Zeeman effect. As this shift depends on the magnetic moment $\boldsymbol{\mu}_i$ of the particular internal state, changing of the magnetic field leads to a change of the relative energy between two channels. If this difference becomes zero, a Feshbach resonance occurs. Therefore the position of the resonance can be parametrised in the form [38], if the magnetic field is applied parallel to the difference of the magnetic moments

$$E_R = \delta\mu(B - B_0). \tag{3.11}$$

The variable B_0 characterises the magnetic field at resonance position, $\delta\mu = \mu_{\text{atoms}} - \mu_{\text{pair}}$ is the difference of magnetic moments between the two separated atoms in the open channel and the bound pair in the closed one. Losses through two body collisions described by γ in equation (3.10) can usually be neglected in the case of a magnetic Feshbach resonance [38]. With these assumptions the scattering length (3.10) simplifies to the well-known approximate formula [63]

$$a(B) = a_{\text{bg}} \left(1 - \frac{\Delta}{B - B_0}\right). \tag{3.12}$$

Here a_{bg} denotes the background scattering length, which is obtained away from resonance position. The width Δ is given by

$$\Delta = \Gamma_0/\delta\mu. \tag{3.13}$$

Equation (3.12) is plotted in Figure 3.2. Close to the resonance the scattering length can be tuned to infinite repulsion or attraction. The width Δ can be determined using Figure 3.2 **(a)**. It is the difference of the position of the resonance B_0 and the magnetic field strength where the scattering length vanishes.

3.2.2. Optical Feshbach Resonance

An optical Feshbach resonance is created using laser light, which is nearly resonant to a transition between a scattering state and an exited molecular bound state and therefore induces a coupling of

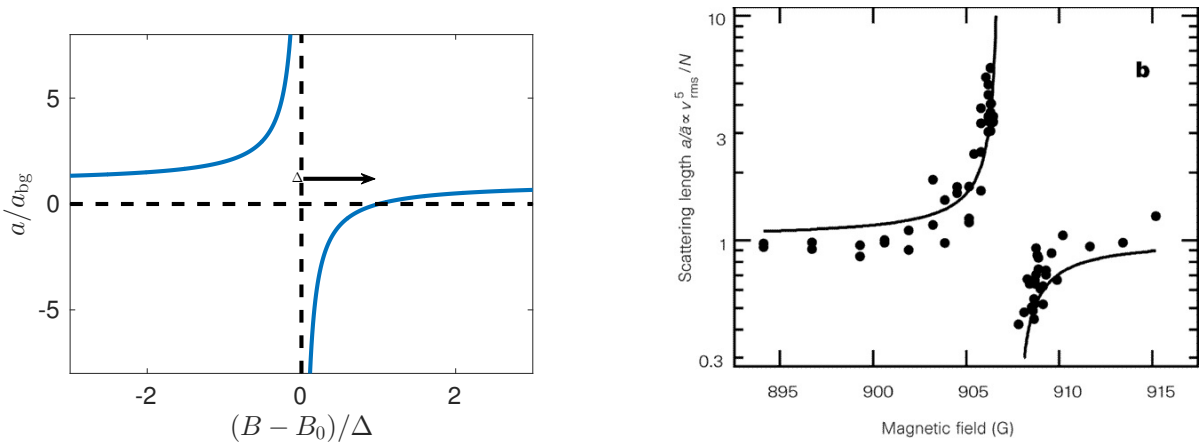

(a) **(b)**

Figure 3.2.: (a): Plot of the approximative formula (3.12) of the scattering length a in case of a magnetically tuned Feshbach resonance without losses.
(b): First experimental observation of a magnetic Feshbach resonance in a cold gas experiment with ^{23}Na. The Figure was created by Inouye et al. [65]

both [67–69]. The scattering length can be controlled by tuning the laser frequency ω or intensity I instead of a magnetic field [38] and follows the equation

$$a = a_{\mathrm{bg}} \left(1 + \frac{\Gamma_0(I)}{\hbar(\omega - \omega_0 - \delta\omega(I)) + i\gamma/2} \right) \tag{3.14}$$

But unlikely to most magnetic Feshbach resonances the bound state decays, which results in a non-vanishing loss parameter γ. Therefore the scattering length becomes complex, where real part characterises the scattering strength and the imaginary the particle loss [38, 70]. According to equation (3.14), the real part of the scattering length obtains a maximum at a finite value, restricting the tunability of the resonance. The behaviour of (3.14) is shown in Figure (3.3).

3.2.3. Microwave- and Radio Frequency induced Feshbach Resonances

These classes of resonances are induced or manipulated by the use of microwave (mw) and radio frequency (rf) fields and have been discussed in recent literature [71–79]. The basic idea behind those considerations is coupling of different states by those fields. The coupling leads to an energy shift of bound states in a field dressed picture and results in a Feshbach resonance, which is controllable by the fields. As in many setups an oscillating magnetic field is considered, the coupling strength is limited by the relatively weak magnetic dipole matrix elements. A pioneer in this topic was Moerdijk [71], who considered rf-fields for evaporative cooling but also suggested them for the creation of resonances. Kaufmann et al. [72] investigated the coupling of bound states due to rf fields with a static magnetic field close to a static Feshbach resonance in a experiment. Ref. [74] extended this to the coupling of a colliding pair with a molecular bound state. Both predict the tuning of resonances by changing both the frequency and strength of a rf field. Tscherbul et al. [75] discovered, that new

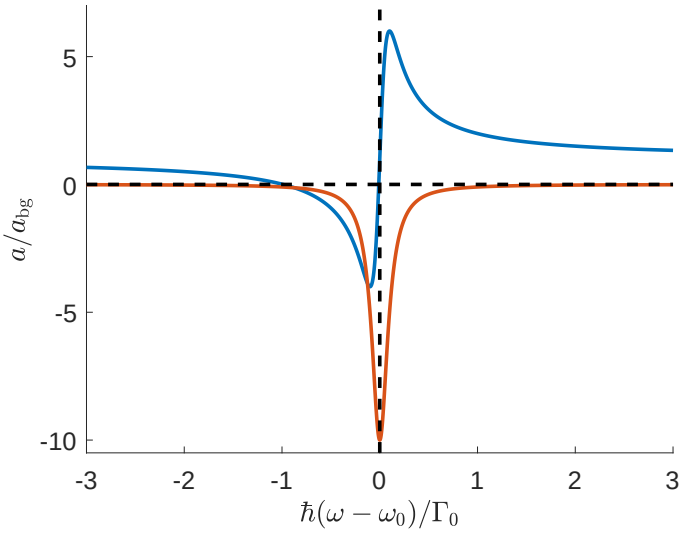

Figure 3.3.: Plot of the real (blue) and imaginary part (red) of the scattering length in case of an optical Feshbach resonance for $\gamma = 0.1\Gamma_0$. In contrast to a resonance without losses, an imaginary part exists around the central position and a finite maximum of the real part occurs.

resonances can be induced by rf field using a coupled channel approach in a field dressed picture. Xie et al. [76] showed the ability of rf fields to tune the interspecies scattering length in ^{6}Li + ^{40}K collisions, while Owens et al. [78] obtained the creation of new resonances with ^{39}K + ^{133}Cs by using scattering calculations in a field dressed basis.

3.2.4. Driving Induced Scattering Resonance

The driving induced scattering resonance will be the focus of this thesis and has been discussed in Refs. [3,4,80] in the case of a periodically driven magnetic Feshbach resonance. The underlying idea is to create a time-periodic inter-atomic potential by driving a parameter of the considered physical system time periodically. As we pointed out in Chapter 1 and we will show in this thesis, a time-periodic potential is able to create bound states, which interact with scattering states in a way that they induce a resonance. A possible realisation of this resonance was suggested by Smith [3, 80, 81]. He considered a magnetic Feshbach resonance with a time-periodic magnetic field [3]

$$B(t) = B_1 + B_2 \cos(\omega t), \tag{3.15}$$

which is polarised along the spin-quantisation axis. He showed by using a Lippmann-Schwinger formalism that this results in a time-dependent potential inducing a Feshbach resonance at the bias magnetic field B_1, which does not need to coincide with the field strength where the static resonance occurs. By tuning the driving frequency ω and field strength B_2 position and width of this artificially created resonance can be tuned [80]. Smith named this method by "Modulated Magnetic Feshbach Resonance".

Here we go beyond his research and examine in Chapter 7 the driving induced scattering resonance in a more generalised setting and for a larger amount of driving strengths and give a deeper explanation of their emergence. In order to do this, we extend in Chapter 5 scattering theory to time-periodic scattering potentials by using Floquet theory. This Floquet-scattering theory is capable of solving Schrödinger equation in the case of a time-periodic Hamiltonians. As an introduction to this setting, we first discuss Floquet theory in the next Chapter.

4. Floquet Theory

In this Chapter Floquet theory is introduced. This theory can be used in order to solve time dependent, but periodic, problems exactly by converting them to a static problem in a more complex Hilbert space. We initiate this Chapter in Section 4.1 by Floquet theorem, which can be considered as the "The Bloch theorem in time". Section 4.2 introduces Floquet equation and summarises relevant properties of periodically driven systems. Section 4.3 is dedicated to the time evolution of states under a time-periodic Hamiltonian.

4.1. Floquet Theorem

Floquet theorem was initially stated in the context of ordinary differential equations [35] and can be written in terms of quantum mechanics in the following way [32, 33, 82]. A time-periodic Hamilton operator

$$\hat{H}(t) = \hat{H}(t+T), \tag{4.1}$$

with $\omega = 2\pi/T$ as the driving frequency is considered. Then Floquet theorem states the existence of solutions $|\psi(t)\rangle$ of the time dependent Schrödinger equation

$$i\hbar\frac{\partial}{\partial t}|\psi(t)\rangle = \hat{H}(t)|\psi(t)\rangle, \tag{4.2}$$

which are of the form

$$|\psi(t)\rangle = e^{-i\frac{\epsilon}{\hbar}t}|\phi(t)\rangle. \tag{4.3}$$

Here ϵ is called the quasi energy or the Floquet energy. It is not to be confused with the physical energy E, which is not necessarily a conserved quantity in a driven system. The Floquet mode $|\phi(t)\rangle$ has the same time-periodicity as the Hamiltonian (4.1)

$$|\phi(t)\rangle = |\phi(t+T)\rangle. \tag{4.4}$$

Note that Floquet theorem is similar to Bloch theorem of solid-state physics [14,83]. Instead of having a Hamilton operator being periodic in space, in Floquet theory the Hamiltonian is considered to be time periodic. The well-known quasimomentum can be mapped to the Floquet energy and the Bloch function corresponds to the Floquet mode.

4.2. Floquet Equation and Properties of Floquet Modes

Using representation (4.3) of the wave function, an eigenvalue equation for the Floquet energy can be derived by inserting (4.3) into (4.2):

$$\hat{\mathcal{H}}|\phi(t)\rangle = \epsilon|\phi(t)\rangle. \tag{4.5}$$

This eigenvalue equation of the Floquet operator

$$\hat{\mathcal{H}} = \hat{H} - i\hbar\frac{\partial}{\partial t} \tag{4.6}$$

is called the Floquet equation. It is defined on the Floquet-Hilbert space $\mathcal{F} = \mathcal{R}\otimes\mathcal{T}$, which consists of the configuration space $\mathcal{R}$ of the original Hamiltonian $\hat{H}$ and the space of time-periodic functions $\mathcal{T}$. By using this Floquet-Hilbert space, time, which is regarded as a parameter in Schrödinger equation, is promoted to a coordinate. This extended Hilbert-space can be used to write down the Floquet equation in a way not using time explicitly. By using the Fourier transformation of both Floquet mode and Hamiltonian

$$|\phi(t)\rangle = \sum_{n=-\infty}^{\infty} e^{-in\omega t}|\phi_n\rangle, \tag{4.7}$$

$$\hat{H}(t) = \sum_{m=-\infty}^{\infty} e^{-im\omega t}\hat{H}_m, \tag{4.8}$$

equation (4.5) can be mapped to a static one

$$\sum_{m=-\infty}^{\infty} \hat{H}_m|\phi_{n-m}\rangle - n\hbar\omega|\phi_n\rangle = \epsilon|\phi_n\rangle,\ \forall n \in \mathbb{Z}, \tag{4.9}$$

which is involving the Fourier components $|\phi_n\rangle$ of the Floquet mode. In addition this equation can be written as an eigenvalue equation of an infinitely sized matrix

$$\mathcal{H} = \begin{pmatrix} \ddots & \ddots & \ddots & & & & \\ \dots & \hat{H}_1 & \hat{H}_0 - (n-1)\hbar\omega & \hat{H}_{-1} & \dots & & \\ & \dots & \hat{H}_1 & \hat{H}_0 - n\hbar\omega & \hat{H}_{-1} & \dots & \\ & & \dots & \hat{H}_1 & \hat{H}_0 - (n+1)\hbar\omega & \hat{H}_{-1} & \dots \\ & & & & \ddots & \ddots & \ddots \end{pmatrix}. \tag{4.10}$$

The eigenvalues of this matrix are given by the Floquet energies ϵ and the eigenvectors consist of the Fourier components of the Floquet modes

$$|\tilde{\phi}\rangle = \begin{pmatrix} \dots \\ |\phi_{n-1}\rangle \\ |\phi_n\rangle \\ |\phi_{n+1}\rangle \\ \dots \end{pmatrix} \tag{4.11}$$

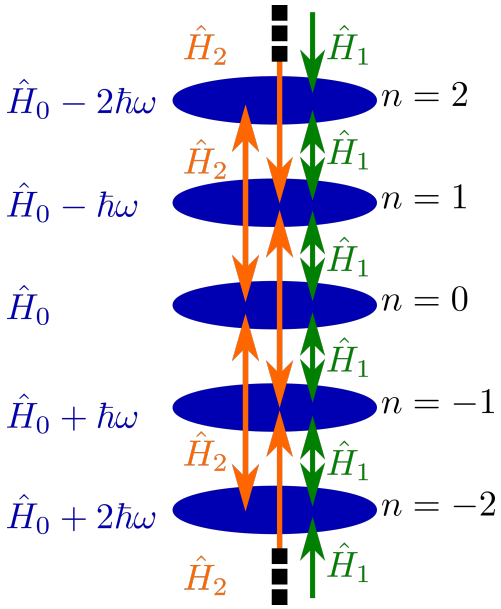

Figure 4.1.: A graphical representation of equation (4.9): The blue ovals represent the configuration space $\mathcal{R}$ labelled by Fourier indices n of the Floquet mode. On this Hilbert space the Hamiltonian $\hat{H}_0 - \hbar n\omega$ acts in terms of a self energy. Higher Fourier components of the Hamiltonian $\hat{H}_m$ lead to coupling of channels with different Fourier index n. This coupling is indicated in the Figure by green and yellow arrows.

Equations (4.9) and (4.10) are a fundamental results of Floquet theory and visualised in Figure 4.1. Any time-periodic Schrödinger equation can be mapped to a static problem, which is located in a larger Hilbert space, by using Fourier transform. But the price of introducing a channel number by the Fourier index n has to be paid, as equation (4.9) can be seen as a static multi-channel Schrödinger equation. This channel structure leads to a more complicated eigenvalue equation in comparison to the static case, as the Floquet-Hilbert space is much larger than the static one, but equation (4.9) is much simpler to solve than the corresponding time-dependent Schrödinger equation. We introduce the concept of Floquet channels by locating the Fourier-component $|\phi_n\rangle$ in the Floquet channel with number n.

From now on, we assume Floquet energy and modes to be labelled by a quantum number q and consider a Floquet mode $|\phi^q\rangle$ with corresponding Floquet energy ϵ_q. Then $|\phi^{q,n}\rangle = e^{in\omega t}|\phi^q\rangle$ is also a Floquet mode yielding the same physical wave function $|\psi(t)\rangle$, but it has a Floquet energy $\epsilon_{q_n} = \epsilon_q + \hbar n\omega$. As the modes describe the same physical wave function, Floquet energies ϵ_q are unique only up to integer multiples of the driving frequency $\hbar\omega$. Similar to the case in solid-state physics, Brillouin zones can be introduced in frequency or Floquet-energy space, respectively. Due to aforementioned ambiguity, the quasi energies ϵ_q can be mapped into the first Floquet-Brillouin zone, which is defined as the interval $\left[-\frac{\hbar\omega}{2}, \frac{\hbar\omega}{2}\right[$ and is used for the definition of the set

$$Q_{1.\mathrm{FBZ}} = \left\{ q : \epsilon_q \in \left[-\frac{\hbar\omega}{2}, \frac{\hbar\omega}{2} \right[\right\}. \tag{4.12}$$

The Floquet modes $|\phi^{q,n}\rangle$ fulfil the orthonormality conditions of the scalar product of $\mathcal{F}$:

$$\langle\langle\phi^{q,n}|\phi^{p,m}\rangle\rangle = \frac{1}{T}\int_0^T dt\langle\phi^{q,n}(t)|\phi^{p,m}(t)\rangle = \delta_{q,p}\delta_{n,m}. \tag{4.13}$$

Here $\langle\phi^{q,n}(t)|\phi^{p,m}(t)\rangle$ denotes the scalar product of $\mathcal{R}$. If q and p are continuous indices, the first Kronecker delta has to be replaced by a Dirac-delta function. By using the Fourier transform of the Floquet mode (4.7) and the orthonormality relation, the completeness relation in $\mathcal{F}$ reads according to Ref. [82]

$$\sum_{q\in Q_{1.\mathrm{FBZ}}}\sum_{n=-\infty}^{\infty}|\phi^{q,n}(t)\rangle\langle\phi^{q,n}(t')| = \mathbb{I}_{\mathcal{R}}\delta(t-t'). \tag{4.14}$$

We denote with $\mathbb{I}_{\mathcal{R}}$ the identity on the configuration space $\mathcal{R}$. If the times t and t' are equal up to an integer multiple of T, it is sufficient to sum over the first Brillouin zone in order to get a modified completeness relation

$$\sum_{q\in Q_{1.\mathrm{FBZ}}}|\phi^{q}(t)\rangle\langle\phi^{q}(t)| = \mathbb{I}_{\mathcal{R}}. \tag{4.15}$$

As the last point of this Chapter, a general formula for time-averaged expectation values is given. We consider a time-dependent operator $\hat{A}(t)$:

$$A(t) = \sum_{n=-\infty}^{\infty} e^{-in\omega t}\hat{A}_n, \tag{4.16}$$

which has the same time periodicity as the Hamilton operator. The time averaged expectation value is then defined as

$$\langle\langle\hat{A}(t)\rangle\rangle = \langle\langle\psi(t)|\hat{A}(t)|\psi(t)\rangle\rangle = \frac{1}{T}\int_0^T dt\langle\psi(t)|\hat{A}(t)|\psi(t)\rangle. \tag{4.17}$$

If the wave function $|\psi(t)\rangle$ is assumed to be a Floquet state according to (4.4), the Fourier decomposition (4.7) can be used in order to write the expectation value in the form

$$\langle\langle\hat{A}(t)\rangle\rangle = \sum_{n,s=-\infty}^{\infty}\langle\phi_{n+s}|\hat{A}_s|\phi_n\rangle. \tag{4.18}$$

By setting $A(t) = \mathbb{I}_{\mathcal{R}}$, this equation can be used in order to calculate the norm of the Floquet state $|\psi(t)\rangle$.

4.3. Time Evolution and Effective Hamiltonian

With the knowledge of the Floquet energies and the corresponding modes any quantum state $|\psi(0)\rangle$ can be propagated by the Hamiltonian $\hat{H}(t)$. Let the propagator corresponding to $\hat{H}(t)$ with initial time $t_0 = 0$ be denoted by $\hat{U}(t,0)$. The time dependence

$$|\psi(t)\rangle = \hat{U}(t,0)|\psi(0)\rangle \tag{4.19}$$

of an arbitrary quantum state $|\psi\rangle$ can be explicitly calculated by inserting the identity (4.15) at time $t = 0$ into (4.19). Using the notation

$$c_q = \langle \phi^q(0)|\psi(0)\rangle, \tag{4.20}$$

the propagated state can be written in the form $|\psi(t)\rangle = \sum_{q\in Q_{1.\mathrm{FBZ}}} \hat{U}(t,0)|\phi^q(0)\rangle c_q$. Floquet theorem validates that Floquet modes $|\phi^q(t=0)\rangle$ equal their corresponding steady state wave function $|\psi^q(t=0)\rangle$ at $t = 0$ and therefore the time evolution of the Floquet mode $|\phi^q(0)\rangle$ is given by $\hat{U}(t,0)|\phi^q(0)\rangle = e^{-i\epsilon_q/\hbar\ t}|\phi^q(t)\rangle$. With this knowledge the time-evolved quantum state is written in the form

$$|\psi(t)\rangle = \sum_{q\in Q_{1.\mathrm{FBZ}}} c_q e^{-i\frac{\epsilon_q}{\hbar}t}|\phi^q(t)\rangle. \tag{4.21}$$

As we assumed $|\psi\rangle$ to be arbitrary, the propagator reads

$$\hat{U}(t,0) = \sum_{q\in Q_{1.\mathrm{FBZ}}} |\phi^q(t)\rangle\langle\phi^q(0)|e^{-i\epsilon_q/\hbar\ t}. \tag{4.22}$$

By again inserting identity (4.15) at $t = 0$, equation (4.22) can be rewritten as

$$\hat{U}(t,0) = \hat{U}_{\mathrm{p}} e^{-i\hat{H}_{\mathrm{eff}}/\hbar\ t}, \tag{4.23}$$

where $\hat{U}_{\mathrm{p}} = \sum_{q\in 1.\mathrm{BZ}} |\phi_q(t)\rangle\langle\phi_q(0)|$ is denoted as micromotion operator [31], as it deals with the time-periodic part of the dynamics. The effective Hamiltonian

$$\hat{H}_{\mathrm{eff}} = \sum_{q\in Q_{1.\mathrm{FBZ}}} \epsilon_q |\phi_q(0)\rangle\langle\phi_q(0)| \tag{4.24}$$

contains the slowly varying components of the dynamics and all information about the Floquet energies and the Floquet modes at times $t = 0$. As $\hat{U}_{\mathrm{p}}(t+T) = \hat{U}_{\mathrm{p}}(t)$ and $\hat{U}_{\mathrm{p}}(0) = \mathbb{I}$, the effective Hamiltonian contains all information to propagate any quantum state at multiple integers of the driving period T. The propagator has in this special case a simple structure of

$$\hat{U}(nT) = e^{-i\hat{H}_{\mathrm{eff}}/\hbar\ nT} = [\hat{U}(T)]^n,\ n \in \mathbb{Z}. \tag{4.25}$$

It is now the point to do some concluding remarks. In this Chapter we introduced Floquet theory, with which one is able to solve the time-dependent Schrödinger equation in the case of a time-periodic Hamiltonian. As a main point we saw by using Floquet theorem in combination with Fourier transform, that we can map the time-dependent Schrödinger equation to a static one, which is located in a more complex Hilbert space. We saw that this Floquet equation looks similar to a multi-channel Schrödinger equation. This fact we exploit in the next Chapter in order to generalise the scattering theory of Chapter 2 to time-periodic potentials.

5. Floquet-Scattering Theory

In this Section we present a scattering theory for time-periodic potentials by usage of Floquet theorem. Due to the driving-induced channel structure, Floquet-scattering theory has similarities to multi-channel quantum scattering theory [56], if the Fourier index n is viewed as a channel. Instead of introducing a Lippmann-Schwinger formalism like Refs. [3, 80] our focus lies on the partial wave expansion. We start in Section 5.1 with introducing time averaged scattering quantities. With this basic framework, the Floquet-partial wave expansion is presented in Section 5.2. We finish this Section by the Floquet-optical theorem, which expresses the unitary of the Floquet-scattering process. Section 5.3 is dedicated to the scattering of indistinguishable particles.

5.1. Coupled-Channel Equations and Cross Sections

In this Section we rewrite the time dependent scattering problem in a set of static coupled equations. This step is useful in order to introduce the scattering amplitude and cross section in an intuitive way.

5.1.1. Coupled-Channel Equations

In order to investigate the effect of periodic driving on the scattering of quantum particles, we use a Schrödinger theory with a Hamiltonian

$$H = -\frac{\hbar^2}{2m}\Delta + V(\mathbf{r}, t), \tag{5.1}$$

where a time-periodic potential $V(\mathbf{r}, t)$ is considered. The period of the potential is denoted by T, i.e.

$$V(\mathbf{r}, t+T) = V(\mathbf{r}, t),\ \forall t \in \mathbb{R}. \tag{5.2}$$

As presented in Chapter 4, the driving frequency ω is defined as $\omega = 2\pi/T$. The Hamiltonian (5.1) can be interpreted in two ways. On the one hand it describes a single particle with mass m under the influence of an external potential $V(\mathbf{r}, t)$. On the other hand it can be also used to describe the scattering of two particles with masses m_1 and m_2 by the inter-particle interaction $U(\mathbf{r}_1 - \mathbf{r}_2, t)$ in the centre-of-mass system [55]. In this case the mass m has to be identified with the reduced

mass $\mu = m_1 m_2/(m_1+m_2)$ and the potential $V(\mathbf{r},t)$ by the inter-particle interaction potential $U(\mathbf{r},t)$.

In order to find a reasonable description of time-periodic scattering, the goal is to obtain the scattering behaviour of steady-state solutions $\psi(\mathbf{r},t) = e^{-i\epsilon/\hbar\ t}\phi(\mathbf{r},t)$ of the Floquet-equation

$$\left[-\frac{\hbar^2}{2m}\Delta + V(\mathbf{r},t) - i\hbar\frac{\partial}{\partial t}\right]\phi(\mathbf{r},t) = \epsilon\ \phi(\mathbf{r},t). \tag{5.3}$$

The first step is to remove the explicit time dependence of the Floquet equation by using the Fourier transform of the Floquet mode and the potential

$$\phi(\mathbf{r},t) = \sum_{n=-\infty}^{\infty} e^{-in\omega t}\phi_n(\mathbf{r}) \tag{5.4}$$

$$V(\mathbf{r},t) = \sum_{n=-\infty}^{\infty} e^{-in\omega t}V_n(\mathbf{r}) \tag{5.5}$$

and to introduce the Floquet channel number by the Fourier-index n. Similar to (4.9), equation (5.3) can be written down in the form

$$-\frac{\hbar^2}{2m}\Delta\phi_n(\mathbf{r}) + \sum_{m=-\infty}^{\infty} V_m(\mathbf{r})\phi_{n-m}(\mathbf{r}) = (e + n\hbar\omega)\phi_n(\mathbf{r}),\ \forall n \in \mathbb{Z}. \tag{5.6}$$

In this equation the coupling of Floquet channels is given by the Fourier-components of the potential $V_n(\mathbf{r})$ which have $n \neq 0$.

5.1.2. Asymptotic Waveform

In order to derive the asymptotic behaviour of the Floquet mode and the form of the cross section, we first summarise necessary assumptions.

At first, we assume the potential $V(\mathbf{r},t)$ to vanish faster than $1/r$ for large r

$$\lim_{r\to\infty} rV(\mathbf{r},t) = 0,\ \forall t \in \mathbb{R}, \tag{5.7}$$

where r is the modulus of the position vector $\mathbf{r}$. Although this condition excludes Coulomb-like potentials, it is necessary for obtaining a simple expression of the asymptotic form of the Floquet mode and covers the in our thesis relevant case of scattering by inter-atomic and short range potentials.

Secondly, a plane wave is considered as an incoming wave function

$$\psi_{\text{in}}(\mathbf{r}) = e^{i\mathbf{kr}}. \tag{5.8}$$

The wave vector $\mathbf{k}$, considered to be parallel to the z-axis, is related to the energy of the plane wave by the dispersion relation for non-relativistic particles

$$E = \frac{\hbar^2}{2m}\mathbf{k}^2. \tag{5.9}$$

We assume the incoming wave to be located in the zeroth Floquet channel

$$\phi_{\text{in}}(\mathbf{r}, t) = \delta_{n,0} e^{i\mathbf{kr}}. \tag{5.10}$$

By comparing the time-evolution of (5.8) and (4.3), we conclude that the energy of the incoming particle equals the Floquet energy

$$E = \epsilon. \tag{5.11}$$

With this consideration we make an ansatz of the asymptotic wave function solving (5.6) in the case of large r. This ansatz reads

$$\phi_n(\mathbf{r}) = \delta_{n,0} e^{i\mathbf{kr}} + f_n \frac{e^{ik_n r}}{r}. \tag{5.12}$$

In this equation the wave vector k_n and the scattering amplitude f_n in the n-th Floquet channel is introduced. The Floquet scattering amplitude f_n depends on the potential, on the driving frequency, on the Floquet energy ϵ and on the solid angle $\Omega = (\theta, \phi)$ of the scattered wave

$$f_n = f_n(\{V_n\}, \omega, \epsilon, \theta, \phi). \tag{5.13}$$

In order to verify the ansatz, we show, that it solves (5.6). The Laplacian of $f_n(\epsilon, \Omega)\frac{e^{ikr}}{r}$ evaluates for the case of large radii to

$$\begin{aligned} \Delta f_n(\epsilon, \Omega) \frac{e^{ik_n r}}{r} &= f_n(\epsilon, \Omega) \frac{1}{r^2} \frac{\partial}{\partial r} r^2 \frac{\partial}{\partial r} \left(\frac{e^{ik_n r}}{r} \right) + \frac{e^{ik_n r}}{r^3} \frac{\partial}{\partial \Omega} f_n(\epsilon, \Omega) \\ &= -k_n^2 f_n(\epsilon, \Omega) \frac{e^{ik_n r}}{r} + \mathcal{O}\left(\frac{1}{r^3} \right) \end{aligned} \tag{5.14}$$

In the next step we assume for simplicity a potential of the form $V_m(\mathbf{r}) = 1/r^{1+\alpha}$ and calculate

$$V_m(\mathbf{r}) \phi_n(\mathbf{r}) = e^{i\mathbf{kr}}/r^{1+\alpha} + e^{ikr}/r^{2+\alpha} = \mathcal{O}\left(\frac{1}{r^{1+\alpha}} \right). \tag{5.15}$$

Condition (5.7) ensures that $\alpha > 0$ and that the influence of the potential on the asymptotic waveform can thus be neglected as r goes to infinity. With those approximations the asymptotic waveform is (5.12) inserted into the coupled-channel equation (5.6)

$$\left(\frac{\hbar^2}{2m} k_n^2 - n\hbar\omega \right) \left(\delta_{n,0} e^{i\mathbf{kr}} + \frac{e^{ikr}}{r} \right) = \epsilon \left(\delta_{n,0} e^{i\mathbf{kr}} + \frac{e^{ikr}}{r} \right) + \mathcal{O}\left(\frac{1}{r^3} \right), \tag{5.16}$$

in order to yield the dispersion relation defining the values of k_n

$$\frac{\hbar^2}{2m} k_n^2 = \epsilon + n\hbar\omega. \tag{5.17}$$

If one works in the centre of mass system, the mass m in equation (5.17) has to be replaced by the reduced mass μ. Due to equation (5.11) we identify k_0 with k. If the right-hand side of 5.17 becomes negative, we get an imaginary $k_n = i\kappa_n$. The asymptotic solution in this Floquet channel is not a spherical wave, but an exponentially decaying solution $f_n e^{-\kappa_n r}/r$.

5.1.3. Cross Section

The goal of this Section is to derive an expression for the time averaged differential and total cross section. The starting point is a general definition of the differential cross section in a time dependent manner similar to (2.4)

$$|\mathbf{j}_{\text{in}}|\frac{d\sigma}{d\Omega}(\Omega,t)|\mathbf{d\Omega}| = \mathbf{j}_{\text{scatt}}(\Omega,t)r^2\mathbf{d\Omega}, \tag{5.18}$$

but we assume an explicit time dependency. For a steady state solution (4.3) the probability current reads

$$\mathbf{j}(\mathbf{r},t) = \frac{\hbar}{2im}\sum_{m,n=-\infty}^{\infty}\left(\phi_m(\mathbf{r})^*\boldsymbol{\nabla}\phi_n(\mathbf{r})e^{-i(n-m)\omega t} - \phi_m(\mathbf{r})\boldsymbol{\nabla}\phi_n(\mathbf{r})^*e^{-i(m-n)\omega t}\right). \tag{5.19}$$

For the incoming plane wave, this evaluates to

$$\mathbf{j}_{\text{in}} = \frac{\hbar\mathbf{k}}{m}. \tag{5.20}$$

In order to determine the probability current of scattered particles, the asymptotic waveform of the scattered wave $f_n(\epsilon,\Omega)e^{ik_nr}/r$ is inserted into expression (5.19). The gradient is evaluated for large r to be

$$\begin{aligned}\boldsymbol{\nabla}f_n(\epsilon,\Omega)\frac{e^{ik_nr}}{r} &= f_n(\epsilon,\Omega)\left(ik_n\frac{e^{ik_nr}}{r} - \frac{e^{ik_nr}}{r^2}\right)\hat{\mathbf{e}}_r + \frac{e^{ik_nr}}{r^2}\frac{\partial f_n(\epsilon,\Omega)}{\partial\Theta}\hat{\mathbf{e}}_\Theta \\ &+\frac{e^{ik_nr}}{r^2\sin(\Theta)}\frac{\partial f_n(\epsilon,\Omega)}{\partial\phi}\hat{\mathbf{e}}_\phi = ik_nf_n(\epsilon,\Omega)\frac{e^{ik_nr}}{r}\hat{\mathbf{e}}_r + \mathcal{O}\left(\frac{\mathbf{1}}{r^2}\right).\end{aligned} \tag{5.21}$$

Inserting this into (5.19), the time-dependent differential cross section is evaluated. As we are interested in the asymptotic behaviour of the wave function, we neglect terms of order $1/r^2$ or higher

$$\frac{d\sigma}{d\Omega}(\epsilon,\Omega,t) = \frac{1}{k}\sum_{m,n=-\infty}^{\infty}\text{Im}\,\left(ik_nf_m^*(\epsilon,\Omega)f_n(\epsilon,\Omega)e^{i(k_n-k_m^*)r}e^{-i(n-m)\omega t}\right). \tag{5.22}$$

This is the most general expression of the differential cross section. In the case of an imaginary wave vector, the corresponding summands $e^{i(k_n-k_m^*)r}$ decay exponentially and do not contributing to the current for large r. In equation (5.22) different summands oscillate with different frequencies in time and wave-vectors in space, as they are created by superposition of different Fourier components of the asymptotic Floquet state. This complicated behaviour is due to the time-dependency of the potential and not monitored in static scattering theory. In the following we assume the driving frequency ω to be large in comparison to the measuring process or the measuring process to be done such often at random times, that it is useful to only consider time averaged quantities $\langle\langle A\rangle\rangle = \frac{1}{T}\int_0^T dtA(t)$. This simplifies the situation dramatically. The time averaged differential cross section is evaluated while using $\frac{1}{T}\int_0^T dt\; e^{i(n-m)\omega t} = \delta_{n,m}$ to be

$$\langle\langle\frac{d\sigma}{d\Omega}\rangle\rangle = \sum_{n\geq n_c}^{\infty}|f_n(\epsilon,\Omega)|^2\frac{k_n}{k}, \tag{5.23}$$

where the critical index n_c is defined by the formula

$$n_c = \left\lceil -\frac{\epsilon}{\omega} \right\rceil , \tag{5.24}$$

which includes the ceiling function $\lceil \bullet \rceil$. This ensures that all k_n with $n \geq n_c$ are real, while all k_n with $n < n_c$ are purely imaginary, such that the sum (5.23) only covers open Floquet channels. As both Floquet energy and driving frequency are positive, definition (5.24) ensures that the critical index is always smaller or equal than zero. In comparison to equation (2.5) of static single-channel scattering theory a sum over the squared modulus of the scattering amplitude f_n of all free channels, weighted by k_n/k, occurs.

A measure of the complete amount of scattered particles is the total cross section σ. It is the integral of the differential cross section over all solid angles

$$\sigma = \int d\Omega \frac{d\sigma}{d\Omega}. \tag{5.25}$$

Using the form of the differential cross section (5.23) the time averaged total cross section can be written in the form

$$\langle\langle \sigma \rangle\rangle = \sum_{n \geq n_c}^{\infty} \langle\langle \sigma_n \rangle\rangle, \tag{5.26}$$

where we have introduced the cross section in in Floquet channel n by

$$\langle\langle \sigma_n \rangle\rangle = \int d\Omega |f_n(\epsilon, \Omega)|^2 \frac{k_n}{k}. \tag{5.27}$$

As the incoming particle is located in the zeroth Floquet channel, no driving-field quanta and therefore energy is added or subtracted, if the particle stays in it and scattering is elastic. Therefore the cross section in Floquet channel zero is considered as the elastic cross section [4]

$$\sigma_{\text{el}} = \langle\langle \sigma_0 \rangle\rangle, \tag{5.28}$$

while the cross Section in channel n is related to inelastic scattering involving n quanta of the driving field. The total inelastic cross section calculates to

$$\sigma_{\text{in}} = \sum_{\substack{n \geq n_c \\ n \neq 0}}^{\infty} \langle\langle \sigma_n \rangle\rangle. \tag{5.29}$$

The scattering amplitudes $f_n(\epsilon, \Omega)$ can be used in order to define a time-dependent scattering amplitude

$$f(t, \epsilon, \Omega) = \sum_{n \geq n_c}^{\infty} e^{-in\omega t} f_n(\epsilon, \Omega), \tag{5.30}$$

and its time-average equals the scattering amplitude in zeroth Floquet channel

$$\langle\langle f \rangle\rangle = f_0. \tag{5.31}$$

In Chapter 7 we will used this quantity in order to observe the enhancement of scattering.

At last we point out the similarities of the coupled-channel picture of Floquet scattering to static multi-channel scattering theory, which is explained for example in Ref. [56, Chapter 3]. In multi-channel scattering theory an equation similar to (5.6) exists, and the shape of the asymptotic wave-forms equal each other if the channels of the multi-channel theory are identified with the Floquet channels. Although multi-channel theory does not include time dependent quantities like in (5.22), the formula for the time-averaged differential cross section (5.23) is similar to the one obtained in static multi-channel scattering theory.

5.2. Floquet-Partial Wave Expansion

Here we generalise the concept of the partial wave expansion to the case of time-periodic scattering. We specialise to spherical symmetric potentials.

5.2.1. Radial-Floquet Equation

Consider a spherical symmetric Hamiltonian $H(\mathbf{r}, t)$, which commutes with the angular momentum operator $\mathbf{L}$ at all times

$$[H(\mathbf{r}, t), \mathbf{L}] = 0 \ \forall t \in \mathbb{R}. \tag{5.32}$$

This implies that $\mathbf{L}$ commutes with all Fourier components (4.8) of the Hamiltonian

$$[H_n(\mathbf{r}), \mathbf{L}] = 0, \forall n \in \mathbb{Z}. \tag{5.33}$$

Using the rules for commutators [84] this result is used in order to prove that the commutator of $\mathbf{L}$ and the Floquet Hamiltonian (4.10) vanishes

$$[\mathcal{H}, \mathbf{L}]_{\mathcal{R}\otimes\mathcal{T}} = 0. \tag{5.34}$$

With this knowledge the eigenfunctions of the angular momentum operator $\mathbf{L}$ can be included in the eigenbasis of $\mathcal{H}$. The eigenfunctions of $\mathbf{L}$ are given by the spherical harmonics $Y_l^m(\Theta, \phi)$. They are parametrised by the quantum number of orbital angular momentum l and its projection m on the quantisation axis.

With this knowledge the Floquet modes and its Fourier components $\phi_{l,n}(r)$ can be decomposed in a radial and angular part

$$\phi_{l,n}(\mathbf{r}) = R_{l,n}(r) P_l(\cos(\theta)), \tag{5.35}$$

where $P_l(z)$ denotes the l-th Legendre polynomial. They appear instead of spherical harmonics, as we assume the incoming plane wave to be directed along the z-axis. In this case the problem is rotational symmetric and therefore the ϕ dependence of the spherical harmonics drops out like

in static scattering theory. By introducing equation (5.35) time dependency is fully put into the radial part of the wave function. After inserting these coefficient functions in the coupled-channel equations (5.6) and separating the angular motion using $\Delta = \Delta_r - \frac{\mathbf{L}^2}{\hbar^2 r^2}$, equation

$$-\frac{\hbar^2}{2m}\Delta_r R_{l,n}(r) + \frac{\hbar^2 l(l+1)}{2mr^2} R_{l,n}(r) + \sum_{m=-\infty}^{\infty} V_m(r) R_{l,n-m}(r) = (\epsilon + n\hbar\omega) R_{l,n}(r) \tag{5.36}$$

is derived as an intermediate step. We denoted with $\Delta_r = \frac{1}{r^2}\frac{\partial}{\partial r} r^2 \frac{\partial}{\partial r}$ the radial part of the Laplacian. Like in the time-independent partial wave expansion, a centrifugal barrier including the angular momentum quantum number l adds to the radial motion. Scaling by $-\frac{2m}{\hbar^2}$, introducing $\frac{\hbar^2}{2m}k_n^2 = \epsilon + n\hbar\omega$ and $v_m(r) = \frac{2m}{\hbar^2}V_m(r)$ leads to the radial Floquet equation

$$\left[\Delta_r + k_n^2 - \frac{l(l+1)}{r^2} - v_0(r)\right] R_{l,n}(r) = \sum_{m\neq 0} v_m(r) R_{l,n-m}(r). \tag{5.37}$$

This equation is central to this thesis, as its solution gives access to all scattering quantities of a given potential. For vanishing right-hand side the special case of time-independent scattering is recovered. In general, the explicitly time-dependent part leads to a coupling of the different Floquet channels. A schematic view on this is given by Figure 5.1. The Fourier components $v_{\pm 1}$ lead to a coupling of nearest neighbour channels, while $v_{\pm 2}$ couples next-nearest neighbours. Although only in the zeroth Floquet channel an incoming wave is present, scattered waves can occur in all free channels due to the periodic driving, where channels supporting imaginary wave vectors posses exponentially decaying wave functions. This structure is similar to static scattering theory but the fact that in Floquet-scattering infinitely many Floquet channels are present [4].

5.2.2. Scattering Amplitudes in Floquet-Partial Wave Expansion

The aim of this Chapter is to derive a closed formula for the scattering amplitudes f_n in the sense of a partial wave expansion, which is presented in Section 2.2.1 in the case of static scattering theory. The beginning of this consideration is the limit of large r of the radial Floquet equation (5.37), where the potential $v_m(r)$ can be neglected, but we do not neglect the centrifugal term. In this case equation (5.37) gets decoupled

$$\left(\Delta_r + k_n^2 - \frac{l(l+1)}{r^2}\right) R_{l,n}(r) = 0. \tag{5.38}$$

This equation can be solved by spherical Hankel functions $h_l^{\pm}(k_n r)$ [85], which are defined by

$$h_l^{\pm}(x) = \mp i(-x)^l \left(\frac{1}{x}\frac{\partial}{\partial x}\right)^l \frac{e^{\pm ix}}{x}, \tag{5.39}$$

and are related to spherical Bessel $j_l(x)$ and Neumann $y_l(x)$ [53, 55] functions by

$$h_l^{\pm}(x) = j_l(x) \pm i y_l(x). \tag{5.40}$$

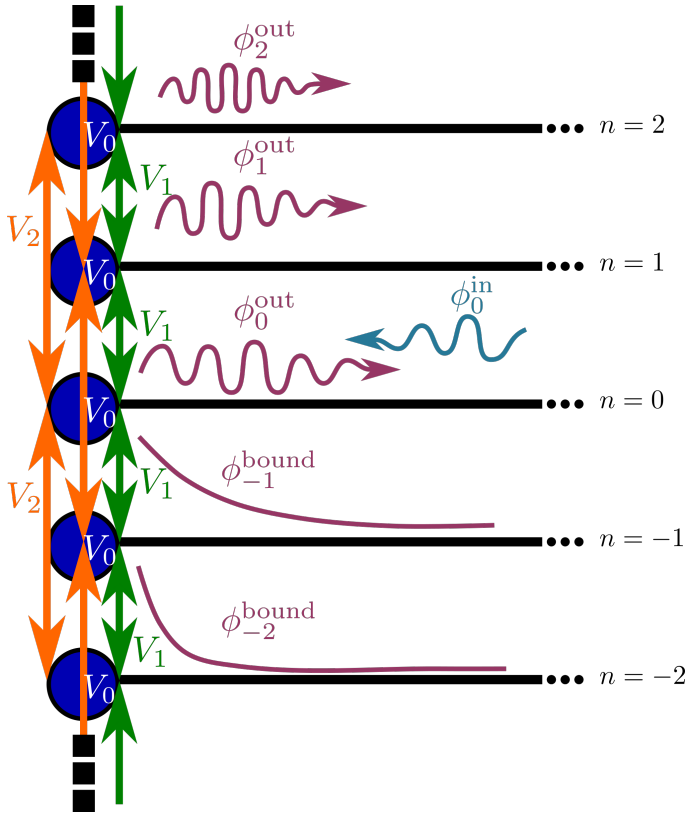

Figure 5.1.: Visualisation of a Floquet-Scattering Process. An incoming wave ϕ_o^{in} is considered in the zeroth Floquet channel. Scattering by the time independent part V_0 (indicated by blue circles) of the potential leads to elastic scattering, where the outgoing wave ϕ_0^{out} stays in the same channel. The first Fourier component V_1 (drawn in green) leads to a coupling of neighbouring Floquet channels, while second component V_2 (drawn in orange) couples next-nearest neighbours. Due to this coupling the particle can be scattered inelastic to higher Floquet channels or become a bound state located in the channels with negative index n. The processes with V_1 involve one quantum of the drive field, while the ones with V_2 involve two. The propagating waves are shown by a wave-package, while the bound states are displayed by an exponentially damped wave function.

The first two spherical Hankel functions are

$$h_0^+(x) = -i\frac{e^{ix}}{x},\ h_0^-(x) = i\frac{e^{-ix}}{x}, \tag{5.41}$$

$$h_1^+(x) = \left(\frac{1}{x} + \frac{i}{x^2}\right)e^{ix},\ h_1^-(x) = \left(\frac{1}{x} - \frac{i}{x^2}\right)e^{-ix}. \tag{5.42}$$

Similar to (2.24), in the limit of large arguments these functions read

$$h_l^{\pm}(x) = \mp\frac{e^{\pm(x-\frac{\pi}{2}l)}}{x}. \tag{5.43}$$

As it is seen from its shape, the spherical Hankel functions with a plus index correspond to incoming waves and the ones with a minus index to outgoing.

The limit of the wave function for large radii is sufficient in order to investigate scattering properties. Therefore we choose as an ansatz for the asymptotic radial wave function a superposition of the asymptotic limit of the spherical Hankel functions

$$R_{l,n}(r) = A_{l,n} i \frac{e^{-i(k_n r - \frac{\pi}{2} l)}}{k_n r} - B_{l,n} i \frac{e^{i(k_n r - \frac{\pi}{2} l)}}{k_n r}. \tag{5.44}$$

If we insert (5.44) into

$$\phi_n(\mathbf{r}) = \sum_{l=0}^{\infty} R_{l,n}(r) P_l(\cos(\theta)), \tag{5.45}$$

we get the asymptotic form of the wave function. In order to be consistent, this should equal equation (5.12)

$$\delta_{n,0} e^{i\mathbf{kr}} + f_n(\epsilon, \theta) \frac{e^{ik_n r}}{r} = \sum_{l=0}^{\infty} \left[A_{l,n} i \frac{e^{-i(k_n r - \frac{\pi}{2} l)}}{k_n r} - B_{l,n} i \frac{e^{i(k_n r - \frac{\pi}{2} l)}}{k_n r} \right] P_l(\cos(\theta)). \tag{5.46}$$

By expanding the plane wave in a sum of angular momenta as in equation (2.12)

$$e^{i\mathbf{kr}} = \sum_{l=0}^{\infty} (2l+1) i^l j_l(kr) P_l(\cos(\theta)) = \sum_{l=0}^{\infty} \frac{2l+1}{2} i^l [h_l^+(kr) + h_l^-(kr)] P_l(\cos(\theta)) \tag{5.47}$$

and expressing $j_l(x)$ via (5.40) and (5.43) by the asymptotic limit of $h_l^{\pm}(x)$, this equation can be rewritten in the form

$$\begin{aligned} f_n(\epsilon, \theta) \frac{e^{ik_n r}}{r} = \sum_{l=0}^{\infty} & \left(B_{l,n} - \frac{2l+1}{2} i^l \delta_{n,0} \right) \frac{-i e^{ik_n r} (-i)^l}{k_n r} P_l(\cos(\theta)) \\ & + \left(A_{l,n} - \frac{2l+1}{2} i^l \delta_{n,0} \right) \frac{i e^{-ik_n r} i^l}{k_n r} P_l(\cos(\theta)) \end{aligned} \tag{5.48}$$

Since the scattered wave only contains outgoing waves, the term in front of the $e^{-ik_n r}$ factor has to vanish. This sets the coefficients $A_{l,n}$ to be

$$A_{l,n} = \frac{2l+1}{2} i^l \delta_{n,0}. \tag{5.49}$$

Thus, the scattering amplitude $f_n(\epsilon, \theta)$ is determined by the coefficients $B_{l,n}$ to be

$$f_n(\epsilon, \theta) = \frac{1}{k_n} \sum_{l=0}^{\infty} (-i)^{l+1} \left[B_{l,n} - \frac{2l+1}{2} i^l \delta_{n,0} \right] P_l(\cos(\theta)) \tag{5.50}$$

Note that the scattering amplitude can be written as a double sum of $f_{l,n}(\epsilon, \theta)$ while using

$$f_{l,n}(\epsilon, \theta) = (-i)^{l+1} [B_{l,n} - \frac{2l+1}{2} i^l \delta_{n,0}] P_l(\cos(\theta). \tag{5.51}$$

By inserting (5.50) into (5.23) the time-averaged differential cross section is calculated by the knowledge of the $B_{l,n}$

$$\langle\langle\frac{d\sigma}{d\Omega}\rangle\rangle = \sum_{n\geq n_c}^{\infty}\frac{1}{k_n k}\sum_{l,l'=0}^{\infty}\left[B^*_{l,n}-\frac{2l+1}{2}(-i)^l\delta_{n,0}\right]\left[B_{l',n}-\frac{2l'+1}{2}i^{l'}\delta_{n,0}\right]P_l(\cos(\theta))P_{l'}(\cos(\theta)) \quad (5.52)$$

The integration over the angle θ by using the orthogonality relation of the Legendre polynomials $\int_{-1}^{1}dzP_l(z)P_{l'}(z)=\delta_{l,l'}\frac{2}{2l+1}$ leads to an expression for the time-averaged total cross section

$$\langle\langle\sigma\rangle\rangle = \sum_{n\geq n_c}^{\infty}\sum_{l=0}^{\infty}\frac{4\pi}{k_n k}\left|B_{l,n}-\frac{2l+1}{2}i^l\delta_{n,0}\right|^2\frac{1}{2l+1}. \quad (5.53)$$

This is similar to expression (2.17) of static scattering theory, but in contrast to (5.53), the scattering phase has been introduced in equation (2.11). We now generalise the concept of the scattering phase $\delta_{l,n}$ to Floquet-scattering theory by defining

$$B_{l,n} = \frac{2l+1}{2}i^l e^{2i\delta_{l,n}}. \quad (5.54)$$

In contrast to the definition in Chapter 2 it is allowed to be complex

$$\delta_{l,n} = \beta_{l,n} + i\gamma_{l,n}. \quad (5.55)$$

The real part $\beta_{l,n}$ of the phase describes a phase shift of the wave function due to the scattering process, while the imaginary part $\gamma_{l,n}$ describes gains and losses due to scattering into and from different Floquet channels. Using the scattering phase according to (5.54) the scattering amplitude can be expressed in the familiar form

$$f_0(\epsilon,\theta) = \frac{1}{k}\sum_{l=0}^{\infty}(2l+1)e^{i\delta_{l,n}}\sin(\delta_{l,n})P_l(\cos(\theta)), \quad (5.56)$$

$$f_n(\epsilon,\theta) = \frac{1}{k_n}\sum_{l=0}^{\infty}\frac{2l+1}{2i}e^{2i\delta_{l,n}}P_l(\cos(\theta)),\ n\neq 0. \quad (5.57)$$

Correspondingly the total cross section reads

$$\langle\langle\sigma\rangle\rangle = \sum_{l=0}^{\infty}\left[\frac{4\pi}{k^2}(2l+1)e^{-2\gamma_{l,0}}|\sin(\delta_{l,0})|^2+\sum_{\substack{n\geq n_c\\ n\neq 0}}^{\infty}\frac{4\pi}{k_n k}(2l+1)\frac{e^{-4\gamma_{l,n}}}{4}\right]. \quad (5.58)$$

This formula shows in an intuitive way the respective contribution of different channels to the Floquet scattering. The channel with the incoming wave $n=0$ contributes to scattering both by phase shift and losses as displayed in the first summand of equation (5.57), while the other channels only contribute through their gain and loss factor $\gamma_{l,n}$.

Similar to equation (2.22) in static scattering theory we define the Floquet-scattering length $a^{\mathrm{Fl}}(t)$ as the negative limit of vanishing energy of the Floquet-scattering amplitude

$$-\lim_{k_0\to 0} f_n(\epsilon,\theta) = a_n^{\mathrm{Fl}}, \tag{5.59}$$

where a_n^{Fl} are the Fourier-coefficients of $a^{\mathrm{Fl}}(t)$. The time averaged scattering length is defined as

$$a_{\mathrm{scatt}} = \langle\langle a^{\mathrm{Fl}}(t)\rangle\rangle = a_0^{\mathrm{Fl}}. \tag{5.60}$$

This definition is central to this thesis, as it allows us to characterise the scattering by a time-dependent potential at low energies by a single parameter. Similar to static scattering theory, s-wave scattering is dominant at low energies in the driven case [4, 80] and because of the additional conservation of angular momentum s-wave scattering is present in all Floquet channels. As s-waves are radial symmetric, the scattering length (5.59) has no dependence on the angle θ.

5.2.3. Floquet-Optical Theorem

In this section we will derive and discuss the Floquet-optical theorem, which will be of great use in Chapter 7. Starting point of its derivation by Floquet-partial wave expansion is to note, that the time-averaged probability current can be separated in partial wave currents $\langle\langle j\rangle\rangle_l$ by

$$\langle\langle \mathbf{j}\rangle\rangle = \sum_{l=0}^{\infty} \langle\langle \mathbf{j}\rangle\rangle_l. \tag{5.61}$$

Inserting the wave function (5.45), while using as radial part the asymptotic form (5.44), and evaluating the Legendre polynomials at forward direction $\theta = 0$, the large r-asymptotic of the time average of the l-wave current is derived to be

$$\langle\langle \mathbf{j}\rangle\rangle_l = \frac{\hbar}{mr^2} \sum_{n\geq n_c}^{\infty} \frac{1}{k_n} \left(|B_{l,n}|^2 - |A_{l,n}|^2\right) \hat{\mathbf{e}}_r + \mathcal{O}\left(\frac{\mathbf{1}}{r^3}\right) \tag{5.62}$$

As in Schrödinger theory no probability is created or destroyed during a scattering process and the different l-wave solutions are decoupled, the integral of each l-wave current over a sphere of radius r_0 vanishes

$$\int d\Omega r^2 \hat{\mathbf{e}}_r \langle\langle \mathbf{j}\rangle\rangle_l = 0. \tag{5.63}$$

The surface integral of $\langle\langle j\rangle\rangle_l$ evaluates to

$$\sum_{n\geq n_c}^{\infty} \frac{4\pi}{k_n} \left(|B_{l,n}|^2 - |A_{l,n}|^2\right) = 0. \tag{5.64}$$

This equation describes the unitary of the scattering process, because it was derived from the vanishing of the probability flux through a surface around the origin. This statement can be refined

further by completing the square $|B_{l,n}|^2 - |A_{l,n}|^2 = |B_{l,n} - A_{l,n}|^2 + 2\text{Re}\ (B_{l,n}A^*_{l,n}) - 2|A_{l,n}|^2$ and inserting (5.49) for $A_{l,n}$ to

$$\sum_{n\geq n_c}^{\infty} \frac{4\pi}{k_n}|B_{l,n} - \frac{2l+1}{2}i^l\delta_{n,0}|^2 = -4\pi(2l+1)\left(\text{Re}\ [B_{l,0}(-i)^l] - \frac{2l+1}{2}\right). \tag{5.65}$$

While multiplying by $\frac{1}{k_0(2l+1)}$ and doing the l-summation, the left-hand side of equation (5.65) is exactly the time-averaged total cross section (5.53), while the right-hand side is proportional to the imaginary part of the Floquet-scattering amplitude (5.50). This yields the Floquet-optical theorem

$$\langle\langle\sigma\rangle\rangle = \frac{4\pi}{k_0}\text{Im}\ f_0(\epsilon, \theta = 0). \tag{5.66}$$

It is very fundamental, as it connects the total cross section to the imaginary part of the scatting amplitude in the zeroth Floquet channel and ensures, like in the static case, the unitary of the Floquet-scattering process. Similar to the static case, the part with Im f_0 originates from an interference term of incoming plane wave and outgoing special wave $2\text{Re}\ (B_{l,n}A^*_{l,n}) - 2|A_{l,n}|^2$, while $\langle\langle\sigma\rangle\rangle$ comes due to the probability current of the scattered wave. This implies, that Floquet-optical theorem does the statement, that losses of probability flux due to the scattered wave are compensated by the interference of plane and scattered wave in forward direction. Note, that only the scattered wave in the zeroth channel, in which also the incoming plane wave is located, contributes to this interference, while the cross section $\langle\langle\sigma\rangle\rangle$ has a contribution of all Floquet channels. Since the probability current (5.61) separates in l-wave currents, Floquet optical theorem can be restated in the case, where $\langle\langle\sigma\rangle\rangle$ and f_0 only cover contributions form l-wave scattering. In the case of s-wave scattering all scattering amplitudes are independent from the angle θ and the total cross section can be directly calculated by multiplying (5.23) with 4π. The Floquet-optical theorem (5.66) can be restated as [4]

$$\text{Im}\ f_0(\epsilon) = \sum_{n\geq n_c}^{\infty} |f_n(\epsilon)|^2 k_n. \tag{5.67}$$

If the zero energy limit of (5.67) is done under the assumption, that all Floquet-scattering amplitudes are not single valued in this limit, we arrive at equation

$$\text{Im}\ a_0^{\text{Fl}} = -\sum_{\substack{n\geq n_c \\ n\neq 0}} |a_n^{\text{Fl}}|^2 k_n. \tag{5.68}$$

This equation states that the imaginary part of the time-averaged Floquet scattering length a_0^{Fl} at zero energy is related to the scattering of particles in higher channels, resulting in losses in the zeroth one. This means that the presence of inelastic scattering can be measured by a non-vanishing imaginary part of the Floquet scattering length in zeroth channel.

5.3. Indistinguishable Particles

In this Section the Floquet-scattering properties of indistinguishable particles are discussed. In the centre-of mass frame, two identical particles are positioned at position $\mathbf{r}$ and $-\mathbf{r}$, so the (anti)-

symmetrised form of a scattering-wave function (5.12) reads

$$\psi^{\pm}(r,\theta,\phi,t) = \frac{1}{\sqrt{2}} e^{-i\epsilon/\hbar t} \left\{ e^{i\mathbf{kr}} \pm e^{-i\mathbf{kr}} + \sum_{n=-\infty}^{\infty} \left[f_n(\epsilon,\theta,\phi) \pm f_n(\epsilon,\pi-\theta,\phi+\pi) \right] \frac{e^{ik_n r}}{r} e^{-in\omega t} \right\}. \tag{5.69}$$

The plus sign used for the case of bosons, while the minus sign gives the case of scalar fermions. As we only deal with scalar fields, both particles have to be spinless or spin polarised. We follow the common definition [52, 56, 86] of normalizing the scattering amplitude by only considering the current in positive $\mathbf{k}$ direction as incoming

$$f_n^{\pm}(\epsilon,\theta,\phi) = \left[f_n(\epsilon,\theta,\phi) \pm f_n(\epsilon,\pi-\theta,\phi+\pi) \right]. \tag{5.70}$$

This scattering amplitude leads a time-averaged differential cross section of

$$\langle\langle \frac{d\sigma}{d\Omega} \rangle\rangle^{\pm} = \frac{1}{2} \sum_{n \geq n_c}^{\infty} |f_n(\epsilon,\theta,\phi) \pm f_n(\epsilon,\pi-\theta,\phi+\pi)|^2 \frac{k_n}{k}, \tag{5.71}$$

where the factor of $1/2$ comes due to normalisation issues [56], with that the time-averaged total cross section $\langle\langle\sigma\rangle\rangle^{\pm}$ can be defined as the integral over the full solid angel of (5.71).

In the case of low energy physics we get as the s-wave scattering length $a^{\pm}_{\text{scatt}}$

$$a^{+}_{\text{scatt}} = 2a_{\text{scatt}} \tag{5.72}$$

for bosons and

$$a^{-}_{\text{scatt}} = 0 \tag{5.73}$$

for fermions.

We now arrived the end of this Section and we do a short summary of the most important findings. We treated the general form of scattering by a time-periodic potential and observed, that with the usage of Floquet theory the time-dependent scattering problem can be mapped to a static multi-channel problem with infinitely many channels. We were able to extend partial-wave expansion to scattering by time-periodic potentials and showed how this theory can be used in order to calculate cross sections and the scattering length in principle. In the next Chapter we apply this theory to a simple model potential, where we find a solution of the scattering problem in a closed form. This solution is used in Chapter 7 to observe the strong enhancement of scattering by periodic driving.

6. Contact Potential with Driven Scattering Length

In this Chapter we apply the framework of Floquet-partial wave expansion to a special scattering potential, named contact potential, which is interesting to investigate, as it possesses a simple solution in a closed form while featuring interesting and non-trivial properties if periodically driven. We therefore introduce in Section 6.1 the contact potential, which describes the scattering of particles in the low energy limit and the regime of s-wave scattering. In Section 6.2 we solve the corresponding radial-Floquet equation and map the driven scattering problem to a recursion relation. Section 6.3 comprises a discussion of the scale invariance of the derived recursion and a rescaling in convenient length and energy scales. Finally, in Section 6.4 we present a method, which can be used in order to solve the recursion relation numerically for general frequencies, and derive approximate analytic expressions in the limit of small and large driving frequencies.

In this Chapter we solely discuss the methods of solving the radial Floquet equation describing scattering by a time-periodic contact potential, while a detailed discussion of the results of this investigation is done in Chapter 7.

6.1. Driven Contact Potential

As a suitable generalisation of the one-dimensional delta potential (1.2), which is describing the inter-particle interaction in the case of scattering of ultracold atoms [38,55], we introduce the contact potential

$$V(\mathbf{r},t) = \frac{2\pi\hbar^2 a(t)}{\mu}\delta^3(\mathbf{r})\frac{\partial}{\partial r}r \tag{6.1}$$

as a time-dependent scattering potential. Here $a(t)$ denotes the s-wave scattering length, which is time-dependent in our case, and μ the reduced mass. The contact potential includes a radial derivative $\frac{\partial}{\partial r}$, which acts on radius r times the wave function, in order to overcome a $1/r$ divergence of wave functions in the origin. The contact potential is constructed for the case of s-wave scattering and is thus valid in the low-energy limit, where the de-Broglie wavelength of the scattered particle is much larger than the relevant length scales of an actual inter-atomic potential. Therefore, it is a simplified model, where the effect of a more complicated inter-atomic potential is only present at the origin and described by the instantaneous scattering length $a(t)$ [4]. A more detailed discussion

of the contact potential is given in Appendix A. In the following we assume the scattering length to be driven sinusoidally

$$a(t) = \bar{a} + a_1 \cos(\omega t), \tag{6.2}$$

with the driving frequency ω, the time-averaged scattering length $\bar{a}$ and the driving amplitude a_1. We focus on the parameter range of $a_1 < |\bar{a}|$, as we only want to consider the case, where the contact interaction is either attractive or repulsive over the whole driving period.

In contrast to static scattering theory, the Floquet state consists of a superposition of wave functions in different Floquet channels, and therefore the de-Broglie wavelength $\lambda_n = 2\pi/k_n$ in all relevant channels should be larger than the typical length scale r_{pot} of the potential

$$k_n r_{\text{pot}} \ll 1 \tag{6.3}$$

in order to justify the approximation of a actual inter-atomic potential by the contact interaction. In the case of ultracold gases the inter-atomic potential is given by the van der Waals potential and the typical length scale of the potential r_{pot} is given by the van der Waals length r_{vdW} [38]. Introducing the energy scale of the potential by

$$E_{\text{pot}} = \frac{\hbar^2}{2\mu} \frac{1}{r_{\text{pot}}^2} \tag{6.4}$$

and using the dispersion (5.17), while assuming that the Floquet channels relevant in the scattering process are of order one, we rewrite (6.3) in a more convenient form

$$\hbar\omega \ll E_{\text{pot}}. \tag{6.5}$$

This condition also ensures the adiabaticity of the driving procedure in energy scales of the potential [4, 87] and therefore validates the approximation of a time-dependent inter-atomic potential by an instantaneous scattering length.

Following Refs. [54, 88], we make the choice of

$$\int_0^\infty dr \delta(r) = \frac{1}{2} \tag{6.6}$$

and derive the delta distribution identity

$$4\pi \int_0^\infty dr\ r^2 \delta^3(\mathbf{r}) = \int_{\mathbb{R}^3} d^3\mathbf{r} \delta^3(\mathbf{r}) = 1 = 2 \int_0^\infty dr \delta(r), \tag{6.7}$$

in order to relate the radial delta function to the three-dimensional one

$$\frac{1}{2\pi r^2} \delta(r) = \delta^3(\mathbf{r}). \tag{6.8}$$

With identity (6.8) and a scaling by $2\mu/\hbar^2$, the non-vanishing Fourier components of the scaled potential $v(r,t)$ can be expressed only by the modulus r of the position vector

$$v_0(r) = 2\frac{\bar{a}}{r^2} \delta(r) \frac{\partial}{\partial r} r \tag{6.9}$$

$$v_{\pm 1}(r) = \frac{a_1}{r^2} \delta(r) \frac{\partial}{\partial r} r. \tag{6.10}$$

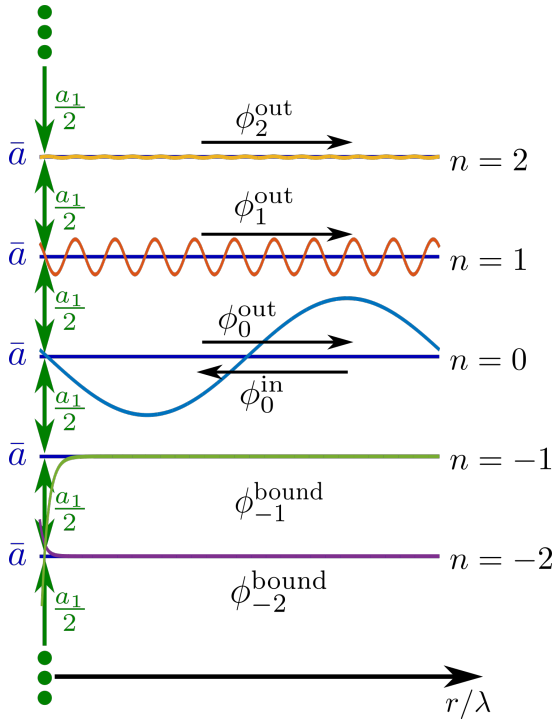

Figure 6.1.: Scetch of the actual wave function in different Floquet channels for a periodically driven contact potential in the case of $\tilde{\epsilon} = 10^{-2}$, $\tilde{\omega} = 1$ and $\tilde{a}_1 = 0.1$. We consider an incoming wave with wavelength λ to be located in the zeroth Floquet channel. Due to the periodic modulation of the potential (6.10) the wave can be scattered inelastically in higher Floquet channels. Additionally the drive creates bound states in the Floquet channels with negative index. Although these bound states have a vanishing probability current, they affect the scattering properties remarkably.

In order to keep the following calculation on the most general level, we consider the case of distinguishable particles.

6.2. Derivation of Recursion Relation

The following derivation of a recursion relation is starting with the radial Floquet equation in the case of s-wave scattering (5.37) with a driven contact potential.

$$\left[\Delta_r + k_n^2 - 2\frac{\bar{a}}{r^2}\delta(r)\frac{\partial}{\partial r}r\right] R_n(r) = 2\frac{a_1}{2r^2}\delta(r)\frac{\partial}{\partial r}r\left[R_{n+1}(r) + R_{n-1}(r)\right]. \tag{6.11}$$

As s-waves correspond to total angular momentum $l = 0$, no centrifugal term appears in equation (6.11) and we will omit this l-index in the wave function in the further calculation by writing $R_n(r) = R_{l=0,n}(r)$. For $r \neq 0$ the radial-Floquet equation can be solved by spherical Hankel functions

(5.11) with index $l = 0$:

$$R_n(r) = C_n \frac{ie^{-ik_n r}}{k_n r} - D_n \frac{ie^{ik_n r}}{k_n r}. \tag{6.12}$$

Like in Chapter 5 we consider an incoming plane wave in the zeroth Floquet channel with energy

$$E = \frac{\hbar^2}{2\mu} k^2. \tag{6.13}$$

Due to the considerations made in (5.11) this incident energy E equals the Floquet energy ϵ. According to equation (5.49) the coefficients C_n have the form

$$C_n = \frac{\delta_{n,0}}{2}. \tag{6.14}$$

As visualised in Figure 6.1 the wave functions in higher Floquet channels posses a larger wave vector, while those in lower have an imaginary one leading to bound wave functions localised around the origin, which read

$$R_n(r) = -D_n \frac{e^{-\kappa_n r}}{\kappa_n r}. \tag{6.15}$$

Here we defined $k_n = i\kappa_n$. As the other summand in (6.12) would lead to an exponentially growing solution, it is omitted in (6.15). The coefficients D_n are obtained by investigating the behavior at the origin by integrating over a small volume located around it. Therefore equations (6.9), (6.10,(6.12) are inserted into equation (6.11), multiplied by r^2 and integrated over the radius r

$$\begin{aligned} &\int_0^{\epsilon_r} dr\ r^2 \left(\Delta_r + k_n^2 - 2\frac{\bar{a}}{r^2}\delta(r)\frac{\partial}{\partial r} r \right) R_n(r) = \\ &\int_0^{\epsilon_r} dr\ r^2 \left(2\frac{a_1}{2r^2}\delta(r)\frac{\partial}{\partial r} r[R_{n+1}(r) + R_{n-1}(r)] \right), \end{aligned} \tag{6.16}$$

where ϵ_r is a small, but finite parameter. We are going to evaluate this integral piecewise. In order to obtain the part involving the radial Laplacian, we rewrite the integration as a volume integral over the Laplacian on a sphere with radius ϵ_r

$$\int_0^{\epsilon_r} dr\ r^2 \Delta_r R_n(r) = \frac{1}{4\pi} \int_{B_{\epsilon_r}(0)} d^3 r \Delta R_n(r). \tag{6.17}$$

This step is possible as the s-wave character of the ansatz function (6.12) includes no contribution of the total angular momentum operator $\mathbf{L}^2$ in the Laplacian. To the right-hand side of equation (6.17) we apply Gauss theorem and transform it to a surface integral

$$\frac{1}{4\pi} \int_{B_{\epsilon_r}(0)} d^3 r \Delta R_n(r) = \frac{1}{4\pi} \int_{\partial B_{\epsilon_r}(0)} d\Omega\ r^2 \frac{\partial}{\partial r} R_n(r). \tag{6.18}$$

The surface integral leads to the radial derivative of the wave function evaluated at $r = \epsilon_r$. Inserting the ansatz functions (6.12) and performing the limit of vanishing ϵ_r we arrive at

$$\int_0^{\epsilon_r} dr\ r^2 \Delta_r R_n(r) = r^2 \frac{\partial}{\partial r} R_n(r) \Big|_{r=\epsilon_r} \overset{\epsilon_r \to 0}{\longrightarrow} \frac{i}{k_n} \left(D_n - C_n \right). \tag{6.19}$$

The second part of equation (6.16), which is proportional to k_n^2 vanishes in the limit of ϵ_r going to zero, as the integral is also proportional to ϵ_r^2.

The integral over the contact potential evaluates to

$$\int_0^{\epsilon_r} dr\ r^2 \frac{1}{r^2}\delta(r)\frac{\partial}{\partial r} r \frac{e^{\pm ikr}}{kr} = \pm \int_0^{\epsilon_r} dr \delta(r) i e^{\pm ikr} = \pm \frac{i}{2}. \tag{6.20}$$

Using this intermediate step in the remaining terms of (6.16) we receive as result

$$\int_0^{\epsilon_r} dr\ r^2 v_0(r) R_n(r) \quad \overset{\epsilon_r \to 0}{\longrightarrow} \quad \bar{a}(C_n + D_n), \tag{6.21}$$

$$\int_0^{\epsilon_r} dr\ r^2 v_{\mp} 1(r) R_{n\pm 1}(r) \quad \overset{\epsilon_r \to 0}{\longrightarrow} \quad \frac{a_1}{2}(C_{n\pm 1} + D_{n\pm 1}). \tag{6.22}$$

With $C_n = \delta_{n,0}/2$ and equations (6.19), (6.21) and (6.22) the radial Floquet equation (6.11) can be transformed to a recursion relation for the coefficients of the outgoing spherical waves

$$\left(\frac{i}{k_n \bar{a}} - 1\right) D_n - \frac{a_1}{2\bar{a}} \left(D_{n+1} + D_{n-1}\right) = g_n, \tag{6.23}$$

where the inhomogeneity is given by

$$g_n = \left(\frac{i}{k_n \bar{a}} + 1\right) \frac{\delta_{n,0}}{2} + \frac{a_1}{2\bar{a}} \left(\frac{\delta_{n+1,0}}{2} + \frac{\delta_{n-1,0}}{2}\right). \tag{6.24}$$

This inhomogeneous recursion relation is linear in the coefficients D_n and relates three of them with neighboring indices n, $n+1$ and $n-1$. Due to the factor $i/k_n - \bar{a}$, being non-linear in the Fourier index n, the recursion can not be solved analytically. The inhomogeneity (6.24) is only located at the indices $n = 0, \pm 1$ and ensures, that the solution of (6.23) does not completely vanish. As the norm of the Floquet mode (4.18) includes a sum over its Fourier components, the coefficients D_n have to converge to zero in order to obtain a finite norm of the corresponding Floquet state. This imposes the following boundary condition for the coefficients D_n

$$\lim_{n \to \pm\infty} D_n = 0. \tag{6.25}$$

If the ansatz (6.12) is compared with the asymptotic solutions of the radial Floquet equation (5.44) and (5.41), it will be seen that the D_n coefficients coincide with the $B_{0,n}$ of equation (5.44) and therefore the scattering amplitude can be calculated by

$$f_n^{\mathrm{s-wave}}(\epsilon) = \frac{-i}{k_n}\left(D_n - \frac{1}{2}\delta_{n,0}\right). \tag{6.26}$$

Equation (6.23) combined with convergence condition (6.25) is central to this thesis, as it allows us to calculate the scattering amplitudes, and with them all further scattering quantities of interest, for arbitrary driving frequency.

6.3. Scale Invariance of Recursion

It can be read off that equation (6.23) with the inhomogeneity (6.24) is invariant under the following scale transformation

$$k_n \rightarrow \beta k_n, \tag{6.27}$$
$$\bar{a} \rightarrow \frac{\bar{a}}{\beta}, \tag{6.28}$$
$$a_1 \rightarrow \frac{a_1}{\beta}. \tag{6.29}$$

Using the dispersion relation (5.17) the transformation can be extended to the Floquet energy ϵ and the driving frequency ω by

$$\epsilon \rightarrow \beta^2 \epsilon, \tag{6.30}$$
$$\omega \rightarrow \beta^2 \omega. \tag{6.31}$$

With this scale invariance we eliminate the explicit dependency of the recursion relation on the time-averaged scattering length $\bar{a}$. We therefore choose to rewrite the recursion relation in units of energy and length scales, which are convenient for this setting. Starting point is measuring the wave vector in units of inverse $\bar{a}$

$$\tilde{k}_n = k_n \bar{a}, \tag{6.32}$$

which can be rewritten as

$$k_n \bar{a} = \operatorname{sign}(\bar{a}) \sqrt{\frac{\epsilon + n\hbar\omega}{\frac{\hbar^2}{2m}} \bar{a}^2} = \operatorname{sign}(\bar{a}) \sqrt{\frac{\epsilon}{E_\mathrm{D}} + n \frac{\hbar\omega}{E_\mathrm{D}}}. \tag{6.33}$$

This determines the energy scale of the problem, which we introduced by the dimer energy

$$E_\mathrm{D} = \frac{\hbar^2}{2m} \frac{1}{\bar{a}^2}. \tag{6.34}$$

It is defined as the binding energy of the bound state, which the contact potential supports for positive value of $\bar{a}$ and is discussed in more detail in Appendix A. It is convenient to measure energy and frequency in units of the dimer energy

$$\tilde{\epsilon} = \frac{\epsilon}{E_\mathrm{D}}, \ \hbar\tilde{\omega} = \frac{\hbar\omega}{E_\mathrm{D}}. \tag{6.35}$$

At last by introducing

$$\tilde{a}_1 = \frac{a_1}{\bar{a}} \tag{6.36}$$

the driving amplitude is measured in units of $\bar{a}$. With these considerations the recursion relation (6.23) and the inhomogeneity (6.24) can be solely rewritten in terms of dimensionless quantities

$$\left(\frac{i}{\tilde{k}_n} - 1 \right) D_n - \frac{\tilde{a}_1}{2} \left(D_{n+1} + D_{n-1} \right) = \tilde{g}_n. \tag{6.37}$$

Here the inhomogeneity is given by

$$\tilde{g}_n = \left(\frac{i}{\tilde{k}_n} + 1\right)\frac{\delta_{n,0}}{2} + \frac{\tilde{a}_1}{2}\left(\frac{\delta_{n+1,0}}{2} + \frac{\delta_{n-1,0}}{2}\right). \tag{6.38}$$

Also condition (6.25) has to be fulfilled for a solution D_n of (6.37). By rewriting the recursion relation in the form (6.37) the dependency of the averaged scattering length $\bar{a}$ has been eliminated and only that on $\tilde{a}_1$, $\tilde{w}$ and $\tilde{\epsilon}$ remain. Although we emphasised the importance of equation (6.23), we will prefer equation (6.37) to (6.23), as it involves one free parameters less than (6.23), while both equations possess the same solution D_n.

Also the scattering amplitude can be measured in units of $\bar{a}$

$$\tilde{f}_n = \frac{f_n}{\bar{a}}, \tag{6.39}$$

and equation (6.26) reads

$$\tilde{f}_n(\epsilon) = \frac{-i}{\tilde{k}_n}\left(D_n - \frac{1}{2}\delta_{n,0}\right). \tag{6.40}$$

But there is one disadvantage remaining in equation (6.37). If $\tilde{k}_n = 0$ for one $n \in \mathbb{Z}$ the fraction $i/\tilde{k}_n$ becomes infinitely large. A special case, where this happens is the low-energy limit, where k_0 tends to zero. Therefore it is useful to solve the expression of the scattering amplitude (6.26) for the D_n coefficients

$$D_n = i\tilde{k}_n\tilde{f}_n + \frac{\delta_{n,0}}{2} \tag{6.41}$$

and insert it into (6.37) in order to get a recursion relation directly for the scattering amplitudes $\tilde{f}_n$.

$$-(1 + i\tilde{k}_n)\tilde{f}_n - \frac{i\tilde{a}_1}{2}(\tilde{k}_{n+1}\tilde{f}_{n+1} + \tilde{k}_{n-1}\tilde{f}_{n-1}) = \delta_{n,0} + \frac{\tilde{a}_1}{2}(\delta_{n+1,0} + \delta_{n-1,0}) \tag{6.42}$$

This way of writing down the recursion has the disadvantage of having more $\tilde{k}_n$ terms involved, which are nonlinear in n, but it has the advantage of being defined at the point $\tilde{k}_0 = 0$. Note that (6.42) coincides with the result obtained by a Bethe-Peierls boundary condition approach by Ref. [4].

6.4. Solution Methods for the Recursion Relation

Due to the term $i/\tilde{k}_n - 1$ in (6.37), which is non-linear in the index n of the recursion, no method has been found to solve the recursion (6.37) analytically in the general case. We therefore present methods which solve the recursion numerically or approximately in the limit of small and large driving frequencies.

6.4.1. Truncation to Linear Set of Equations

In order to treat (6.37) and (6.38) numerically, they are first transformed to a set of linear equations of infinite size

$$\underline{\underline{A}}\mathbf{D} = \mathbf{g}. \tag{6.43}$$

The solution vector $\mathbf{D}$ has the components D_n, while the index n is considered as an integer. The infinitely sized matrix $\underline{\underline{A}}$ is tridiagonal with the matrix elements

$$A_{n,n} = \frac{i}{\tilde{k}_n} - 1, \; A_{n,n\pm1} = -\frac{\tilde{a}_1}{2}. \tag{6.44}$$

The inhomogeneity vector $\mathbf{g}$ possesses the non-vanishing components

$$g_0 = \left(\frac{i}{\tilde{k}_n} + 1\right), \; g_{\pm1} = \frac{\tilde{a}_1}{4}. \tag{6.45}$$

In order to solve (6.37) numerically, the infinite linear set of equations (6.43) is truncated to a finite one. This approach is useful due to boundary condition (6.25) and states that the approximative solution vanishes even at a finite cut-off index m, that means it holds $D_n = 0$ for $|n| > m$. Additionally the matrix elements $A_{n,m}$ are set to zero for $|n| > m$. The resulting finite set of linear equations looks formally like (6.43) and can be solved by numerical algorithms. We implemented a MATLAB function, to which we will further refer as numerical method, using the backslash operator [89] $\mathbf{D} = \underline{\underline{A}}\backslash\mathbf{g}$ in order to solve the finite set of linear equations. In order to check if the cut-off m is sufficiently large, we test numerically if the solution of the finite linear set of equations lies near zero for indices close to the cut-off on both sides. If it does, the solution is considered to be correct inside the numerical errors, if not a new calculation using a larger cut-off needs to be done. In Figure 6.2 both real and imaginary part of the solution of the recursion relation (6.37) are depicted. In this case the coefficients D_n converge to zero even in the range of index numbers for $m = 10$.

Note, that also equation (6.42) can be truncated in the same manner to

$$\underline{\underline{B}}\mathbf{f} = \boldsymbol{\gamma}. \tag{6.46}$$

Again, $\underline{\underline{B}}$ is a tridiagonal matrix with matrix elements of

$$B_{n,n} = -(1 + i\tilde{k}_n), \; B_{n,n\pm1} = -\frac{i\tilde{a}_1}{2}\tilde{k}_{n\pm1} \tag{6.47}$$

and the non-zero vector components are given by

$$\gamma_0 = 1, \; \gamma_{\pm1} = \tilde{a}_1. \tag{6.48}$$

6.4.2. Limit of Large Driving Frequencies

In the limit of infinite large driving frequencies $\tilde{\omega}$ we find an analytical expression, which approximately solves the recursion relation (6.37). Starting point is the behaviour of the wave vector

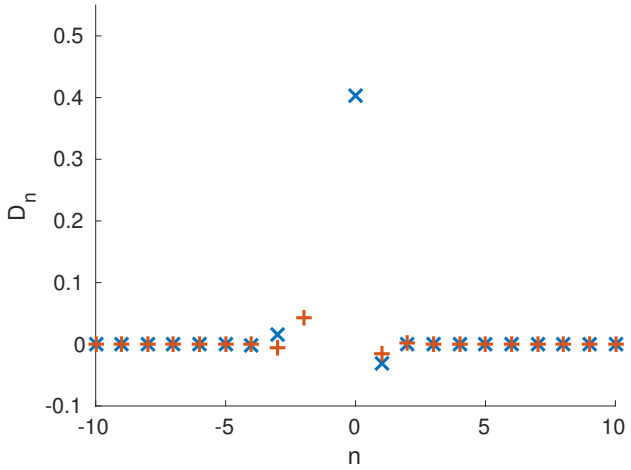

Figure 6.2.: Plot of real (blue) and imaginary (red) part of the solution D_n of (6.37) for $\tilde{\epsilon} = 0.1$, $\tilde{\omega} = 1$ and $\tilde{a}_1 = 0.1$.

$\tilde{k}_n = \sqrt{\tilde{\epsilon} + n\hbar\tilde{\omega}}$ in this case, which tends for $n \neq 0$ towards infinity, but for $n = 0$ it equals $\sqrt{\tilde{\epsilon}}$. Inserting this limit into (6.37), it simplifies in a dramatic way, as the non-linear n-dependence vanishes. For $|n| > 1$ the simplified recursion reads

$$D_n + \frac{\tilde{a}_1}{2}(D_{n+1} + D_{n-1}) = 0, \tag{6.49}$$

while for the rest of the indices we still remain with (6.37). Equation (6.49) is solved by the exponential ansatz $D_n = \Lambda_\pm^{|n|}$, where $\Lambda_\pm$ has the values

$$\Lambda_\pm = \frac{-1 \pm \sqrt{1 - \tilde{a}_1^2}}{\tilde{a}_1}. \tag{6.50}$$

They fulfil $\Lambda_+\Lambda_- = 1$. Additionally $\Lambda_\pm$ are real provided that $\tilde{a}_1 \leq 1$ and complex in the other case, where it holds $|\Lambda_\pm| = 1$. This is not leading to a converging solution of the recursion for large absolute values of n. We therefore stay in the case of $\tilde{a}_1 < 1$, where $|\Lambda_+| < 1$. The solution of the recursion in the high frequency limit is thus given by

$$D_n = \alpha\Lambda_+^{|n|}, \ n \geq 1, \tag{6.51}$$

$$D_n = \beta\Lambda_+^{|n|}, \ n \leq 1. \tag{6.52}$$

Recursion (6.37) with indices $n = -1, 0, 1$ is used in order to determine the values of α and β together with D_0. With the ansatz (6.51), (6.52) these equations are written as a set of linear equations

$$\begin{pmatrix} \Lambda_+ + \frac{\tilde{a}_1}{2}\Lambda_+^2 & \frac{\tilde{a}_1}{2} & 0 \\ -\frac{\tilde{a}_1\Lambda_+}{2} & \frac{i}{k_0} - 1 & -\frac{a_1}{2}\Lambda_+ \\ 0 & \frac{\tilde{a}_1}{2} & \Lambda_+ + \frac{\tilde{a}_1}{2}\Lambda_+^2 \end{pmatrix} \begin{pmatrix} \alpha \\ D_0 \\ \beta \end{pmatrix} = \begin{pmatrix} -\frac{\tilde{a}_1}{4} \\ \frac{1}{2}\left(\frac{i}{k_0} + 1\right) \\ -\frac{\tilde{a}_1}{4} \end{pmatrix}, \tag{6.53}$$

which is solved uniquely by

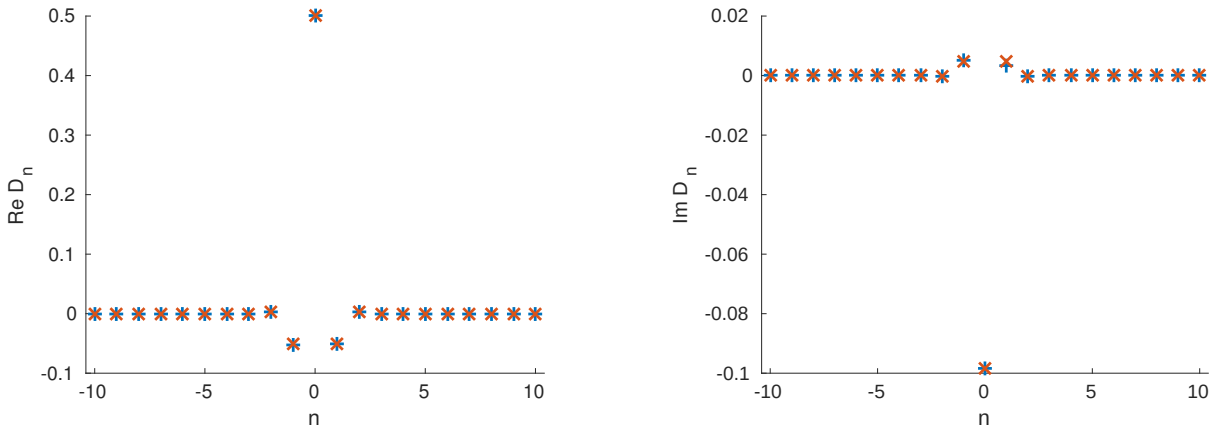

(a) **(b)**

Figure 6.3.: Plot of the real part **(a)** and the imaginary part **(b)** of the sequence D_n using the numerics (blue) and the high frequency limit (red) at $\hbar\tilde{\omega} = 1000$, $\tilde{\epsilon} = 0$, $\tilde{a}_1 = 0.1$.

$$\alpha = \beta = -\frac{i}{\sqrt{1-\tilde{a}_1^2}\tilde{k}_0 - i}, \tag{6.54}$$

$$D_0 = \frac{\sqrt{1-\tilde{a}_1^2}\tilde{k}_0 + i}{-2\sqrt{1-\tilde{a}_1^2}\tilde{k}_0 + 2i}. \tag{6.55}$$

For large frequencies, like $\hbar\tilde{\omega} = 1000$, which is used in Figure 6.3, the high frequency solution fits very well to the numerical one. The case of lower frequencies can be spotted in Figure 6.4. There the difference gets larger, especially for those coefficients D_n with small but finite n. A detailed discussion of the resulting scattering amplitude is done in Section 7.7.

6.4.3. Limit of Low Driving Frequencies

Similar to the considerations in the previous Subsection we derive a closed formula for the coefficients D_n, which solve the recursion (6.37) approximately in the limit of low frequencies. Following [90] we consider in this limit driving frequencies $\hbar\tilde{\omega}$ being much smaller than the Floquet energy $\tilde{\epsilon}$, such that the condition

$$n\hbar\tilde{\omega} \ll \epsilon, \tag{6.56}$$

is fulfilled for all indices n with a coefficient D_n of relevant weight. Numerical experiments show, that for small driving frequencies these indices are located close to zero. As an example, Figure 6.5 shows the case of $\tilde{\epsilon}/\tilde{\omega} = 10^4$, where only the $n = 0$ index differs from zero in a relevant way. We therefore assume that we can neglect the driving-frequency dependency of the wave-vector $\tilde{k}_n$ and do the approximation

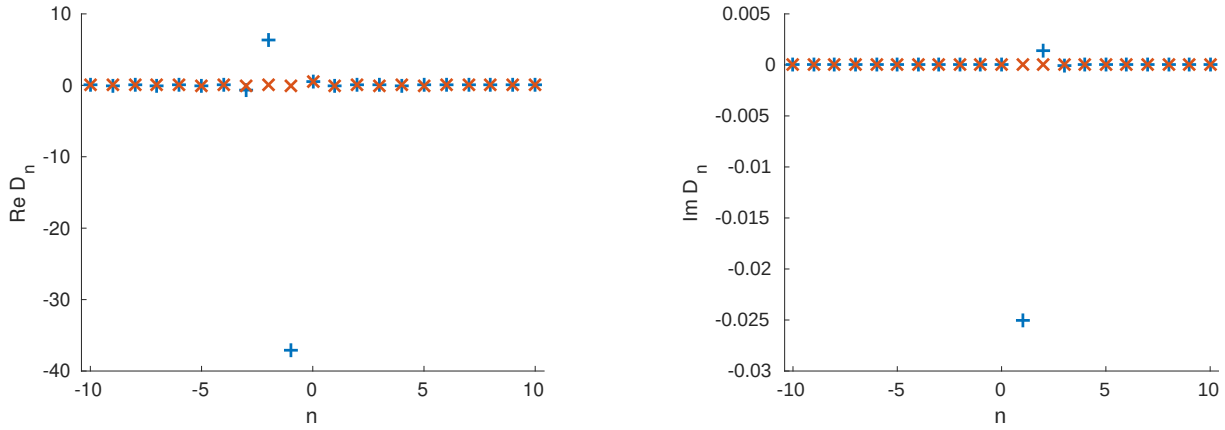

(a) **(b)**

Figure 6.4.: Plot of the real part **(a)** and the imaginary part **(b)** of the sequence D_n using the numerics (blue) and the formula for high frequencies (red) close to a resonance. In this case the approximation does not coincide with the numerical solution. We used $\hbar\tilde{\omega} = 1.02$, $\tilde{a}_1 = 0.1$ and $\tilde{\epsilon} = 0$ as parameters.

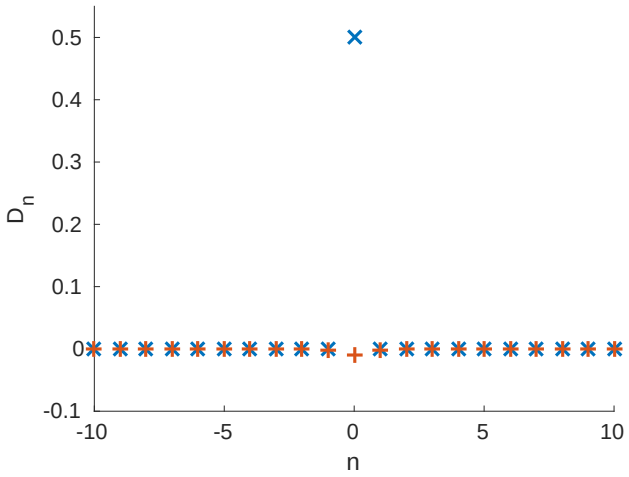

Figure 6.5.: Real (blue) and imaginary (red) part of the recursion relation (6.37) in the case of $\tilde{a}_1 = 0.4$, $\tilde{\epsilon} = 10^{-4}$ and $\tilde{\omega} = 10^{-8}$.

$$\tilde{k}_n \approx \tilde{k}_0. \tag{6.57}$$

In this limit (6.37) is written

$$\left(\frac{i}{\sqrt{\tilde{\epsilon}}} - 1\right) D_n - \frac{\tilde{a}_1}{2} \left(D_{n+1} + D_{n-1}\right) = \tilde{g}_n, \tag{6.58}$$

where the inhomogeneity $\tilde{g}_n$ is defined in equation (6.38). Similar to (6.49) we can solve this equation by assuming an exponential ansatz

$$D_n = \alpha \Lambda_+^{|n|}, \; n \geq 1 \tag{6.59}$$

$$D_n = \beta \Lambda_+^{|n|}, \; n \leq 1, \tag{6.60}$$

where Λ_+ is equal to

$$\Lambda_+ = \frac{\left(\frac{i}{k_0} - 1\right) + \sqrt{\left(\frac{i}{k_0} - 1\right)^2 - \tilde{a}_1^2}}{\tilde{a}_1}. \tag{6.61}$$

Plugging this ansatz into (6.37), the remaining parameters α, β, D_0 are calculated to be

$$\alpha = \beta = -\frac{i}{\tilde{k}_0 \sqrt{-\tilde{a}_1^2 + \frac{(\tilde{k}_0 - i)^2}{\tilde{k}_0^2}}}, \tag{6.62}$$

$$D_0 = -\frac{1}{2} + \frac{i\tilde{k}_0 \sqrt{-\tilde{a}_1^2 + \frac{(\tilde{k}_0 - i)^2}{\tilde{k}_0^2}}}{\left(\tilde{a}_1^2 - 1\right) \tilde{k}_0^2 + 2i\tilde{k}_0 + 1}. \tag{6.63}$$

These equations are used in Section 7.8 for a detailed investigation of the low frequency limit of scattering by a driven contact potential.

We now do a short summary: In this Chapter we mapped the radial Floquet equation (6.11) to recursion relation (6.37), which is used in order to calculate all quantities of interest. This was possible, as we dealed by the contact interaction with a local potential. Recursion (6.11) can be solved numerically for arbitrary driving frequencies and analytically in the limit of high and low driving frequencies. In the next Chapter we use this results in order to calculate the time-averaged scattering amplitude (5.30) and both total (5.26) and elastic cross (5.28) sections and observe, that scattering can be enhanced in the vicinity of so-called driving induced scattering resonances.

7. Enhancement of Scattering by Periodic Driving

In this Chapter we use the results of Chapter 6 in order to investigate the Floquet-scattering amplitude (6.40), which results from scattering by a driven contact potential and can be calculated by recursion (6.37). In Section 7.1 we give an overview of the quantities and settings of interest and spot the emergence of so-called scattering resonances. Section 7.2 is dedicated to the deeper understanding of these resonances. There we find an explanation of their emergence by the occurrence of bound states in the continuum, which are induced by periodic driving. This consideration lays the basis for Section 7.3, where we investigate the position of the scattering resonances. In Section 7.4 we introduce two formulas, which approximate the scattering amplitude in the vicinity of those resonances. An evaluation of position and width of the scattering resonances is given in Section 7.5. We focus on the limit of vanishing Floquet energy and investigate the resonances in the plane spanned by the driving strength $\tilde{a}_1$ and the driving frequency $\tilde{\omega}$. We report in Section 7.6 that real and imaginary part of the Floquet-scattering amplitude are connected by Kramers-Kronig like relations. Section 7.7 provides a short discussion of the large frequency limit, while Section 7.8 deals with the case of small frequencies.

7.1. Overview

Like in Chapter 6 we focus on case of low-energy physics in the s-wave regime and therefore omit the angular momentum index l in this Chapter. Moreover, we measure all quantities, which are marked by a tilde, in dimensionless units, which we defined in equations (6.35), (6.36) and (6.39). As it can be used to calculate all quantities of interest, we focus our research on the time average of the Floquet scattering amplitude (5.30)

$$\langle\langle \tilde{f}(t) \rangle\rangle = \tilde{f}_0, \tag{7.1}$$

which is equal to the Floquet-scattering amplitude in the zeroth channel $\tilde{f}_0$. Its low-energy limit yields the time-averaged scattering length (5.60)

$$\tilde{a}_{\mathrm{scatt}}(\omega) = -\lim_{\epsilon \to 0} \tilde{f}_0(\epsilon, \omega) \tag{7.2}$$

and it determines the strength of elastic scattering (5.28) by the driven potential, as its absolute square is proportional to the cross section of the zeroth Floquet channel

$$\langle\langle \sigma_0 \rangle\rangle = 4\pi |\tilde{f}_0|^2. \tag{7.3}$$

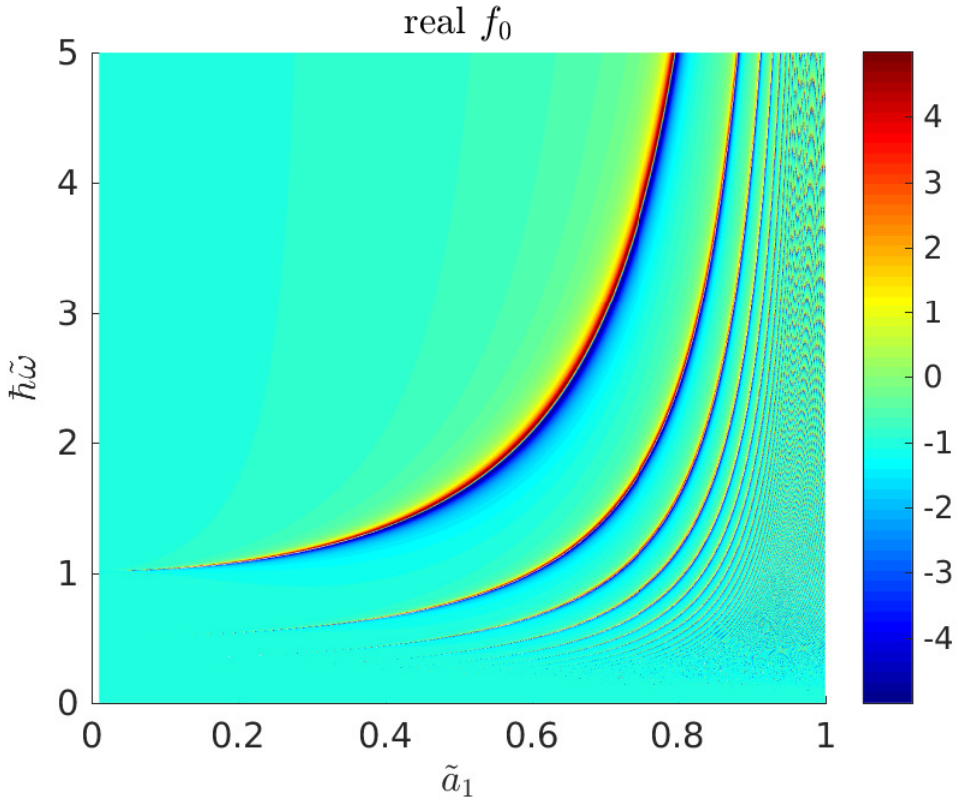

(a)

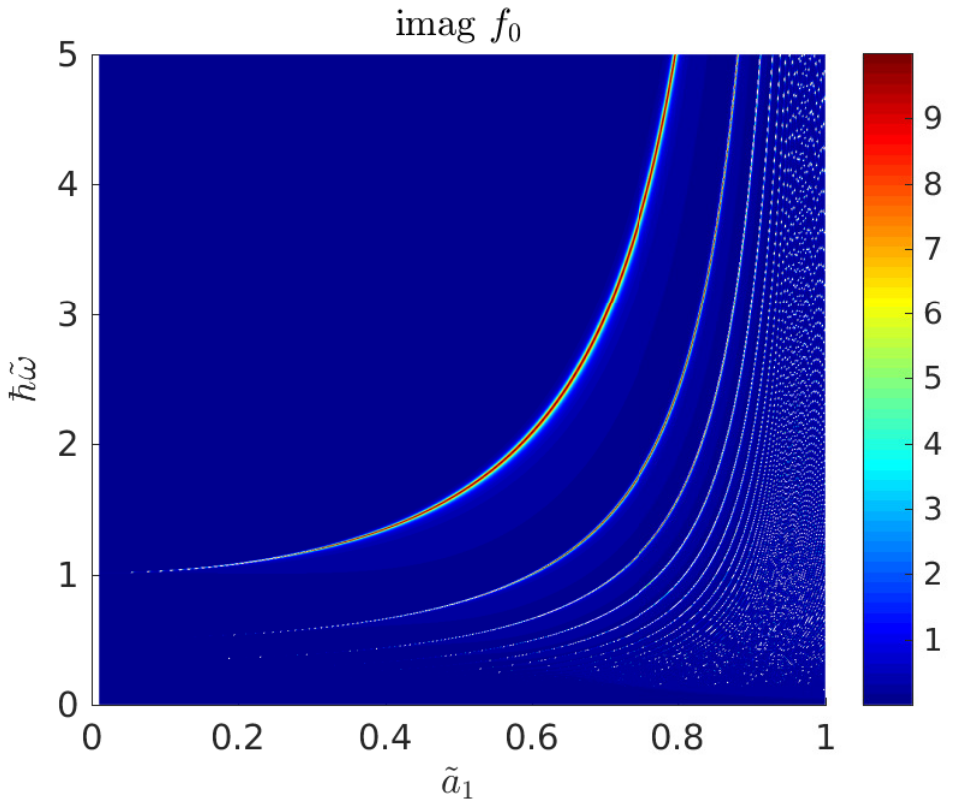

(b)

Figure 7.1.: Plot of the real **(a)** and imaginary **(b)** part of the time-averaged scattering amplitude in the $\tilde{\omega}$-$\tilde{a}_1$ plane for a Floquet energy of $\tilde{\epsilon} = 0.01$ and positive average scattering length $\bar{a}$.

Furthermore, its imaginary part can be related to the time-averaged total cross section by the Floquet optical theorem (5.66)

$$\langle\langle\sigma\rangle\rangle = \frac{4\pi}{k}\text{Im } \tilde{f}_0. \tag{7.4}$$

In order to measure time-averaged quantities in experiment, the time scale of the measuring process should be much larger than the period of the time-periodic driving.

We show in Appendix E that, if we consider the scattering of atoms in a Bose-Einstein condensate by a periodically modulated interaction potential, the Floquet scattering length $\tilde{a}_{\text{scatt}}(\omega)$ appears in the interaction term of the Gross-Pitaevskii equation in Floquet-Born approximation. Therefore (7.2) is directly related to the interaction strength of particles in a Bose-Einstein condensate and a tuning of the Floquet-scattering length leads to a change of the interaction strength.

In Figure 7.1 real and imaginary part of the scattering amplitude $\tilde{f}_0$ is plotted in the $\tilde{\omega}$-$\tilde{a}_1$ plane with a Floquet energy of $\tilde{\epsilon} = 0.01$ and positive average scattering length $\bar{a}$. We see lines of resonances, where the imaginary part obtains its maximum and the real part is enhanced. As the imaginary part corresponds via (7.4) to the total scattering cross section, the particle is scattered maximally along these lines. We therefore call these lines scattering resonances. As they do not cross each other, we enumerate them in Figure 7.1 from left to right. As the width of these resonances vanishes in the limit of small $\tilde{a}_1$, it cannot be seen in Figure 7.1, that some lines reach the $\tilde{\omega}$-axis. With growing $\tilde{a}_1$ their slope and their width increases. For $\tilde{a}_1$ close to one the lines of resonance seem to get too dense to get numerically resolved.

In order to understand these resonances better, Figure 7.2 shows a cut along the $\tilde{\omega}$-axis at $\tilde{a}_1 = 0.1$ for the first resonance with several Floquet energies $\tilde{\epsilon}$. As it converges to the scattering length $\tilde{a}_{\text{scatt}}$ for vanishing energy, we investigate the negative scattering amplitude $-\tilde{f}_0$. The case of a Floquet energy of $\tilde{\epsilon} = 10^{-3}$ is shown in **(a)**. Here the enhancement of the scattering amplitude is small compared to the other Panels. In **(b)** we reduced the Floquet energy by a factor of 10^{-1}. Here, the real part of the scattering amplitude has a larger maximum as in Panel **(a)**, while the qualitative course is the same. The minimum of the imaginary part also decreases, which is signalling a larger total cross section. This trend continues for lower Floquet energy in Panel **(c)**. Panel **(d)** shows the case of vanishing Floquet energy, where the negative scattering amplitude $-\tilde{f}_0$ equals the scattering length $\tilde{a}_{\text{scatt}}$. In this case the width of the imaginary part converges to zero, while the real part is still enhanced and can be tuned to any value between plus and minus infinity. This allows the enhancement of the scattering strength to any desired value by tuning the driving frequency. The vanishing imaginary part signals with equation (5.68) the absence of inelastic scattering in the vicinity of a scattering resonance.

In Figure 7.3 we plot the negative scattering amplitude $-\tilde{f}_0$ for different driving strengths $\tilde{a}_1$, while we centre each plot at the resonance frequency $\tilde{\omega}_0$, where the imaginary part is maximally enhanced. We observe, that the shape of the resonances is the same, if we rescale the difference between driving frequency $\tilde{\omega}$ and the frequency $\tilde{\omega}_0$, as we did in Figure 7.3. This shows, that the width of the resonance can be tuned by the driving strength $\tilde{a}_1$. Since solely $\tilde{a}_1$ is changed in Figure 7.3, the transformation between the Panels is not described by the scale invariance (6.27). The similarity rather portends that the scattering resonances have an universal behaviour [3]. In Section 7.5 we

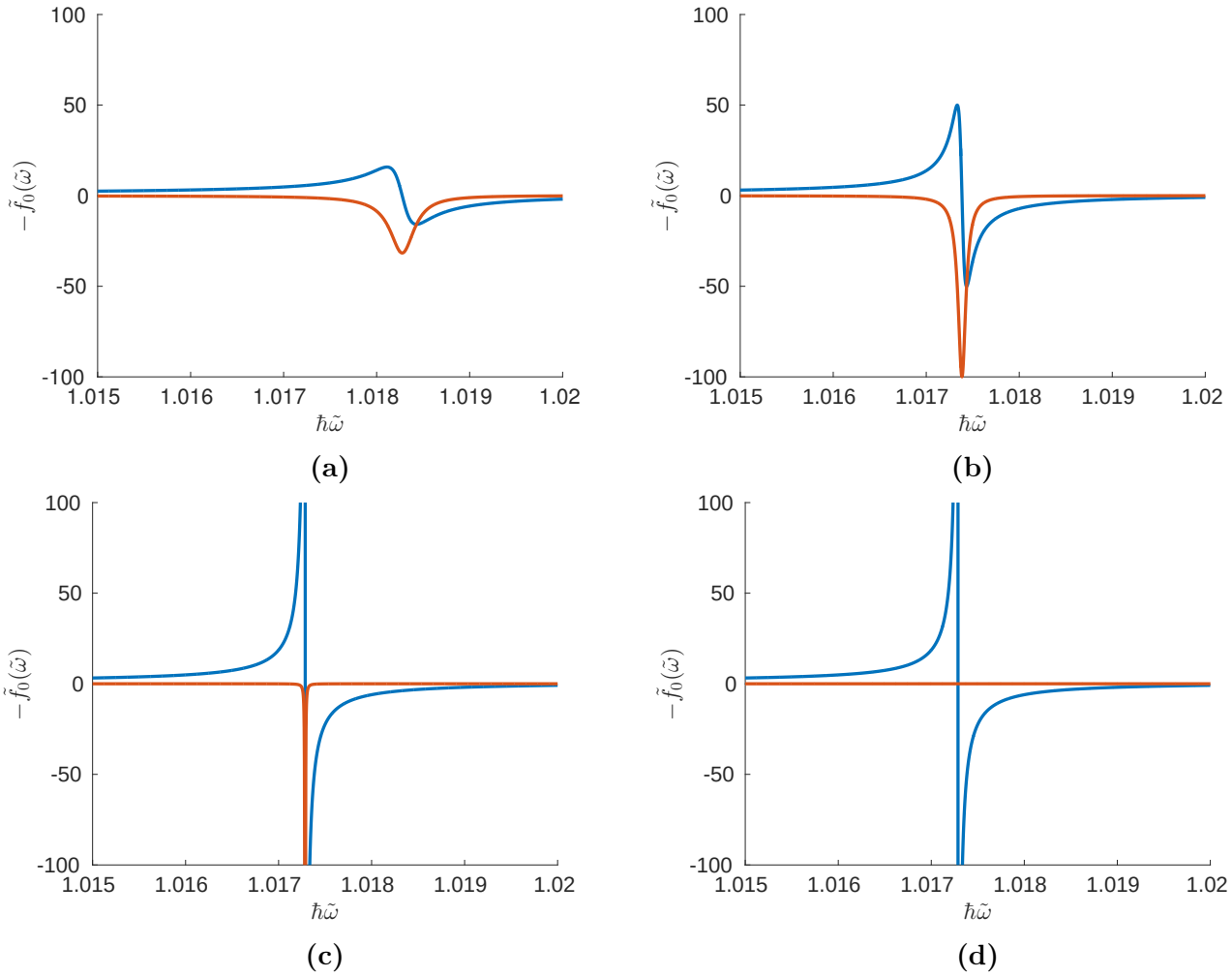

Figure 7.2.: Plot of real (blue) and imaginary (red) part of the negative scattering amplitude over the driving frequency for $\tilde{a}_1 = 0.1$ and $\tilde{\epsilon} = 10^{-3}$ **(a)**, $\tilde{\epsilon} = 10^{-4}$ **(b)**, $\tilde{\epsilon} = 10^{-8}$ **(c)** and $\tilde{\epsilon} = 0$ **(d)**.

do a more detailed analysis of the resonance shape and see that it can be approximately described by simple formulas, where only fitting parameters of these formulas change with $\tilde{a}_1$, but not its qualitative shape.

The case of scattering by a contact potential having a negative average scattering length $\bar{a}$ is shown in Figure 7.4. Both real and imaginary part of the scattering amplitude change by tuning of the driving frequency $\tilde{\omega}$ and driving strength $\tilde{a}_1$, but there are no lines of resonances, where scattering is strongly enhanced. We will see in Section 7.2 that the occurrence of the scattering resonances is related to the presence of a bound state. For negative time-averaged scattering length $\bar{a}$ the potential is attractive and it turns out, that such a bound state and therefore scattering resonances are not present. If not explicitly stated, we therefore investigate in the following the case of positive $\bar{a}$.

In Figure 7.5 the cut-off index $m_{\mathrm{cut-off}}$, at which equation (6.43) is truncated, is shown. It increases for larger $\tilde{a}_1$ and is expected to diverge in the limit of $\tilde{a}_1 \to 1$. This indicates, that our

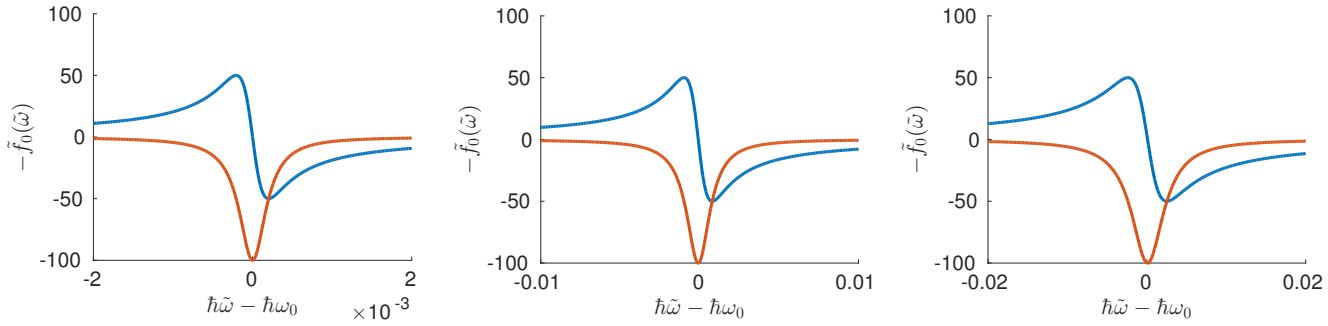

(a) **(b)** **(c)**

Figure 7.3.: Plot of the negative scattering amplitude $-\tilde{f}_0$ with Floquet energy $\tilde{\epsilon} = 10^{-4}$. Panel **(a)** shows the case of $\tilde{a}_1 = 0.2$, where $\hbar\tilde{\omega}_0 = 1.072$, while **(b)** shows the case of $\tilde{a}_1 = 0.4$ with $\hbar\tilde{\omega}_0 = 1.34$ and **(c)** shows the case of $\tilde{a}_1 = 0.6$, where $\hbar\tilde{\omega}_0 = 2.084$.

numerical method breaks down at $\tilde{a}_1 = 1$. In addition, our method fails for $\tilde{a}_1 > 1$, as the results depend on the cut-off index $m_{\mathrm{cut-off}}$ in this case and thus are not reliable.

7.2. Feshbach-Fano Physics in Floquet Picture

In this Section we connect the occurrence of scattering resonances to the energy of so-called driving-induced bound states and find, that the emergence of a scattering resonance can be explained by a Fano-Feshbach resonance involving these bound states.

We define a scattering resonance as a state with maximally enhanced scattering cross section for a given Floquet energy $\tilde{\epsilon}$. Our goal is to use this definition in order to calculate the value of the scattering amplitudes f_0 at a resonance and to derive a recursion relation with a boundary condition, which is only fulfilled at a resonance and can therefore be used to calculate the position of those.

We start our derivation by the Floquet-optical theorem (5.66) and specialise it to the case of s-wave scattering (5.67)

$$\mathrm{Im}\ f_0 = k[(\mathrm{Re}\ f_0)^2 + (\mathrm{Im}\ f_0)^2] + \sum_{\substack{n \geq n_c \\ n \neq 0}}^{\infty} |f_n|^2 k_n. \tag{7.5}$$

This equation is quadratic in Im f_0 and can therefore be solved for it

$$\mathrm{Im}\ f_0 = \frac{1 \pm \sqrt{1 - 4k[k(\mathrm{Re}\ f_0)^2 + \sum_{n\neq 0} |f_n|^2 k_n]}}{2k}. \tag{7.6}$$

Due to the Floquet optical theorem (5.66) scattering is maximal, if this also applies to Im $\tilde{f}_0$. As the quantities k, $(\mathrm{Re}\ f_0)^2$, $|f_n|^2$ and k_n behind the minus sign of the discriminant in equation (7.6)

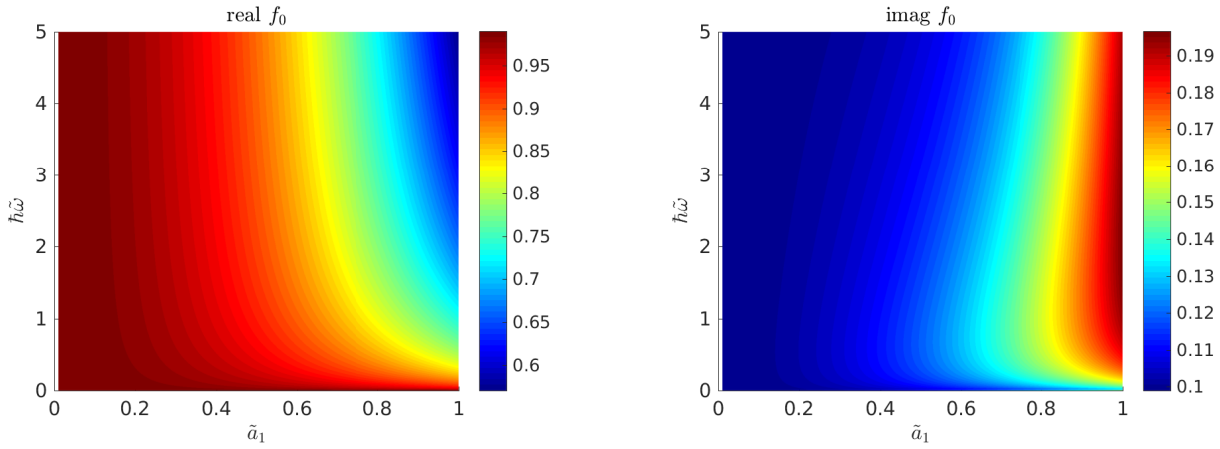

(a) **(b)**

Figure 7.4.: Plot of real **(a)** and imaginary **(b)** part of the scattering amplitude in zeroth Fourier mode in the $\tilde{\omega}$-$\tilde{a}_1$ plane for a Floquet energy $\tilde{\epsilon} = 0.01$ and negative average scattering length $\bar{a}$.

are greater or equal than zero, they all have to vanish in order to maximise Im f_0 and therefore the cross section $\langle\langle\sigma\rangle\rangle$. This implies that at resonance the scattering amplitude in zeroth Floquet channel equals

$$f_0^{\text{res}} = \frac{i}{k}, \tag{7.7}$$

while the ones in all other open Floquet channels vanish

$$f_n^{\text{res}} = 0 \ \forall n \geq n_c \text{ and } n \neq 0. \tag{7.8}$$

We introduced the superscript res in order to emphasise, that these values are obtained at a scattering resonance. Note, that condition (7.7) is fulfilled by the resonances shown in Figure 7.2 and the sketch of the wave function at resonance displayed in Figure 7.6. In comparison to Figure 6.1 all amplitudes of wave functions in higher Floquet channels vanish in Figure 7.6 because of relation (7.8). Inserting equation (6.26) into (7.7) we arrive at the following condition for the Hankel-function coefficient

$$D_0^{\text{res}} = -\frac{1}{2}, \tag{7.9}$$

while the coefficients belonging to open channels vanish

$$D_n^{\text{res}} = 0 \ \forall n \geq n_c \text{ and } n \neq 0, \tag{7.10}$$

as they are proportional to the corresponding scattering amplitude. The next step is to adapt recursion relation (6.37) to coefficients D_n^{res} with a negative index n. Inserting condition (7.9) into (6.37) for $n = -1$ leads to

$$\left(\frac{i}{\tilde{k}_{-1}} - 1\right) D_{-1}^{\text{res}} - \frac{\tilde{a}_1}{2} D_{-2}^{\text{res}} + \frac{\tilde{a}_1}{4} = \frac{\tilde{a}_1}{4}, \tag{7.11}$$

while we obtain for all indices $n \leq -2$ the equation

$$\left(\frac{i}{\tilde{k}_n} - 1\right) D_n^{\text{res}} - \frac{\tilde{a}_1}{2}\left(D_{n-1}^{\text{res}} + D_{n+1}^{\text{res}}\right) = 0, \ \forall n \leq -2. \tag{7.12}$$

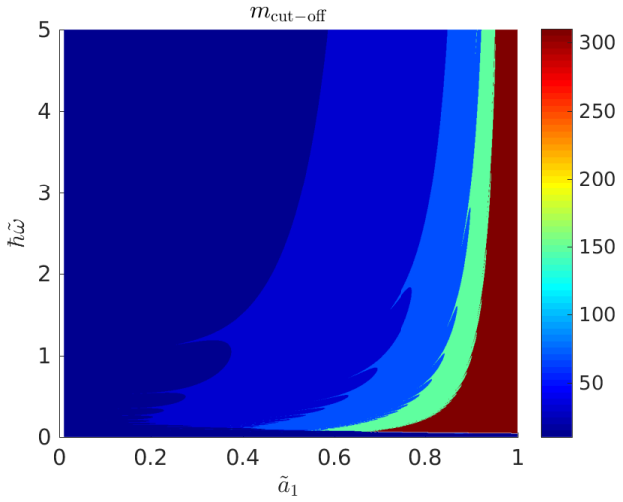

Figure 7.5.: Maximal cut-off index $m_{\mathrm{cut-off}}$ needed to ensure the convergence of the truncation method. As the cut-off index is expected to diverge for $\tilde{a}_1 \to 1$, we limited this index to be smaller than a maximal one of around 300.

Since at resonance the Floquet state should also be normalisable, the coefficients D_n^{res} have to fulfil the boundary condition (6.25). As equation (6.25) is implicitly fulfilled for $n \to \infty$ by condition (7.10), a physical solution of (7.11) and (7.12) has to satisfy

$$\lim_{n\to-\infty} D_n^{\mathrm{res}} = 0. \tag{7.13}$$

Condition (7.13) is used in Section 7.3 in order to calculate the energies $\tilde{\epsilon}_{\mathrm{res}}$, where a resonance occurs in the $\tilde{\omega}$-$\tilde{a}_1$ plane.

Now we want to make the connection from the emergence of scattering resonances to the occurrence of driving induced bound states. This consideration starts by noting, that if the term $\tilde{a}_1/4$ in equation (7.14) is cancelled, equations (7.11) and (7.12) can be rewritten in the from

$$\left(\frac{i}{\tilde{k}_n} - 1\right) D_n^{\mathrm{side}} - \frac{\tilde{a}_1}{2}\left(D_{n-1}^{\mathrm{side}} + D_{n+1}^{\mathrm{side}}\right) = 0, \ \forall n \leq -1, \tag{7.14}$$

if we impose to (7.14) as boundary conditions (7.13) and

$$D_0^{\mathrm{side}} = 0, \tag{7.15}$$

while relabelling $D_n^{\mathrm{res}} = D_n^{\mathrm{side}}$ for $n \leq -1$. This decouples the recursion for coefficients D_n^{side} belonging to negative indices n from the one for positive ones. We introduced the label side in order to point out, that equation (7.14) can be alternatively derived from radial Floquet equation (6.11), if a wave function of the form

$$R_n(r) = \begin{cases} 0, & n \geq 0 \\ -D_n^{\mathrm{side}} \frac{e^{-\kappa_n r}}{\kappa_n r}, & n < 0 \end{cases}, \tag{7.16}$$

being non-zero only in the side system, which is defined to consist of all closed Floquet channels, is taken as ansatz. In this step we additionally assume all Floquet channels with $n < 0$ to be closed.

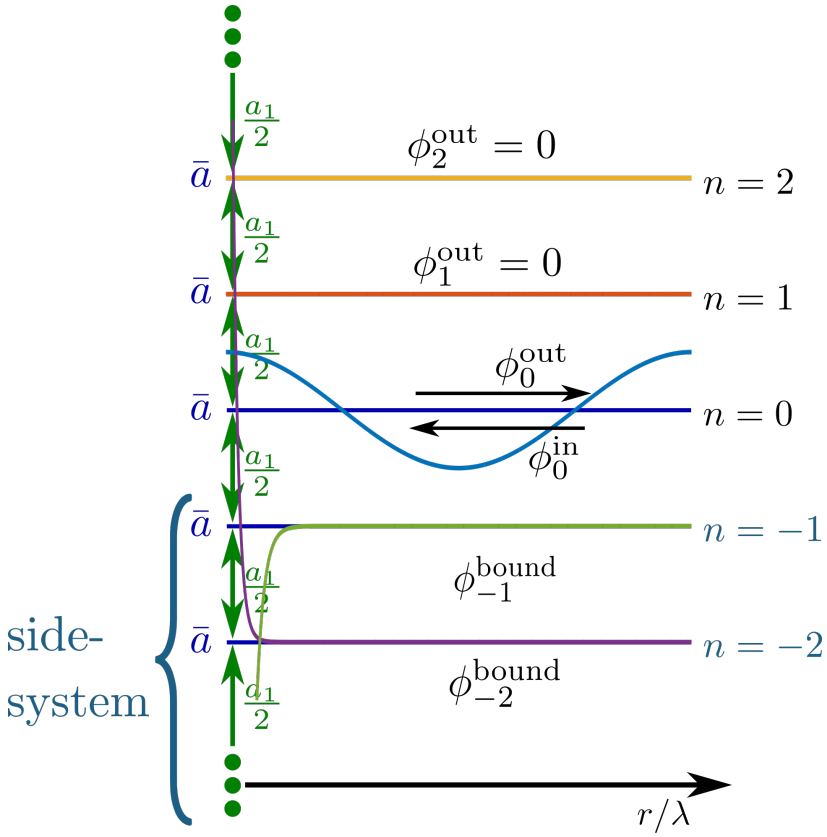

Figure 7.6.: Plot of the actual wave function at a scattering resonance with a critical index $n_c = 0$. In all channels with $n \geq 1$ the wave functions ϕ_n^{out} vanish, while for $n = 0$ it has the form such that scattering gets maximally enhanced. For Floquet channels with $n \leq -1$ exponentially decaying solutions exist. This set of bound states is named side system. This plot is made for $\tilde{\epsilon} = 10^{-2}$, $\tilde{a}_1 = 0.1$ and $\hbar\tilde{\omega} = 1.0271837$.

Due to this, ansatz (6.11) consists only of bound wave functions and is therefore referred to a bound state, which is induced by periodic driving and therefore named as driving-induced bound state. It has the dispersion

$$\tilde{\epsilon}_{\text{side}} + n\hbar\tilde{\omega} = -\frac{\hbar^2}{2m}\tilde{\kappa}_n^2, \tag{7.17}$$

i.e. $\tilde{k}_n = i\tilde{\kappa}_n$.

The fact, that equation (7.14) can be derived in two different ways gives rise to a central statement of this thesis: A scattering resonance emerges at points in the $\tilde{\omega} - \tilde{a}_1$ plane, where the energy of an incoming particle $\tilde{\epsilon}_{\text{res}}$ equals the energy of a bound state $\tilde{\epsilon}_{\text{side}}$ located in the side system

$$\tilde{\epsilon}_{\text{res}} = \tilde{\epsilon}_{\text{side}} \tag{7.18}$$

and the side system gets decoupled from the open Floquet channels. In the case of a non-vanishing wave function in the zeroth Floquet channel, this decoupling is manifested due to the above reasoning

and equation (7.9) by a wave function of

$$R_0(r) = \frac{i}{kr}\cos(kr). \tag{7.19}$$

At a scattering resonance the wave function in the zeroth Floquet channel is as shown in Figure 7.6 exactly given by (7.19), while it vanishes due to equation (7.10) for all further open channels and is given by (7.16) for the channel located in the side system.

There are ranges of the parameters $\tilde{\omega}$ and $\tilde{a}_1$, where the energy $\tilde{\epsilon}_{\text{side}}$ lies above zero and thus in the continuum of scattering solutions. In this case, Floquet states of the form (7.16) are bound states in the continuum. In general, bound states in the continuum are defined as square-integrable bound states which are energetically embedded in a continuum of non-normalizable scattering states [91]. This idea goes back to von Neumann and Wigner [92], who theoretically constructed a time-independent potential possessing such a bound state [93]. They also appear in interfering resonances [94, 95] and can be induced by periodically driven systems [96, 97]. It has been shown that they occur in one-dimensional driven impurities and are connected to transmission resonances in both tight-binding lattice and driven delta potential [5, 49].

With the insight, that in the presence of a scattering resonance, the side system possesses a bound state in the continuum, the emergence of such a resonance can be explained in an intuitive way by destructive interference of different paths for the scattered wave related to Fano-interference [50, 51, 90, 98]. The first path consists of an elastic scattering process by the contact potential in the zeroth Floquet channel, while the second involves a transition to and from the side system before getting scattered. At resonance condition, the side system possesses a bound state in the continuum and the second path thus obtains an additional phase shift of π. The destructive interference of both paths is leading to a decoupling of side system and open channels, and therefore to (7.19) as a wave function in the zeroth Floquet channel and due to (7.7) to a maximal scattering amplitude. Note, that similar features show up in the scattering of electrons with protons in a laser field [6, 10].

Equation (7.18) suggests that this resonance has similarities to static Feshbach resonances, which are discussed in Chapter 3. There also scattering becomes maximal, if the energy of the incoming particle equals up to a shift of (3.8) to the energy of a bound state in a closed channel. The energy of this bound state can be altered in the case of the common magnetic Feshbach resonance by tuning a magnetic field. For our driven scattering problem these tuning parameters are the driving frequency $\tilde{\omega}$ and the driving strength $\tilde{a}_1$, and the bound state is the bound state in the continuum located in the side system.

At last we take a look on the case $n = 0$ of equation (6.37) at a scattering resonance. If (7.9) and (7.10) is inserted, we obtain

$$D_{-1}^{\text{res}} = -\frac{2i}{\tilde{a}_1\tilde{k}}. \tag{7.20}$$

This result allows us to iteratively calculate in combination with the recursion relation (7.14) all coefficients D_n^{res} for negative n, if the value of $\tilde{k}$ is determined by the use of the convergence condition (7.13). Moreover we use it in order to derive a critical frequency $\tilde{\omega}_{\text{c}}$, below which no scattering

resonances occur. This is done by arguing, that the $n = -1$ Floquet channel is open if $\tilde{\epsilon} \geq \hbar\tilde{\omega}$, due to dispersion relation (5.17). In this case condition (7.10) also applies to the $n = -1$ channel and it states that $D_{-1}^{\mathrm{res}} = 0$, which is a contradiction to (7.20), as both $\tilde{a}_1$ and $\tilde{k}$ are not considered to be infinitely large, so that equation (7.20) could not become zero. Due to this reasoning scattering resonances can only occur for frequencies larger than the critical frequency $\tilde{\omega}_{\mathrm{c}}$ of Floquet energy divided by $\hbar$

$$\tilde{\omega} \geq \tilde{\omega}_{\mathrm{c}} = \frac{\tilde{\epsilon}}{\hbar}. \tag{7.21}$$

This feature has also been observed in scattering by an one-dimensional driven impurity [5, 98, 99] and is related to the opening of the Floquet channel with number $n = -1$. If condition (7.21) is not fulfilled, the side system does not include the Floquet channel with number $n = -1$ and is therefore not directly coupled to the zeroth Floquet channel, where the incoming wave is present. In this situation the side system can not be decoupled from the open Floquet channels. As it turned out that this decoupling of open and closed channels is essential for the emergence of a scattering resonance, this explains the absence of resonances for frequencies below the critical one (7.21).

7.3. Investigation of Resonance Positions

We now use equation (7.14) to calculate the locations $\tilde{\epsilon}_{\mathrm{res}}$ or $\tilde{\epsilon}_{\mathrm{side}}$, respectively, of the scattering resonances in the $\tilde{\omega}$-$\tilde{a}_1$ plane. In Subsection 7.3.1 we do the calculation with a numerical method, while in 7.3.2 we work out an analytic approximation in the limit of weak driving.

7.3.1. Numerical Calculation

In order to solve equation (7.14) numerically, we first map it to a set of linear equations of infinite size similar to (6.37), which reads

$$\underline{\underline{A}}\mathbf{D} = \mathbf{0}, \tag{7.22}$$

where the vector $\mathbf{D}$ consists of the coefficients D_n and the matrix elements of $\underline{\underline{A}}$ vanish except of

$$A_{n,n} = \frac{i}{\tilde{k}_n} - 1, \tag{7.23}$$

$$A_{n,n\pm1} = -\frac{\tilde{a}_1}{2}. \tag{7.24}$$

Like in equation (7.14) all indices n are restricted to the set $n \in -\mathbb{N}$. In contrast to (6.43) this equation is homogeneous. In this case a non-zero, and therefore physical, solution of the set of linear equations is only occurring, if the determinant of the matrix $\underline{\underline{A}}$ vanishes. In order to compute such a determinant numerically, we truncate the infinitely large matrix to a finite one by restricting the index to be larger than a cut off $m \in -\mathbb{N}$. This is appoximately valid due to condition (7.13). We use a Matlab algorithm to locate the zeros of the determinant and therefore the resonance positions.

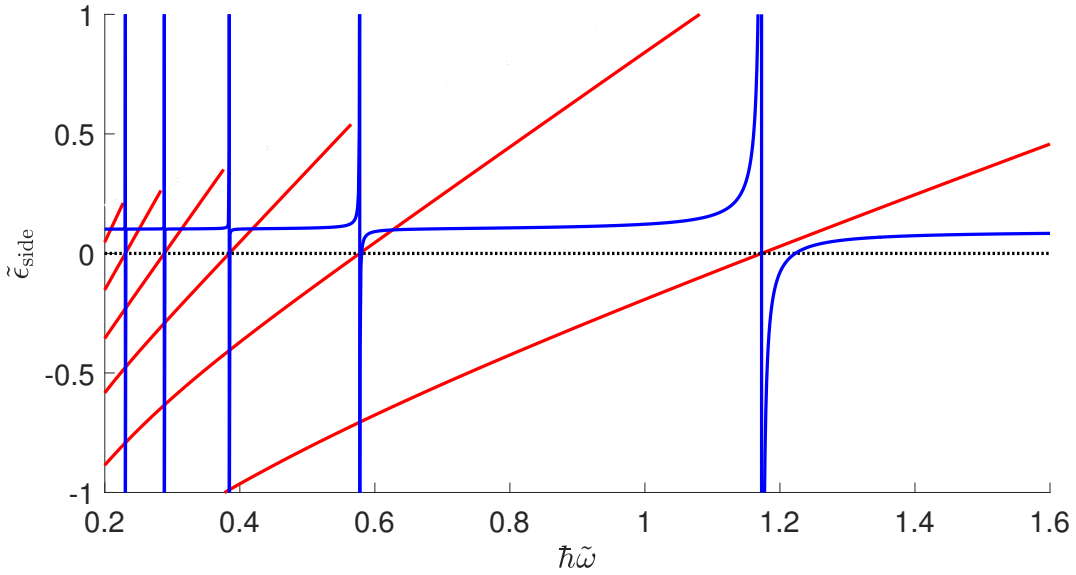

Figure 7.7.: Plot of the energy of the bound state of the side system $\tilde{\epsilon}_{\text{side}}$ (red) and the Floquet scattering amplitude $\tilde{a}_{\text{scatt}}$ (blue, in arbitrary units) over the driving frequency for $\tilde{a}_1 = 0.3$. The intersection of $\tilde{\epsilon}_{\text{side}}$ with the dotted line at $\tilde{\epsilon} = 0$ equals the position of the scattering resonances for $\tilde{a}_{\text{scatt}}$. We only calculated $\tilde{\epsilon}_{\text{side}}$ in the case of $\hbar\tilde{\omega} > \tilde{\epsilon}_{\text{side}}$, as otherwise no resonances occur.

For energies larger than the driving frequency the imaginary part of the determinant gets non-zero. This indicates, that in this case the wave vector k_{-1} gets real and therefore the side system begins at index $n = -2$. This results in the absence of scattering resonances in this region, as it represents the case of driving frequencies lower than the critical one (7.21).

In Figure 7.7 we plot the energy $\tilde{\epsilon}_{\text{side}}$ over the driving frequency for fixed $\tilde{a}_1$. This makes the statement of equation (7.18) directly visible: A scattering resonance, which is visualised by the divergence of $\tilde{a}_{\text{scatt}}$ painted in blue in Figure 7.7, emerges at driving frequencies, where the Floquet energy $\tilde{\epsilon} = 0$ equals the energy of the side system $\tilde{\epsilon}_{\text{side}}$. In addition it shows that for certain driving frequencies the side system possesses more than one bound state.

The results of this method in the $\tilde{\omega}$-$\tilde{a}_1$ plane is shown in Figure 7.8, where we show in **(a)** the lines, where $\tilde{\epsilon}_{\text{side}}$ intersect the Floquet energy of $\tilde{\epsilon} = 0$ and in **(b)** we show intersections with a Floquet energy of $\tilde{\epsilon} = 0.5$. We restricted this investigation to five scattering resonances located at the largest frequencies. In both Figures lines of scattering resonances exist, which all start in the case of $\tilde{\epsilon} = 0$ at the $\tilde{\omega}$-axis with the slope zero and ascend in the case of rising $\tilde{a}_1$. For $\tilde{\epsilon} = 0.5$ only three lines reach the $\tilde{\omega}$-axis, as the others would have reached it below the critical frequency $\tilde{\omega}_{\text{crit}}$. This behaviour of the lines of resonances equals to the lines of in Figure 7.1.

It turns out that in the case of negative $\bar{a}$ this method gives the result, that in the whole $\tilde{\omega}$-$\tilde{a}_1$ plane no bound state exists, and due to relation (7.18) this explains that no scattering resonances occur.

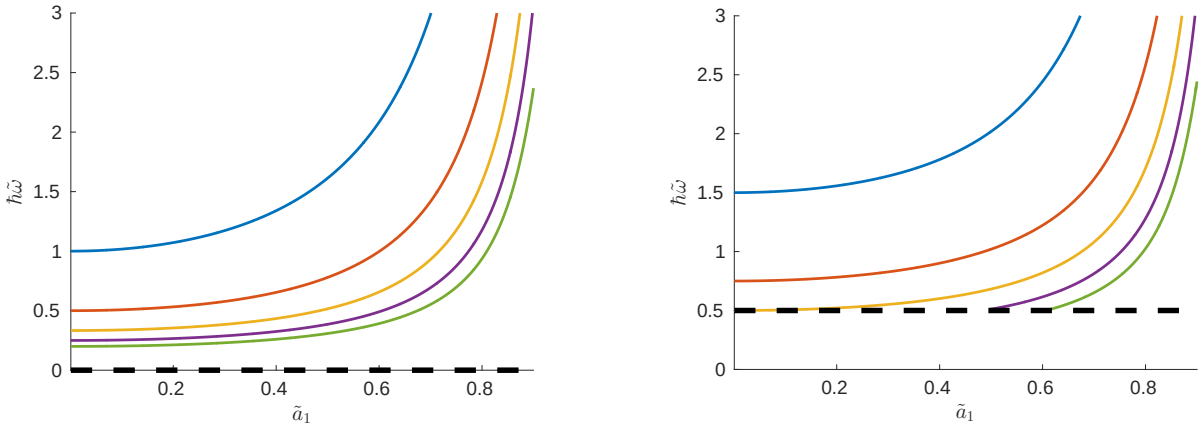

Figure 7.8.: Location of scattering resonances in the $\tilde{\omega}$-$\tilde{a}_1$ plane for $\epsilon = 0$ **(a)** and $\epsilon = 0.5$ **(b)**. The first resonance is painted in blue, the second red, the third yellow, the fourth purple and the fifth green. The dashed black vertical line shows the position of the critical frequency (7.21), below which no resonances occur.

7.3.2. Analytic Evaluation

This Subsection is devoted to an approximative analytic evaluation of the resonance position by expanding the recursion (7.14) in orders of the driving strength $\tilde{a}_1$. We therefore express (7.14) in the form

$$G_n D_n - \frac{\tilde{a}_1}{2}(D_{n+1} + D_{n-1}) = 0, \ n \in -\mathbb{N}, \tag{7.25}$$

where $G_n = 1/\tilde{\kappa}_n - 1$ and the subscript side is dropped at the coefficients D_n for simplicity. In order to evaluate this equation systematically we perform a perturbative ansatz for the coefficients

$$D_n = \sum_{\alpha=0}^{\infty} \tilde{a}_1^{\alpha} D_n^{(\alpha)}. \tag{7.26}$$

We first consider the limit of vanishing driving amplitude $\tilde{a}_1$, whose asymptotic behaviour is determined in zeroth order of $\tilde{a}_1$. The recursion (7.25) decouples in this case and reads

$$\left(\frac{1}{\tilde{\kappa}_n} - 1\right) D_n^{(0)} = 0. \tag{7.27}$$

It has only a non-vanishing solution

$$D_n^{(0)} = \delta_{n,m}, \ m \in -\mathbb{N}, \tag{7.28}$$

if the term in the brackets vanishes. This is the case if $\tilde{\kappa}_n = 1$ for some $n \in -\mathbb{N}$, which can be simplified to

$$\tilde{\epsilon}_{\mathrm{res}} = -1 - n\hbar\tilde{\omega}_{\mathrm{res}}, \ n = -1, -2, ..., -n_{\max}. \tag{7.29}$$

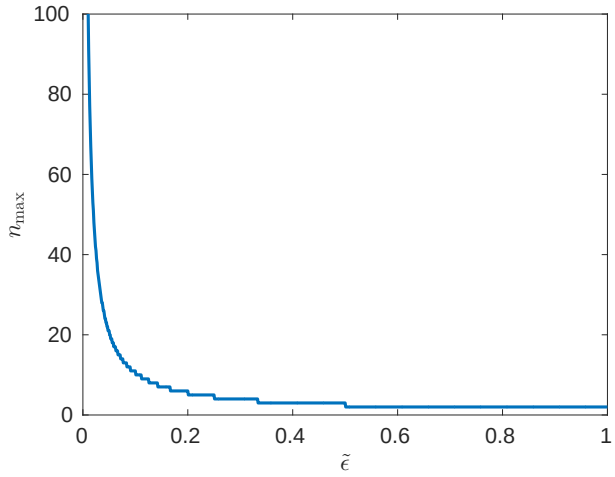

Figure 7.9.: Number of resonances $n_{\max}$ reaching the $\tilde{\omega}$ axis over the energy $\tilde{\epsilon}$. For vanishing energy the number diverges to infinity.

Due to the critical frequency (7.21) there exits a maximal number of scattering resonances for vanishing $\tilde{a}_1$, which can be calculated by inserting (7.29) into condition (7.21). This inequality can be solved for n, yielding

$$|n| \leq n_{\max}, \tag{7.30}$$

with $n_{\max} = \lfloor 1 + 1/\tilde{\epsilon} \rfloor$ as the maximal number of resonances at vanishing $\tilde{a}_1$. The quantity $n_{\max}$ is plotted in Figure 7.9. For $\tilde{\epsilon}$ close to one, only one resonance exists, while this number goes to infinity in the case of vanishing Floquet energy. For the case of $\tilde{\epsilon} = 0.5$ three resonances reach the $\tilde{\omega}$-axis, as it is shown in Figure 7.8.

Equation (7.29) provides an intuitive interpretation of the bound states of the side system, which stands on the right-hand side of this equation, as a field dressed version of the bound state of the static contact potential. Additionally a physical interpretation of the interfering paths, which create the scattering resonance by a Fano-interference, becomes clearer. The first path is the direct scattering process on the contact interaction, while the second one involves a transition to the bound state of the contact potential with an emission of $|n|$ driving field quanta and a subsequent transition back. Moreover, the resonance number, defined in Section 7.1, is given by $|n|$.

We now solve recursion (7.25) to the first order of $\tilde{a}_1$. The perturbative approach leads to the insight, that for a solution of the form (7.28) in zeroth order only the coefficients $D^{(1)}_{m\pm1}$ are unequal from zero. In case of the first resonance, where $n = -1$, equation (7.25) reads in this order of $\tilde{a}_1$

$$\begin{pmatrix} G_{-1} & -\tilde{a}_1/2 \\ -\tilde{a}_1/2 & G_{-2} \end{pmatrix} \begin{pmatrix} D^{(0)}_{-1} + \tilde{a}_1 D^{(1)}_{-1} \\ \tilde{a}_1 D^{(1)}_{-2} \end{pmatrix} = \begin{pmatrix} 0 \\ 0 \end{pmatrix}. \tag{7.31}$$

This equation only possesses a non-vanishing solution, if the determinant of the matrix vanishes. This leads to

$$G_{-1} G_{-2} = \frac{\tilde{a}_1^2}{4}. \tag{7.32}$$

In order to solve this equation approximately, we solve it first for $\tilde{\kappa}_{-1}$ and find

$$\tilde{\kappa}_{-1} = \frac{1}{1 + \frac{\tilde{a}_1^2}{4} \frac{1}{\frac{1}{\tilde{\kappa}_{-2}} - 1}}. \tag{7.33}$$

This expression can be solved for the driving frequency. In this step we approximate $\kappa_{-2} \approx \sqrt{\tilde{\epsilon}_{\mathrm{res}} + 2}$ by assuming the driving frequency to be located near the first resonance by inserting equation (7.29) into $\tilde{\kappa}_{-2}$. As an intermediate step we arrive at an expression for the driving frequency of the first scattering resonance for small $\tilde{a}_1$. This reads

$$\hbar\tilde{\omega}_{\mathrm{res}} \approx \tilde{\epsilon}_{\mathrm{res}} + \frac{1}{\left(1 + \frac{\tilde{a}_1^2}{4} \frac{1}{\frac{1}{\sqrt{\tilde{\epsilon}_{\mathrm{res}}+2}} - 1}\right)^2}. \tag{7.34}$$

Using the small-argument approximation $1/(1+x)^2 \approx 1 - 2x$ we extract the term in the leading order of $\tilde{a}_1$

$$\hbar\tilde{\omega}_{\mathrm{res}} \approx \tilde{\epsilon}_{\mathrm{res}} + 1 - \frac{1}{2} \frac{1}{\frac{1}{\sqrt{\tilde{\epsilon}_{\mathrm{res}}+2}} - 1} \tilde{a}_1^2. \tag{7.35}$$

This equation corresponds to (7.29) with an additional term being quadratic in $\tilde{a}_1$, which can be seen as a shift of the field dressed energy of the bound state due to a finite driving strength $\tilde{a}_1$. Alternatively, the same result can be obtained by looking at a convergence condition of the sequence similar to [49]. Following the procedure of [49], we come to

$$\frac{2}{\tilde{a}_1} G_{-1} \approx \frac{\tilde{a}_1}{2} G_{-2}^{-1}, \tag{7.36}$$

as an intermediate step, which is equal to equation (7.32).

In the case of resonances belonging to $n \neq -1$, a similar result can be obtained by looking at the determinant of the matrix

$$\begin{pmatrix} G_{n-1} & -\tilde{a}_1/2 & 0 \\ -\tilde{a}_1/2 & G_n & -\tilde{a}_1/2 \\ 0 & -\tilde{a}_1/2 & G_{n+1} \end{pmatrix}. \tag{7.37}$$

Performing the same steps as in the case of $n = -1$, we calculate the location on the $|n|$-th resonance

$$\hbar\tilde{\omega}_{\mathrm{res}} = \frac{\tilde{\epsilon}}{|n|} + \frac{1}{|n|} \frac{1}{\left[1 + \frac{\tilde{a}_1^2}{4} \left(\frac{1}{\frac{1}{\sqrt{\tilde{\epsilon}_{\mathrm{res}}(\frac{n+1}{n}-1)+\frac{n+1}{n}}} - 1} + \frac{1}{\frac{1}{\sqrt{\tilde{\epsilon}_{\mathrm{res}}(\frac{n-1}{n}-1)+\frac{n-1}{n}}} - 1} \right)\right]^2}, \tag{7.38}$$

which can be simplified in leading order of $\tilde{a}_1$ to

$$\hbar\tilde{\omega}_{\mathrm{res}} \approx \frac{\tilde{\epsilon}_{\mathrm{res}}}{|n|} + \frac{1}{|n|} - \frac{1}{2|n|} \left(\frac{1}{\frac{1}{\sqrt{\tilde{\epsilon}_{\mathrm{res}}(\frac{n+1}{n}-1)+\frac{n+1}{n}}} - 1} + \frac{1}{\frac{1}{\sqrt{\tilde{\epsilon}_{\mathrm{res}}(\frac{n-1}{n}-1)+\frac{n-1}{n}}} - 1} \right) \tilde{a}_1^2. \tag{7.39}$$

Similar to (7.35) these equations state that the energy of the driving induced bound state and therefore the resonant frequency can be changed by altering the driving strength $\tilde{a}_1$, while (7.39)

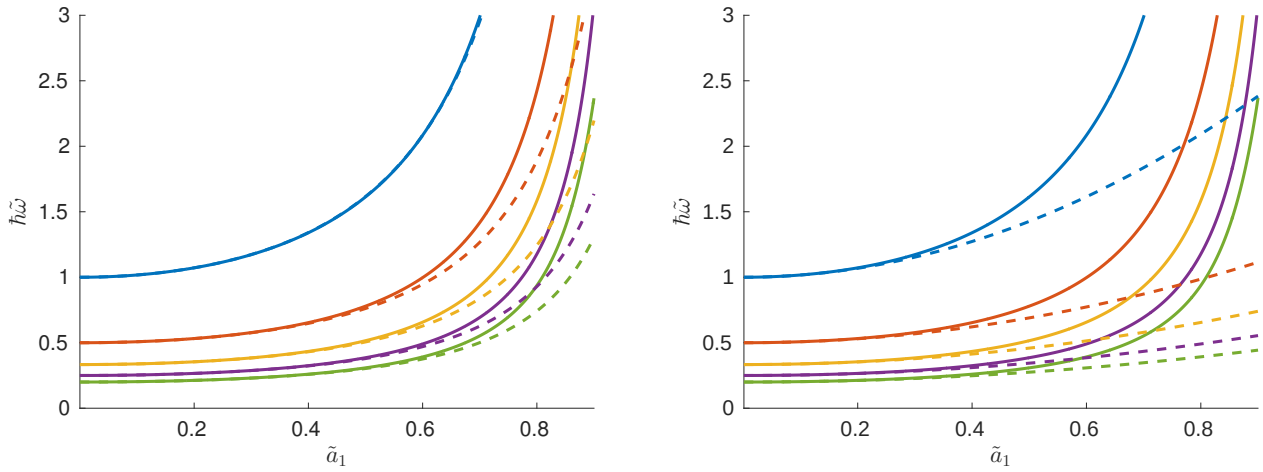

Figure 7.10.: Location of scattering resonances for $\tilde{\epsilon} = 0$ in the $\tilde{\omega}$-$\tilde{a}_1$ plane. The solid lines are obtained while using the numerics. In **(a)** we show in dashed lines the result of equation (7.38), while in **(b)** we display the result of (7.39) in dashed lines.

furthermore displays that this change is of the order $\tilde{a}_1^2$ for small driving strength $\tilde{a}_1$. Although there are technical differences in the derivation, equations (7.34) and (7.35) coincide with (7.38) and (7.39) in the case of $n = -1$. In Panel **(a)** of Figure 7.10 we compare equation (7.38) to the numerical data, while we do the same in Panel **(b)** with equation (7.39). For small $\tilde{a}_1$ both approximations fit well to the numerical results, but (7.38) agrees in a much larger range to the numerics as (7.39). Especially in the case of $n = -1$ the accordance of (7.38) to the numerics is exceptional.

In Figure 7.11 we plot the solution of recursion (7.25) at the first and second resonance. Although the coefficients D_{-1} of both cases are equal, the weight in case of the first resonance lies on D_{-1}, in case of the second the D_{-2} coefficient is largest. This demonstrates the validity of the perturbation approach (7.26) for small $\tilde{a}_1$.

At last, we shortly discuss the case of negative background scattering length $\bar{a}$. Due to equation (6.33) it holds in this case

$$\tilde{\kappa}_n = -\sqrt{-\tilde{\epsilon} - n\hbar\omega}\,. \tag{7.40}$$

In zeroth order, the perturbative approach (7.26) would only have a non-vanishing solution of the form $D_n^{(0)} = \delta_{n,m}$, if the condition

$$-\sqrt{-\tilde{\epsilon} - m\hbar\tilde{\omega}} = 1 \tag{7.41}$$

were fulfilled. As the square root is positive, the left-hand side of (7.41) becomes negative and can not be equal to 1. Therefore equation (7.41) is never fulfilled, which shows, at least in zeroth order of $\tilde{a}_1$, that no resonances can occur for negative $\bar{a}$. This can be also understood physically. As in the case of negative $\bar{a}$ the contact interaction is attractive, it possesses no bound state like for positive $\bar{a}$. There we have seen, that the scattering resonance originates from a Fano-interference of different paths, where one of these paths includes a direct scattering by the contact interaction and the other

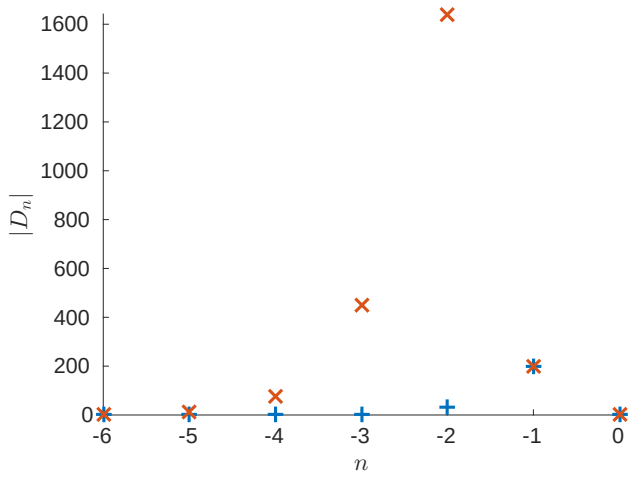

Figure 7.11.: Plot of the coefficients D_n^{res} at the first (blue) and second (red) resonance for $\tilde{a}_1 = 0.1$ and $\tilde{\epsilon} = 0.01$.

an additional transition to and from the bound state (A.14) of the contact potential. If the bound state is not present, the second path does not exist, with the result of no possible interference of paths. This leads to the absence of scattering resonances as shown in Figure 7.4.

7.4. Scattering Amplitude in the Vicinity of a Resonance

In the last two Sections we only discussed the situation, where we are located exactly at the resonance position. In this Section we want to broaden the view and investigate the scattering amplitude in the vicinity of a resonance. We already saw in Figures 7.2 and 7.4 that the shape of the scattering amplitude around a resonance looks similar for different Floquet energies $\tilde{\epsilon}$ and driving strengths $\tilde{a}_1$. This leads to the question, if this shape can be approximated by a simple formula, like it is done by (3.12) in the case of a magnetic Feshbach resonance. In order to give an answer to this question, we introduce two phenomenological formulas, for which we show by fitting them to the data, that they approximate the shape of the scattering amplitude in the vicinity of a resonance. In Subsection 7.4.1 we motivate the first formula as a frequency dependent adaption of equation (3.12) and compare it with the numerical data, while in Subsection 7.4.2 a second formula is derived by investigating scattering in a two-channel model. In Section 7.5 we use these formulas in order to extract position and width of the resonances by fitting the formulas introduced in this Section to the data.

7.4.1. Frequency Controlled Feshbach Scattering Amplitude

The first formula originates from equation (3.10). In the case of magnetic Feshbach resonances the bound-state energy E_R in equation (3.10) is parametrised by $E_R = \delta\mu(B - B_0)$. Inspired by this

approach we assume also a linear dependency of the bound state energy on the driving frequency

$$E_R = C\hbar(\tilde{\omega} - \tilde{\omega}_0), \tag{7.42}$$

where ω_0 denotes the resonant frequency and C is a constant. Inserting this into equation (3.10) yields

$$-\tilde{f}_0(\tilde{\omega}) = a_{\mathrm{bg}} \left(1 - \frac{\Delta}{\hbar\tilde{\omega} - \hbar\tilde{\omega}_0 - i\Gamma}\right). \tag{7.43}$$

We additionally extrapolate the scattering length to the negative scattering amplitude in the case of non-vanishing energy of the scattered particle. The involved parameters will be used as fitting parameters and have the following physical meaning. The background scattering length a_{bg} equals the scattering length in the limit of large frequencies, Δ equals the width of the real part of the resonance in the limit of vanishing Γ. The quantity Γ limits the maximal amount of scattering and determines the width of the imaginary part. We introduce the dimensionless variable

$$x = \hbar\frac{\tilde{\omega} - \tilde{\omega}_0}{\Delta} \tag{7.44}$$

and separate equation (7.43) in real and imaginary part

$$-\frac{\mathrm{Re}\ \tilde{f}_0(\tilde{\omega})}{a_{\mathrm{bg}}} = 1 + \frac{x}{x^2 + \left(\frac{\Gamma}{\Delta}\right)^2} \tag{7.45}$$

$$-\frac{\mathrm{Im}\ \tilde{f}_0(\tilde{\omega})}{a_{\mathrm{bg}}} = \frac{\Delta}{\Gamma}\frac{1}{\left(\frac{x}{\Gamma}\right)^2 + 1}. \tag{7.46}$$

In Figure 7.12 we compare these formulas to the numerical data by fitting both real and imaginary part simultaneously. In general, we obtain a good agreement between both, deviations are much smaller than the actual values.

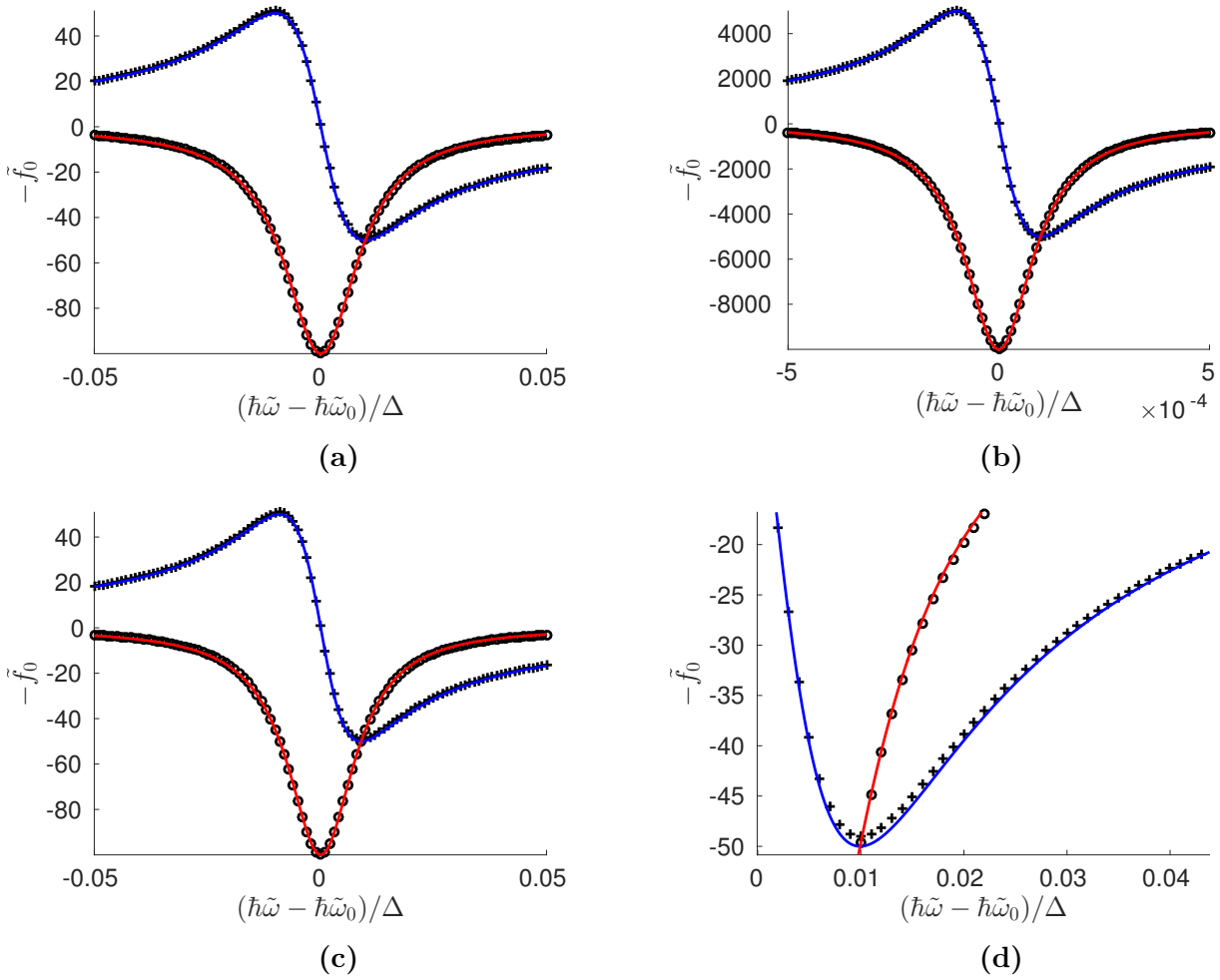

Figure 7.12.: Comparison of the real (blue) and imaginary (red) part of the scattering amplitude $-\tilde{f}_0$ over the difference of the driving frequency $\tilde{\omega}$ from the resonant $\tilde{\omega}_0$ measured in units of the width Δ. The values for fitting equation (7.43) are shown with + for real and o for imaginary part. Panel **(a)** shows the case of $\tilde{\epsilon} = 10^{-4}$ and $\tilde{a}_1 = 0.1$, which gave the result of $\hbar\tilde{\omega}_0 = 1.0174$, $\Delta = 5.0673 \times 10^{-3}$, $\Gamma = 5.0260\ 10^{-5}$ and $a_{\mathrm{bg}} = 0.9917$. Panel **(b)** shows the case of $\tilde{\epsilon} = 10^{-8}$ and $\tilde{a}_1 = 0.1$, which gave the result of $\hbar\tilde{\omega}_0 = 1.0173$, $\Delta = 5.064 \times\ 10^{-3}$, $\Gamma = 5.025 \times 10^{-7}$ and $a_{\mathrm{bg}} = 0.992$. Panel **(c)** shows the case of $\tilde{\epsilon} = 10^{-4}$ and $\tilde{a}_1 = 0.5$, which gave the result of $\hbar\tilde{\omega}_0 = 1.6135$, $\Delta = 0.1671$, $\Gamma = 1.5 \times 10^{-3}$ and $a_{\mathrm{bg}} = 0.9$. Panel **(d)** shows an enlarged plot of case **(a)** in order to indicate the limitations of the method.

In **(b)** we decreased the Floquet energy $\tilde{\epsilon}$ compared to **(a)**. While the width Δ stays approximately the same, the maximal enhancement of scattering is larger, while the scaling of the frequency axis by a factor of 10^{-2} has to be done in order to resolve the shape of the resonance in a way like it is done in **(b)**. This behaviour is implemented in equation (7.46), as Γ also changes with 10^{-2}, which leads with equation (7.46) to an enhancement of the maximum by 10^2. In addition, (7.46) is expressed in a way, where it only depends on x/Γ, which makes visible, that the scaling of the x-axis leads to a similar shape of the imaginary part of the scattering amplitude. The real part (7.45) has similar

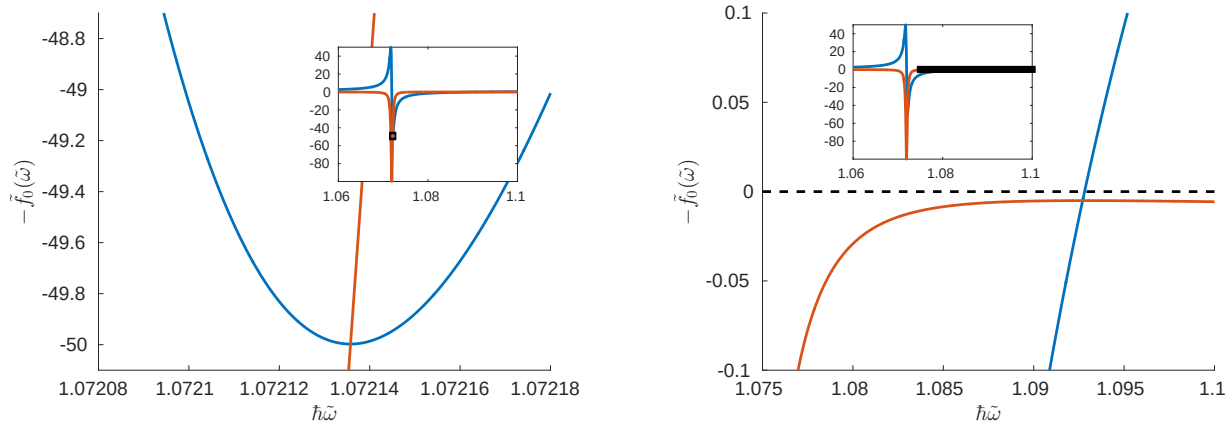

(a) **(b)**

Figure 7.13.: Enlarged plots of real (blue) and imaginary (red) part of the scattering amplitude calculated with the numerical method of Subsection 6.4.1. The black area in the inset points out the enlarged area. The black dotted line in panel **(b)** is a guide to the eye. Both plots are calculated with $\tilde{\epsilon} = 10^{-4}$ and $\tilde{a}_1 = 0.2$.

scaling properties. In **(c)** we increased $\tilde{a}_1$ compared to **(b)**, here the curve looks the same like in **(b)** and the value of Δ/Γ stays approximately the same. This behaviour is also included in equations (7.45) and (7.46), as (7.45) depends on Δ/Γ, while (7.46) has slight deviations. Panel **(d)** shows that equation (7.45) deviates largest from the data around the maximum value of the real part. In order to see this more detailed, we show in Figure 7.13 **(a)** an enlarged plot of the numerical data, which fulfil the relation

$$2 \max |\mathrm{Re}\ \tilde{f}_0| = \max |\mathrm{Im}\ \tilde{f}_0|, \tag{7.47}$$

but equation (7.43) does that explicitly not. This shows a limitation of the fitting with equation (7.43).

As it is useful in the later discussion, we calculate the limit of vanishing Γ of equations (7.45) and (7.46). The imaginary part (7.46) is proportional to a Lorentz-shaped curve with width Γ. Therefore in the limit $\Gamma \to 0$ it is proportional to the Dirac-delta function. Both real and imaginary part of the scattering amplitude read in the limit of vanishing Γ

$$-\lim_{\Gamma\to 0} \frac{\mathrm{Re}\ \tilde{f}_0}{a_{\mathrm{bg}}} = 1 - \frac{1}{x}, \tag{7.48}$$

$$-\lim_{\Gamma\to 0} \mathrm{Im}\ \frac{\tilde{f}_0}{a_{\mathrm{bg}}} = -\Delta\pi\delta(\hbar\tilde{\omega} - \hbar\tilde{\omega}_0) \tag{7.49}$$

Equation (7.48) equals (3.12), if the magnetic field is replaced by the driving frequency $\tilde{\omega}$. But instead of being zero, the imaginary part is proportional to the Dirac-Delta function in this limit.

7.4.2. Scattering Amplitude of a Simple Coupled Channel Model

In the spirit of the radial Floquet equation (6.11) the scattering by a time-dependent potential can be rewritten as a multi-channel scattering problem. For the derivation of the second approximative formula, we ask the question, how many channels are necessary in order to approximate the physics of Floquet scattering, which intrinsically involves an infinite amount of channels. As the simplest non-trivial model we investigate the scattering by a two-channel Hamiltonian with contact interaction

$$H(r) = H_0(r) + V_{\text{int}}(r). \tag{7.50}$$

Here H_0 consists of the kinetic energy and the intra-channel potential

$$H_0 = -\frac{\hbar^2}{2\mu}\begin{pmatrix} \frac{1}{r^2}\frac{\partial}{\partial r}r^2\frac{\partial}{\partial r} & 0 \\ 0 & \frac{1}{r^2}\frac{\partial}{\partial r}r^2\frac{\partial}{\partial r} \end{pmatrix} + \frac{\hbar^2}{2\mu}\begin{pmatrix} \frac{2a_0}{r^2}\delta(r)\frac{\partial}{\partial r}r & 0 \\ 0 & V + \frac{2a_1}{r^2}\frac{\partial}{\partial r}r \end{pmatrix}, \tag{7.51}$$

where the zeroth channel is considered to be open, while the energy of the first channel is shifted by V in order to obtain a closed one. If we only consider H_0 as the Hamiltonian, the two channels are decoupled, and the scattering by H_0 is described with the findings of Appendix A. In this case the scattering amplitude in the zeroth channel is $-f^{-1} = 1/a_0 + ik$ and the first one possesses a bound state with the eigenenergy

$$\mathcal{E}_{\text{bound}} = V - 1/a_1^2. \tag{7.52}$$

The inter-channel coupling is induced by the potential

$$V_{\text{int}}(r) = \frac{\hbar^2}{2\mu}\begin{pmatrix} 0 & \frac{2a_{\text{WW}}}{r^2}\delta(r)\frac{\partial}{\partial r}r \\ \frac{2a_{\text{WW}}}{r^2}\delta(r)\frac{\partial}{\partial r}r & 0 \end{pmatrix}. \tag{7.53}$$

The strength of the coupling is given by a_{WW}, which has the dimension of a scattering length.

If one would only consider the Floquet channels $n = 0$ and $n = -1$ in the radial Floquet equation in coupled channel representation (6.11), one would recover the same Hamilton operator as (7.50), but with the parameters $a_0 = a_1 = \bar{a}$, $a_{\text{WW}} = \tilde{a}_1\bar{a}$ and $V = \hbar\omega$. In this model we want to go beyond and absorb the influence of higher Floquet channels of the side system in a_1, which does not have to be related to a_0, and a potential of the form $V = |n|\hbar\omega$. In Appendix C we derive the scattering amplitude of model (7.50) and see, that the inverse scattering amplitude can be approximated by the form

$$-\frac{1}{f} = \frac{1}{a_{\text{BG}}}\frac{\tilde{\omega} - \tilde{\omega}_0}{\tilde{\omega} - \tilde{\omega}_0 - \delta/\hbar} + i\gamma, \tag{7.54}$$

where we have introduced by

$$a_{\text{BG}} = a_0\left(1 - \frac{a_{\text{WW}}^2}{a_0 a_1}\right), \tag{7.55}$$

the background scattering length, which determines the scattering amplitude in the case of an infinitely large frequency ω. The width of the real part of the scattering amplitude corresponds to

$$\delta = \frac{2a_{\text{WW}}^2}{a_0 a_1|n|}\frac{1}{1 - \frac{a_{\text{WW}}^2}{a_0 a_1}}\frac{1}{a_1^2}. \tag{7.56}$$

The quantity

$$\gamma = k \tag{7.57}$$

characterises the width of the imaginary part and its inverse corresponds to the maximal value of the scattering amplitude. In practice, $\tilde{\omega}_0$, δ, γ and a_{BG} are fitting parameters and are extracted by fitting equation (7.54) to the numerical data for $\tilde{f}_0$. We can invert relations (7.55)-(7.57) in combination with (7.52) in order to calculate the parameters of the simple coupled channel model from the fitting parameters obtained with equation (7.54). The inverted relations read

$$\mathcal{E} = \gamma^2, \tag{7.58}$$

$$a_1 = \sqrt{\frac{1}{-\mathcal{E} + |n|\hbar\tilde{\omega}_0}}, \tag{7.59}$$

$$a_{\mathrm{WW}} = \sqrt{\frac{1}{2} a_{\mathrm{BG}} \delta a_1^3 |n|}, \tag{7.60}$$

$$a_0 = a_{\mathrm{BG}} + \frac{a_{\mathrm{WW}}^2}{a_1}. \tag{7.61}$$

Formula (7.54) has been reported recently by [80], but without the derivation shown in Appendix C. With the dimensionless variable

$$x = \hbar \frac{\tilde{\omega} - \tilde{\omega}_0}{\delta} \tag{7.62}$$

the scattering amplitude (7.54) is expressed in real and imaginary part

$$-\frac{\mathrm{Re}\ f}{a_{\mathrm{BG}}} = \frac{(x-1)x}{x^2 + \gamma^2 a_{\mathrm{BG}}^2 (x-1)^2}, \tag{7.63}$$

$$-\frac{\mathrm{Im}\ f}{a_{\mathrm{BG}}} = -\frac{\gamma a_{\mathrm{BG}} (x-1)^2}{x^2 + \gamma^2 a_{\mathrm{BG}}^2 (x-1)^2}. \tag{7.64}$$

In Figure 7.14 we compare these equations to the numerical data by simultaneously fitting real and imaginary part. Similar to Figure 7.12 we find a good agreement between approximative formula and numerical data. Panel **(d)** shows that equation (7.54) resolves the numerical data in the vicinity of the maximum of the real part, which is a benefit in comparison to equation (7.43). Also in this case we scaled both axis in order to plot the scattering amplitude for different parameters in a similar form.

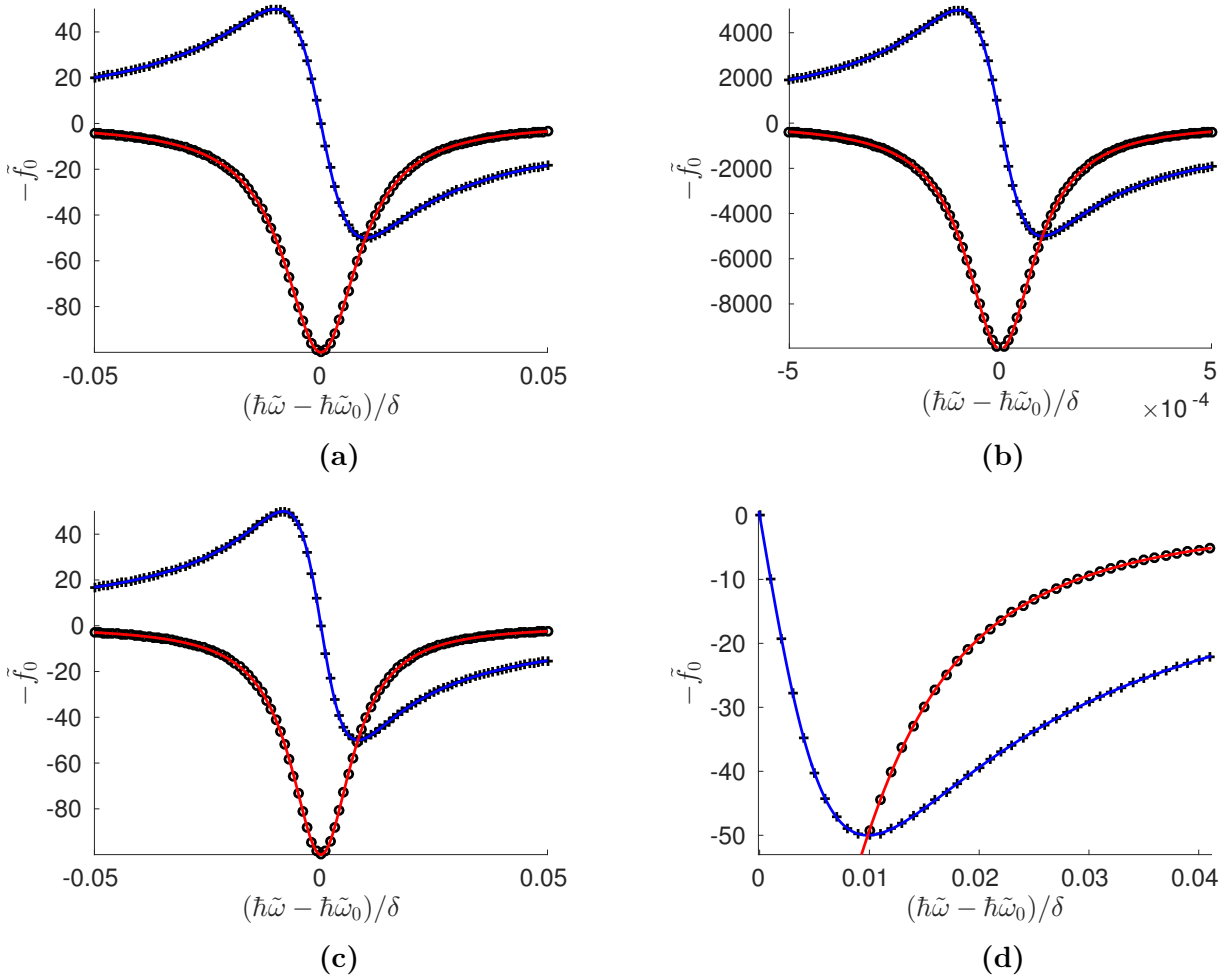

Figure 7.14.: Comparison of the real (blue) and imaginary (red) part of the scattering amplitude $-\tilde{f}_0$ over the difference of the driving frequency $\tilde{\omega}$ from the resonant $\tilde{\omega}_0$ measured in units of the width Δ. The values for fitting equation (7.43) are shown with + for real and o for imaginary part. Panel **(a)** shows the case of $\tilde{\epsilon} = 10^{-4}$ and $\tilde{a}_1 = 0.1$, which gave the result of $\hbar\tilde{\omega}_0 = 1.0174$, $\delta = 5.051 \times 10^{-3}$, $\gamma = 10^{-2}$ and $a_{\mathrm{bg}} = 0.995$. Panel **(b)** shows the case of $\tilde{\epsilon} = 10^{-8}$ and $\tilde{a}_1 = 0.1$, which gave the result of $\hbar\tilde{\omega}_0 = 1.0173$, $\delta = 5.0507 \times 10^{-3}$, $\gamma = 10^{-4}$ and $a_{\mathrm{bg}} = 0.995$. Panel **(c)** shows the case of $\tilde{\epsilon} = 10^{-4}$ and $\tilde{a}_1 = 0.5$, which gave the result of $\hbar\tilde{\omega}_0 = 1.6135$, $\delta = 0.1826$, $\gamma = 10^{-2}$ and $a_{\mathrm{bg}} = 0.8235$. Panel **(d)** shows an enlarged plot of the case of **(a)**.

The invariance between **(a)** and **(c)** is directly implemented in equations (7.63) and (7.64), as they are completely expressed by the dimensionless variable x. Because

$$\max \mathrm{Re}\ |f| = \frac{1}{2\gamma} \tag{7.65}$$

and

$$\max \mathrm{Im}\ |f| = \frac{1}{\gamma} \tag{7.66}$$

hold for equations (7.63) and (7.64), we see in Panel **(b)**, that a larger enhancement of scattering is described by a lower value of γ. In Figure 7.13 **(b)** we see that only the real part of the numerically calculated scattering amplitude has a zero, while (7.63) and (7.64) only simultaneously equal zero. This is a limitation of these approximate formulas.

Since it is important in the next Section, we show in Appendix D that for the limit of vanishing width γ formulas (7.63) and (7.64) converge to

$$-\lim_{\gamma\to 0} \mathrm{Re}\ f = a_{\mathrm{BG}} \left(1 - \frac{\delta}{\hbar\tilde{\omega} - \hbar\tilde{\omega}_0}\right). \tag{7.67}$$

for the real and

$$-\lim_{\gamma\to 0} \mathrm{Im}\ f(\tilde{\omega}) = -|\delta| a_{\mathrm{BG}} \pi \delta(\tilde{\omega} - \tilde{\omega}_0). \tag{7.68}$$

for the imaginary part. The real part fits with the corresponding result of (7.48), while the imaginary differs from (7.49) only by a modulus of δ.

7.5. Position and Width of Scattering Resonances

In this Section we use both equations (7.43) and (7.54) in order to extract fitting parameters characterising the scattering resonance. In particular we are interested in the position $\hbar\tilde{\omega}_0$ and the width Δ or δ. In Subsection 7.5.1 we evaluate the dependency of the fitting parameters on the Floquet energy $\tilde{\epsilon}$, while in Subsection 7.5.2 we evaluate their values in the $\tilde{\omega}$-$\tilde{a}_1$ plane.

7.5.1. Energy Dependence of Parameters

We now investigate the behaviour of the fitting parameters, which characterise a resonance. We therefore fit the formulas (7.43) and (7.54) to the numerical data and extract the dependencies of their parameters on the Floquet energy $\tilde{\epsilon}$. As the coefficient of determination R^2 [100] quantifies the accordance between the results of the fitting procedure to the data, only those fits yielding a coefficient of determination R^2 close to one are considered. The closer R^2 lies by one, the better the fit explains the data. We start with the width of the imaginary parts γ, respectively, Γ and found out that they depend on the Floquet energy in the following way

$$\log\gamma = p_1\ \log\tilde{\epsilon} + p_2, \tag{7.69}$$

$$\log\Gamma = p_1\ \log\tilde{\epsilon} + p_2. \tag{7.70}$$

We display this result in Figure 7.15 **(a)**. In Table 7.1 we see, that $p_1 \approx 0.5$, which implies the dependency of γ on $\tilde{\epsilon}$ by

$$\gamma \approx \sqrt{\tilde{\epsilon}}, \tag{7.71}$$

while in the case of equation (7.43) one has to multiply the right-hand side by a constant $C = 10^{p_1}$,

Table 7.1.: Results of the fitting procedure using equation (7.54) in the case of $\tilde{a}_1 = 0.1$ up to two decimals. Values in brackets give the 95% confidence interval.

Quantity	Formula	Values (95%-Confidence Bounds)	
γ	$\log\gamma = p_1 \log\tilde{\epsilon} + p_2$	p_1	0.50 $(0.50, 0.50)$
		p_2	3.14×10^{-5}
			$(2.78 \times 10^{-5}, 3.49 \times 10^{-5})$
a_{BG}	$a_{\mathrm{BG}} = c$	c	1 $(1,\ 1)$
δ	$\delta = a\ \tilde{\epsilon}^b + c$	a	2.38×10^{-4}
			$(1.32 \times 10^{-4},\ 3.44 \times 10^{-4})$
		b	1.08 $(1.08,\ 1.4)$
		c	5.05×10^{-3}
			$(5.05 \times 10^{-3},\ 5.05 \times 10^{-3})$
$\hbar\tilde{\omega}_0$	$\hbar\tilde{\omega}_0 = a\ \tilde{\epsilon}^b + c$	a	0.99 $(0.99,\ 0.99)$
		b	1.00 $(1.00,\ 1.00)$
		c	1.017 $(1.017,\ 1.017)$

Table 7.2.: Results of the fitting procedure using equation (7.43) in the case of $\tilde{a}_1 = 0.1$ up to two decimals. Values in brackets give the 95% confidence interval.

Quantity	Formula	Values (95%-Confidence Bounds)	
Γ	$\log\Gamma = p_1 \log\tilde{\epsilon} + p_2$	p_1	0.50 $(0.50, 0.50)$
		p_2	-2.32 $(-2.33,\ -2.31)$
a_{bg}	$a_{\mathrm{bg}} = c$	c	0.92 $(0.92,\ 0.92)$
Δ	$\Delta = a\ \tilde{\epsilon}^b + c$	a	3.2×10^{-2}
			$(-2.5 \times 10^{-1},\ 0.32)$
		b	1.33 $(-1.08,\ 3.75)$
		c	5.33×10^{-3}
			$(5.27 \times 10^{-3},\ 5.38 \times 10^{-3})$
$\hbar\tilde{\omega}_0$	$\hbar\tilde{\omega}_0 = a\ \tilde{\epsilon}^b + c$	a	0.99 $(0.99,\ 0.99)$
		b	1.00 $(1.00,\ 1.00)$
		c	1.017 $(1.017,\ 1.017)$

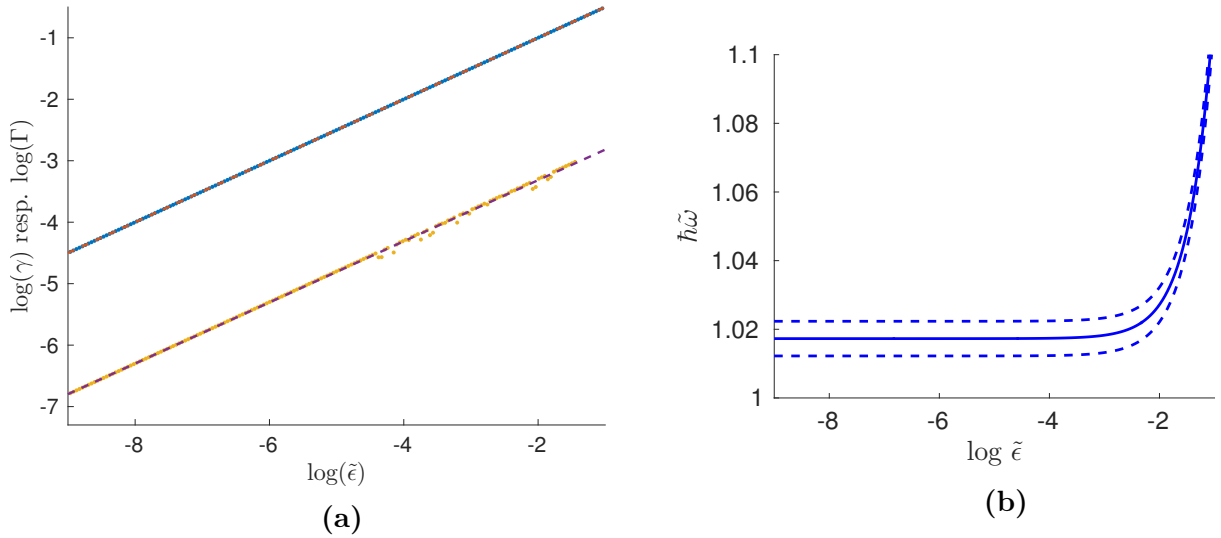

(a) **(b)**

Figure 7.15.: Panel **(a)** shows in blue the results of the fitting parameter γ of (7.54) and in yellow the results for Γ defined in (7.43). Linear fits for both data are shown in dashed lines. Panel **(b)** shows position $\hbar\tilde{\omega}_0$ and width δ (dashed lines) obtained with equation (7.54) of the first scattering resonance.

which is documented in Table 7.2 and gets

$$\Gamma = C\sqrt{\tilde{\epsilon}}. \tag{7.72}$$

Further investigations revealed, that equations (7.71) and (7.72) stay true in the case of larger $\tilde{a}_1$, while the constant C depends on $\tilde{a}_1$.

As the main result of this investigation we can state that in the limit of vanishing energy $\tilde{\epsilon}$ both γ and Γ are going to zero and therefore equations (7.63), (7.64) and (7.48), (7.49) are a valid description of the scattering resonance in the limit of vanishing Floquet energy $\tilde{\epsilon}$. As in both cases the imaginary part of the Floquet-scattering length is proportional to a Dirac-delta function, we conclude that the Floquet scattering resonance is lossless if the driving frequency does not exactly hit the resonant frequency $\hbar\tilde{\omega}_0$. One leading physical mechanism of losses is inelastic scattering. We show in Section 7.2 that all higher open Floquet channels possess a vanishing Floquet scattering length, which means that at scattering resonance inelastic collisions are not present.

We found out that the behaviour of the quantity $\hbar\omega_0$ as shown in Figure 7.15 is described by a power law

$$Q = a\ \tilde{\epsilon}^b + c. \tag{7.73}$$

In the case of a_{BG}, a_{bg}, δ and Δ a power law gives only the trend of the data and does not match to each single data point, as shown in Figure 7.16. The result of this investigation is shown in Tables 7.1 and 7.2. In Figure 7.15 **(b)** we see that both position and width stay approximately constant for Floquet energies below $\tilde{\epsilon} = 10^{-4}$.

As the coefficient of determination R^2 [100] quantifies the accordance between the results of the fitting procedure to the data, we compare the values of R^2 between (7.43) and (7.54). In Figure 7.16

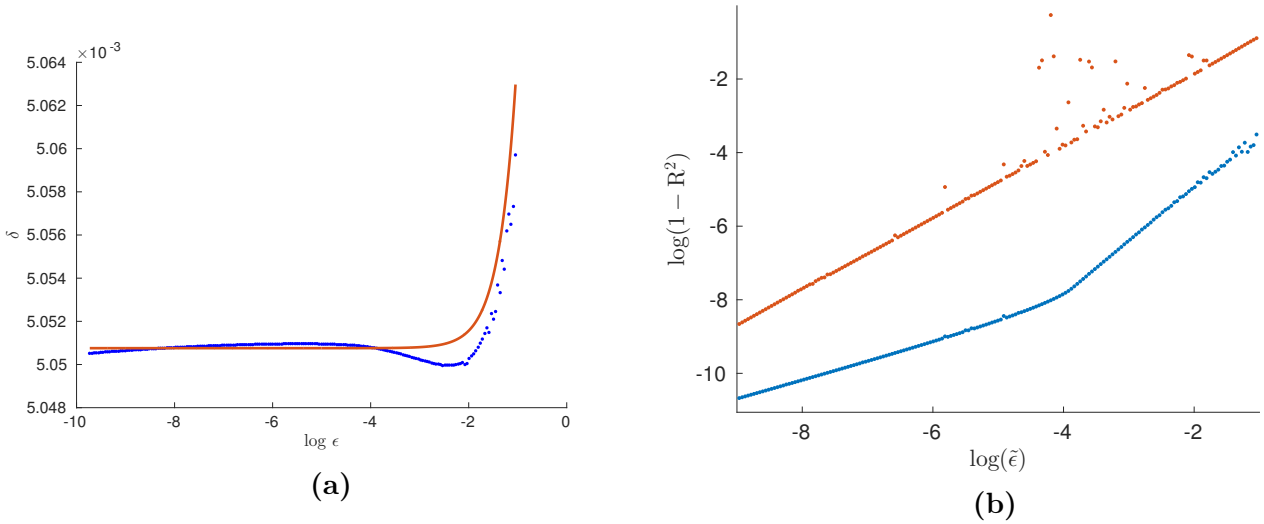

Figure 7.16.: (a): Plot of the fitting parameter δ (blue) and a power law fit (red). **(b)**: plot of the decade logarithm of $1 - R^2$ of the fit results with equation (7.54) (blue) and equation (7.43) (red) relative to the decade logarithm of the Floquet energy $\tilde{\epsilon}$ in the case of $\tilde{a}_1 = 0.1$.

we plot the logarithm of $1 - R^2$. The coefficient of determination gets closer to one in the case of vanishing Floquet energy $\tilde{\epsilon}$, signalling a better accordance of the fitting equations to the numerics. Additionally the values corresponding to (7.54) are always closer to one and therefore fit better to the data than the ones, which correspond to (7.43). We conclude that equation (7.54) is more suitable in order to describe the shape of a scattering resonance than (7.43). This is additionally manifested in numerical instabilities occurring in the fit results of equation (7.43) in the case of small Floquet energies $\tilde{\epsilon}$ and by the findings displayed in Panel **(d)** of Figures 7.12 and 7.14.

7.5.2. Position and Width in the $\tilde{\omega}$-$\tilde{a}_1$ Plane

After the investigation of the $\tilde{\epsilon}$ dependence of the scattering-resonance parameters we take a look on the behaviour of these resonances in the $\tilde{\omega}$-$\tilde{a}_1$ plane. We specialise to the case of vanishing Floquet energy. In order to calculate the numerical results, we use equation (6.42), which is valid for $\tilde{\epsilon} = 0$. Due to the considerations in the previous Subsection, we do a fitting procedure using equation (7.67). In Figure 7.17 we compare equation (7.67) to the numerical data and obtain a good agreement. It turns out that this fitting procedure yields good results, except for small values of $\tilde{a}_1$, as in this case the resonances become very narrow and the fitting procedure fails due to computational issues. In order to obtain results also in this region, we extrapolated the data to small $\tilde{a}_1$ and excluded data points with a large numerical uncertainty. This can be done with a high precision, as the resonance frequency at $\tilde{a}_1 = 0$ is known due to equation (7.29). As a result, we plot in Figure 7.18 position and width of the first five resonances in the $\tilde{\omega}$-$\tilde{a}_1$ plane. Similar to Figure 7.8 the resonance positions and widths increase for larger $\tilde{a}_1$. Figure 7.18 can be seen as a map of how to tune the parameters in order to form the shape of the resonance in a desired way. The time-averaged scattering length $\bar{a}$

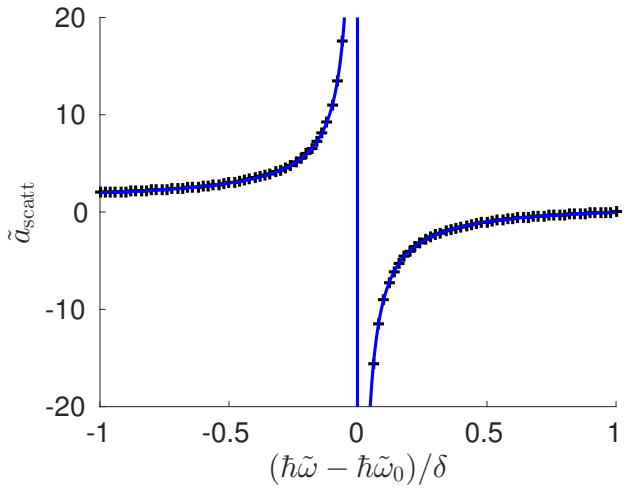

Figure 7.17.: Comparison of the numerical calculated scattering length $\tilde{a}_{\mathrm{scatt}}$ with the fitting equation (7.67) at $\tilde{a}_1 = 0.1$. The fitting procedure yields the values $\hbar\tilde{\omega}_0 = 1.0173$, $\delta = 5.0512 \times 10^{-3}$ and $a_{\mathrm{bg}} = 0.9949$.

in the contact interaction determines the energy and length scale, as it appears in $\hbar\tilde{\omega}$ via the dimer energy (6.34) and is used as a scaling factor connecting a_1 to the dimensionless $\tilde{a}_1$. Position $\hbar\tilde{\omega}_0$ and width δ of the resonance can be controlled by choosing the driving amplitude $\tilde{a}_1$. Finally, the driving frequency $\hbar\tilde{\omega}$ can be used to adjust the actual value of the scattering length $\tilde{a}_{\mathrm{scatt}}$ and for example control the enhancement over its background value.

In Figure 7.19 we compare the resonance positions to the ones obtained in Section 7.3 and find a good agreement, as the maximal error is of order 10^{-4}.

In Panel **(a)** of Figure 7.20 we plot the width of the first five resonances over the driving strength $\tilde{a}_1$ and report, that they increase with the driving strength. In order to characterise the width of the resonances further, we analyse their behaviour in the limit of low driving amplitudes $\tilde{a}_1$, and find out that the data can be described by a power law

$$\delta_n = a_n \, \tilde{a}_1^{b_n}. \tag{7.74}$$

In order to obtain the values of the fit parameters a_n and b_n in the limit of vanishing $\tilde{a}_1$, we successively restrict the data to be fitted to the values around zero. At last, we extrapolate these results to the case of $\tilde{a}_1 = 0$. The resulting values of a_n and b_n are shown in Table 7.3. The exponents b_n increase with the number n of the resonance and have the approximate behaviour

$$b_n \approx 2n. \tag{7.75}$$

In Panel **(b)** of Figure 7.20 we show the background scattering length a_{BG}, which is approximately one in the most cases and decreases in the case of the first resonance.

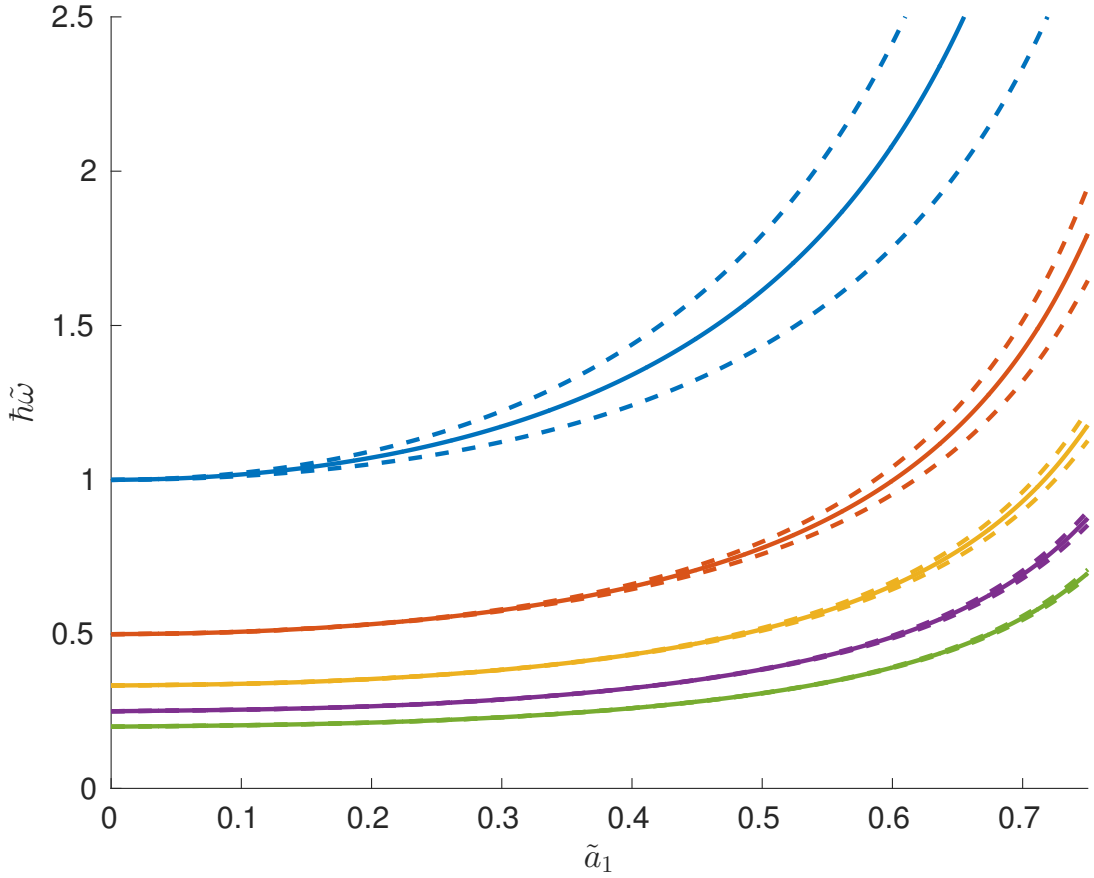

Figure 7.18.: Position and width of scattering resonances in the $\tilde{\omega}$-$\tilde{a}_1$ plane for Floquet energy $\tilde{\epsilon} = 0$. Positions are given by continuous lines, while widths are given by difference between dashed and continuous lines of the same colour. The quantities for first resonance are painted blue, for second red, for third yellow, for fourth purple and for fifth green.

7.5.3. Relation to Simple Coupled Channel Model

In this Section we calculate with equations (7.58)-(7.61) the parameters of the simple coupled channel model from the fit parameters obtained with equation (7.54). In Figure 7.21 we plot the dependencies of the model parameters over the driving strength $\tilde{a}_1$ using the data from the fitting procedure with equation (7.54). As the width of the imaginary part γ is zero for vanishing Floquet energy $\tilde{\epsilon}$, the energy $\mathcal{E}$ in the model does also vanish. The value of a_0 approximately follows the value of a_{BG}, while a_1 is decreasing with increasing $\tilde{a}_1$ in order to lower the energy of the model bound state such that the behaviour of the energy of the side system is reproduced. It turns out that all considered scattering resonances have approximately the same value of a_1. For small $\tilde{a}_1$ the value of a_{WW} is close to zero and it increases with larger $\tilde{a}_1$. This can be understood by the fact that $\tilde{a}_1$ couples the open Floquet channels to the driving induced bound state in the Floquet-side bands, and the width is related to the coupling strength by equation (7.56). For larger values of $\tilde{a}_1$ and for higher resonance numbers the coupling strength decreases. An intuitive explanation is that higher Floquet

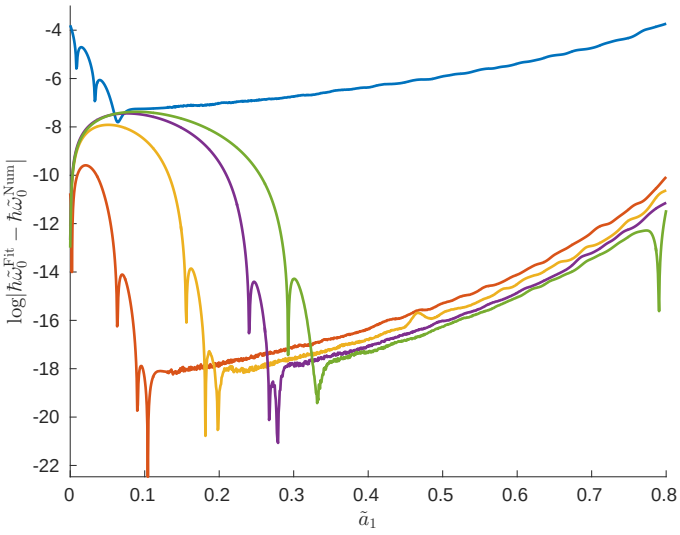

Figure 7.19.: Plot of the decade logarithm of the difference between the resonance positions calculated by the fitting procedure (7.54) and by the energy of the side system (7.14). The quantities for the first resonance are painted blue, for the second red, for the third yellow, for the fourth purple and for the fifth green.

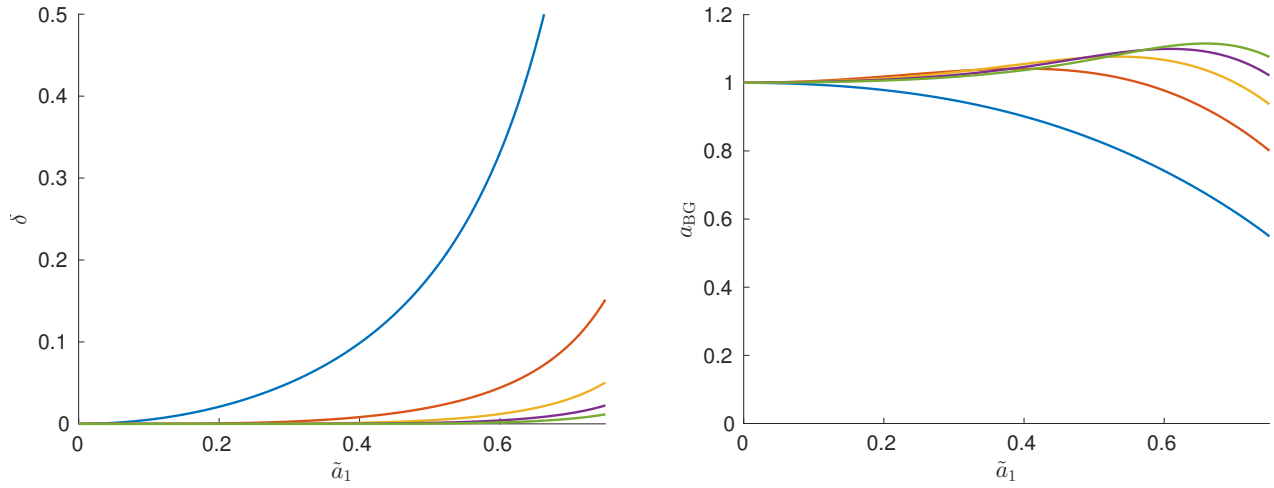

(a) **(b)**

Figure 7.20.: **(a):** Plot of the resonance width δ over the driving strength $\tilde{a}_1$. **(b)**: Plot of the background scattering length a_{BG} of the resonance. The width for the first resonance is painted blue, for the second red, for the third yellow, for the fourth purple and for the fifth green.

Table 7.3.: Results of the fitting procedure for widths of the resonances $\delta = a\ \tilde{a}_1^b$ in the limit of vanishing $\tilde{a}_1$ up to two decimals. Values in brackets give the 95% confidence bounds.

Number	a_n	b_n
1	0.48 (0.44, 0.55)	2.00 (1.97, 2.03)
2	0.36 (0.32, 0.39)	4.00 (3.97, 4.02)
3	0.34 (0.26, 0.42)	5.94 (5.83, 6.05)
4	0.33 (0.19, 0.48)	7.79 (7.54, 8.05)
5	0.42 (0.26, 0.58)	9.83 (9.63, 10.03)

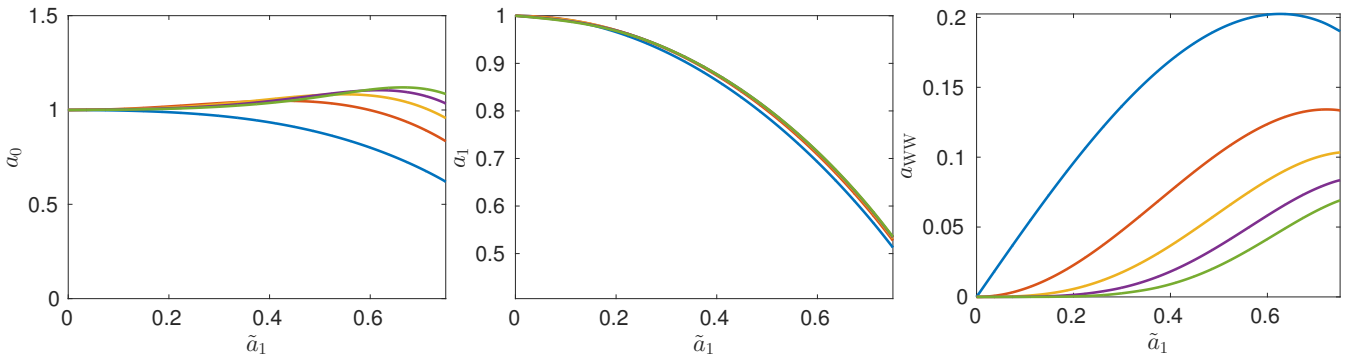

(a) **(b)** **(c)**

Figure 7.21.: Plot of the parameters of the simple coupled channel model of Section 7.4.2 over the driving strength $\tilde{a}_1$. In **(a)** the background scattering length of the free channel is plotted, in **(b)** the one for the closed and in **(c)** the coupling strength of both channels, which are present in the model. Quantities for first resonance are painted blue, for second red, for third yellow, for fourth purple and for fifth green.

channels get more populated and therefore the overlap between the wave functions in different modes becomes smaller. This results in an effective smaller coupling of the channels. Note that these model parameters exist due to simplification issues and are no measurable quantities.

7.6. Kramers-Kronig like Relation between Real and Imaginary Part

After the detailed analysis of the scattering resonances we report that the following quantity involving the time-averaged scattering amplitude

$$\tilde{\chi}(\omega) = -f_0(\omega) + \lim_{\omega\to\infty} f_0(\omega) \tag{7.76}$$

fulfils the so called anti Kramers-Kronig relations

$$\text{Re } \tilde{\chi}(\omega_0) = -\frac{1}{\pi}\mathbb{P}\int_{-\infty}^{\infty} d\omega \frac{\text{Im } \tilde{\chi}(\omega)}{\omega - \omega_0}, \tag{7.77}$$

$$\text{Im } \tilde{\chi}(\omega_0) = \frac{1}{\pi}\mathbb{P}\int_{-\infty}^{\infty} d\omega \frac{\text{Re } \tilde{\chi}(\omega)}{\omega - \omega_0}, \tag{7.78}$$

which are derived in Appendix B for anti-causal susceptibilities. We introduced the principal value integral as

$$\mathbb{P}\int_{-\infty}^{\infty} dx \frac{\tilde{\chi}(x)}{x - x_0} = \lim_{\gamma\to 0}\left(\int_{-\infty}^{x_0-\gamma} dx + \int_{x_0+\gamma}^{\infty} dx\right)\frac{\tilde{\chi}(x)}{x - x_0} \tag{7.79}$$

and use the quantity $\tilde{\chi}(\omega) = -f_0(\omega) + \lim_{\omega\to\infty} f(\omega)$ instead of the bare scattering amplitude $-f_0(\omega)$ in order to ensure that the limit of $\tilde{\chi}(\omega)$ for infinite frequencies is going to zero. We show in Appendix B, that this condition is necessary for the fulfilment of the anti-Kramers Kronig relations. The fact that (7.76) fulfils equations (7.77) and (7.78) is not a violation of causality, as (7.76) is not a susceptibility. The fulfilment of the anti-causal Kramers Kronig relations signals that the scattering amplitude $f_0(\tilde{\omega})$ has a simple analytic structure, which captures the physics of a scattering resonance. In Appendix B we further show, that functions with poles in the upper complex half plane fulfil the anti-Kramers Kronig relations. As both fit formulas (7.43) and (7.54) have only one pole, which is located in the upper half plane for positive γ or Γ, respectively, they also fulfil equations (7.77) and (7.78).

In order to show that the numerically calculated values fulfil the anti-Kramers-Kronig relations, a MATLAB function was implemented in order to calculate the imaginary part of the scattering amplitude using the real part with equation (7.78) and vice versa with (7.77). The function is implemented in the following way: The integrals in (7.77) and (7.78) are truncated to a range of total length 2Λ lying symmetrically around the point ω_0. This is done in order to ensure that

$$\mathbb{P}\int_{-\Lambda+\omega_0}^{\Lambda+\omega_0} dw \frac{1}{\omega - \omega_0} = 0. \tag{7.80}$$

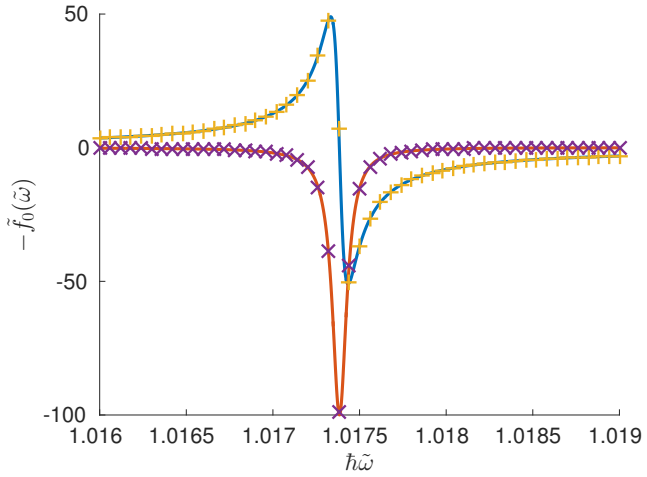

Figure 7.22.: Plot of real (blue) and imaginary (red) part of the negative scattering amplitude in the case of $\tilde{\epsilon} = 10^{-4}$, $\tilde{a}_1 = 0.1$. The yellow + mark the values obtained by re-calculating the real part using the imaginary by equation (7.77). The purple x are calculated using equation (7.78).

Additionally we approximate the principal value by leaving out the integration between the values $\omega_0 - \epsilon_p$ and $\omega_0 + \epsilon_p$, where ϵ_p is a small, but numerical resolvable value. The numerics have been validated with the function $\tilde{\chi}_{\text{val}}(\omega) = 1/(\omega + i\gamma)$, which has a pole in the upper complex half plane for $\gamma < 0$ and therefore known to fulfil the anti-Kramers-Kronig relations.

The result of this investigation is shown in Figure 7.22, where a good agreement between numerical and anti-Kramers-Kronig relations calculated data is shown. In Figure 7.23 we plot the relative norm

$$\frac{|\tilde{\chi}_{\text{numeric}}(\omega) - \tilde{\chi}_{\text{anti-Kramers-Kronig}}(\omega)|}{|\tilde{\chi}_{\text{numeric}}(\omega)|} \tag{7.81}$$

of the error between numerical and anti-Kramers-Kronig calculated data. For all considered positions in the $\tilde{\epsilon}$-$\tilde{a}_1$ plane this error has the order of the numerical uncertainty of the method.

Additionally we can directly show that (7.43) and (7.54) fulfil the anti-Kramers-Kronig relations in the case of positive imaginary part γ or Γ, respectively, by calculating the principal value integral in the following manner

$$\mathbb{P}\int_{-\infty}^{\infty} dx \frac{\tilde{\chi}(x)}{x - x_0} = \lim_{\gamma\to 0, \Lambda\to\infty} \left(\int_{-\Lambda+x_0}^{x_0-\gamma} dx + \int_{x_0+\gamma}^{\Lambda+x_0} dx \right) \frac{\tilde{\chi}(x)}{x - x_0}. \tag{7.82}$$

It turns out that in the case of (7.43) and (7.54) both in equation (7.82) occurring limits commute.

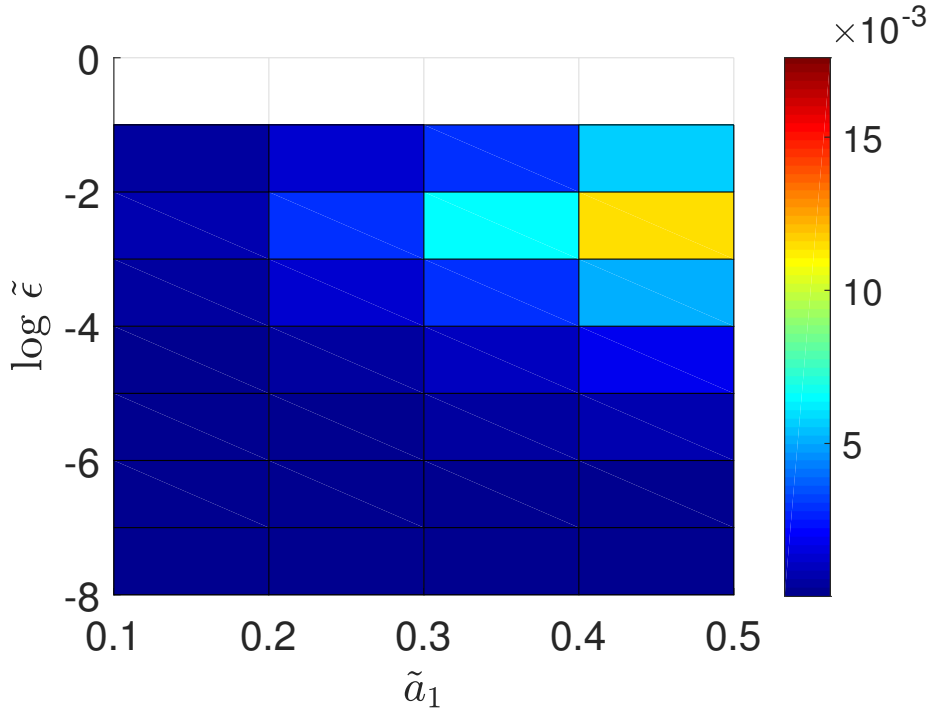

Figure 7.23.: Plot of the relative error (7.81) of numerical data and anti-Kramers-Kronig relation recalculated data in the plane of Floquet energy $\tilde{\epsilon}$ and driving strength $\tilde{a}_1$.

7.7. Scattering Amplitude at Large Driving Frequencies

In this Section we consider the limit of infinitely large driving frequencies. In this case the wave functions in all Floquet channels with index greater than zero are unbound, while all below are bound. Interestingly, the coefficients D_n obey the rule $D_n = D_{-n}$, as the recursion relation (6.49) is the same in both cases. Therefore the amplitude of the wave function in both open and closed Floquet channels are distributed symmetrically around channel number zero in this limit. The scattering amplitude can be calculated with the results obtained in Section 6.4 by inserting equation (6.54) into (6.26) and it reads

$$\tilde{f}_0(\tilde{\epsilon}, \tilde{a}_1) = \frac{-\sqrt{1-\tilde{a}_1^2} + i(1-\tilde{a}_1^2)\tilde{k}_0}{1+\sqrt{1-\tilde{a}_1^2}\,k_0}. \tag{7.83}$$

As equation (7.83) has no dependency on the driving frequency, this result corresponds to the limit of infinite large driving frequency without any $1/\tilde{\omega}$ correction. A plot of (7.83) in the $\tilde{\epsilon}$-$\tilde{a}_1$ plane is performed in Figure 7.24. If $\tilde{a}_1 = 1$, real and imaginary part of the scattering amplitude vanishes. For the limit of $\tilde{\epsilon}$ going to zero the imaginary part vanishes, while the real part converges to $\tilde{a}_{\text{scatt}} = \sqrt{1-\tilde{a}_1^2}$. This is quite remarkable, as for large driving frequencies one would expect, that the effect of the time-dependent part vanishes due to averaging issues, which leads to a scattering length of $\tilde{a}_{\text{scatt}} = 1$. Additionally no resonances occur, as the condition of maximal scattering (7.7) can never be fulfilled by equation (7.83).

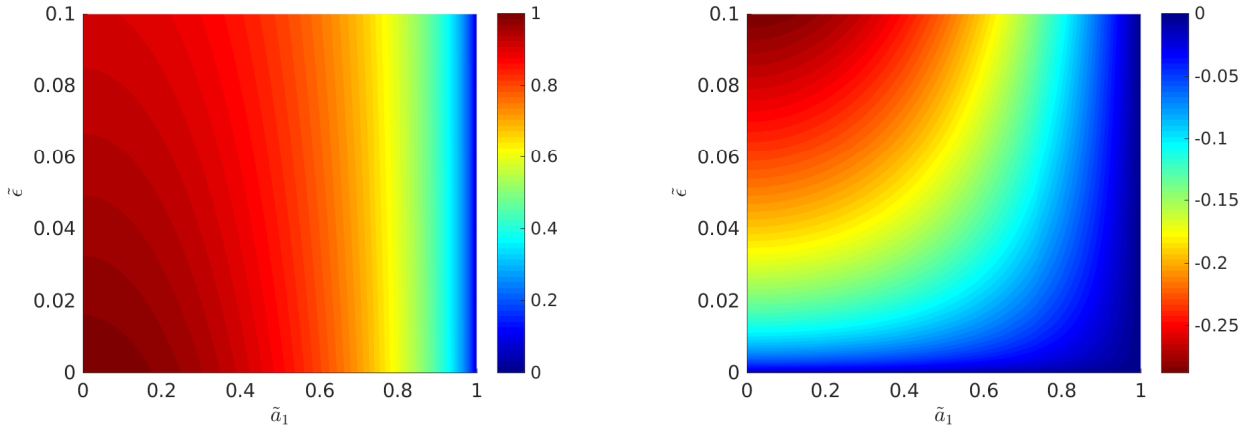

(a) **(b)**

Figure 7.24.: Real **(a)** and imaginary **(b)** part of the negative scattering amplitude $-\tilde{f}_0$ in the case of infinite large driving frequency $\tilde{\omega}$.

7.8. Scattering Amplitude at Low Driving Frequencies

In this Section we discuss the case of vanishing driving frequency, in which condition (6.56) is fulfilled. In this limit the critical index (5.24) diverges to minus infinity and all Floquet channels capturing a relevant weight of the wave function are unbound. Due to the absence of bound states no resonances occur in this limit. In Section 6.4.3 we solve the recursion relation (6.37) in the case of vanishing driving frequency. Plugging the (6.63) into (6.40), we arrive at a time-averaged scattering amplitude of

$$\tilde{f}_0 = \frac{i}{\tilde{k}_0} - \frac{1}{\tilde{k}_0\sqrt{-1+\tilde{k}_0\left(-\tilde{a}_1^2\tilde{k}_0+\tilde{k}_0-2i\right)}}. \tag{7.84}$$

In order to find a result being easier to interpret, we perform the limit of vanishing energy of (7.84). As the driving frequency is exactly zero, equation (6.56) is always valid in this limit. The complex roots occurring in this calculation are considered to be the principal square root [85, 101]. The resulting time-averaged scattering length is

$$\tilde{a}_0^{\mathrm{Fl}} = 1. \tag{7.85}$$

Additionally we can show, that in those limits $-\tilde{f}_{\pm1}$ converges to

$$\tilde{a}_{\pm1}^{\mathrm{Fl}} = \frac{\tilde{a}_1}{2}, \tag{7.86}$$

while the scattering amplitudes of all other channels vanish. By extrapolating this limit to small, but finite, driving frequencies $\tilde{\omega}$, we can write down the time dependent scattering length

$$\tilde{a}^{\mathrm{Fl}}(t) = 1 + \tilde{a}_1\cos(\omega t). \tag{7.87}$$

This is an interesting result, as it states that for low driving frequencies the Floquet-scattering length equals the scattering length involved in the driving potential (6.2), i.e. the scattered particle follows

the potential adiabatically.

We show in Appendix E that the time dependent Floquet-scattering length can be identified with the scattering length appearing in the interaction term of the Gross-Pitaevskii equation. Therefore, equation (7.87) is supported by the investigations [1, 48] of collective excitations of a Bose-Einstein condensate induced by a periodically modulated scattering length.

We now sum up the most important points of this Chapter. We considered the scattering by a periodically driven contact potential and saw in Section 7.1 that periodic driving is able to create scattering resonances, which allow the tuning of the interaction strength to any desired value. We explained in Section 7.2 that their emergence is related to Fano interference and we could show that they occur, if the energy of the incoming particle equals the energy of a bound state in the continuum. With this result we calculated in Section 7.3 the positions of scattering resonances. In Section 7.4 we showed, that the shape of a scattering resonance can be approximated by simple formulas. We used these formulas in a fitting procedure and characterised the scattering resonance by their fitting parameters, which we determined in Section 7.5 in the $\tilde{\omega}$-$\tilde{a}_1$ plane. In Section 7.6 we reported, that the scattering amplitude in the vicinity of a resonance fulfils the so-called anti-Kramers-Kronig relations. After a detailed analysis of the sinusoidally driven contact potential we characterise in the next Chapter the influence of higher harmonics of the driving scheme on the scattering resonances.

8. Influence of Higher Fourier Modes of the Driven Potential

This Chapter is devoted to the better understanding of higher Fourier modes of the driven contact potential, as it plays a role for experimental applications. If, as considered in Ref. [3], a time-periodic magnetic field

$$B(t) = B_1 + B_2 \cos(\omega t) \tag{8.1}$$

is applied in the vicinity of a magnetic Feshbach resonance, it leads to a time-dependent scattering length

$$a(t) = a_{\mathrm{bg}} \left(1 - \frac{\Delta}{B_2 \cos(\omega t) + B_1 - B_0} \right). \tag{8.2}$$

For small driving amplitudes $B_2 \ll |B_1 - B_0|$ this time-dependent scattering length can be approximated by only considering the first Fourier component as in Chapter 6 or Rev. [3]. In order to consider higher harmonics, we solve in Section 8.1 the scattering by a contact potential which has an arbitrary, but periodic, time-dependence and map the solution of the scattering problem to a relation between Floquet-scattering amplitudes of different channels. Section 8.2 is devoted to the better understanding of the influence of higher Fourier modes in the potential, while Section 8.3 applies these findings to the case of a periodically driven magnetic Feshbach resonance. In Section 8.4 we calculate the frequency and length scales of a driven scattering resonance in the case of ^{85}Rb and ^{133}Cs atoms.

8.1. Contact Potential with General Time-Periodic Driving

We consider the contact interaction introduced in Chapter 6 by equation (6.1) and assume a general time-periodic scattering length, which can be represented as a Fourier series

$$a(t) = \sum_{n=-\infty}^{\infty} e^{-in\omega t} A_n. \tag{8.3}$$

If the contact potential is considered to be hermitian, its Fourier components fulfil the relation

$$A_n = A_{-n}^*. \tag{8.4}$$

In this case the radial Floquet equation (5.37) with zero angular momentum of the driven contact potential reads

$$\left(\Delta_r + k_n^2\right) R_n(r) = \sum_{m=-\infty}^{\infty} 2\frac{A_m}{r^2}\delta(r)\frac{\partial}{\partial r} r R_{n-m}(r). \tag{8.5}$$

As we consider s-wave scattering only, we omit similar to Chapter 6 the angular momentum index of the wave function. Although equation (8.5) differs from (6.11) by including Fourier components of the potential A_n with an index larger than one, it is solved by the same ansatz (6.12) assuming condition (6.14). The integration procedure around the singularity introduced in Chapter 6 is also applied to this setting and leads to a relation connecting potentially all coefficients D_n

$$\left(\frac{i}{\tilde{k}_n} - 1\right) D_n - \sum_{\substack{m=-\infty \\ m\neq 0}}^{\infty} \tilde{A}_m D_{n-m} = \tilde{h}_n. \tag{8.6}$$

The inhomogeneity is given by

$$\tilde{h}_n = \begin{cases} \left(\frac{i}{\tilde{k}_n \bar{a}} + 1\right) \frac{1}{2}, & n = 0 \\ \frac{\tilde{A}_n}{2}, & n \neq 0. \end{cases} \tag{8.7}$$

As A_0 plays the role of $\bar{a}$ in Chapter 6, we introduced the dimensionless wave vector $\tilde{k}_n = k_n A_0$, scattering amplitude $\tilde{f}_n = f_n/A_0$ and defined the normalised Fourier components of the potential by

$$\tilde{A}_n = \frac{A_n}{A_0}. \tag{8.8}$$

Re-expressing the coefficients D_n by the scattering amplitudes (6.40) in equations (8.6) and (8.7) leads to the relation

$$-(1 + i\tilde{k}_n)\tilde{f}_n - i \sum_{\substack{m=-\infty \\ m\neq 0}}^{\infty} \tilde{A}_m \tilde{k}_{n-m} \tilde{f}_{n-m} = \tilde{A}_n. \tag{8.9}$$

This equation is due to the occurrence of the Floquet-wave vector $\tilde{k}_n$ non-linear in the Fourier index n and has also been obtained by Ref. [4] with a different approach. As it connects coefficients, whose indices differ by an integer n we can interpret the effect of $\tilde{A}_n$ as the strength of processes involving $|n|$ quanta of the drive field. Due to its complexity, equation (8.9) can be only solved numerically. In this case a truncation scheme similar to Section 6.4 is performed. First of all, only Fourier components $\tilde{A}_n$ with indices having a modulus smaller than a cut-off m_1 are considered. This approximation is only valuable, if Fourier-components $\tilde{A}_n$ with large indices vanish. Then equation (8.9) is truncated by setting all $\tilde{f}_n$ with indices having a modulus larger than a cut-off m_2 to zero. It is useful to consider $m_1 < m_2$. The result is a set of linear equations, which is solved numerically.

Also in this case, the knowledge of the time-averaged scattering amplitude $\tilde{f}_0$ suffices to calculate both elastic and inelastic cross section and the time-averaged scattering length $\tilde{a}_{\mathrm{scatt}}$.

8.2. Commensurate Two Colour Drive

In order to understand the effect of higher Fourier modes of the potential in the simplest case, we assume the driven scattering length to be of the form

$$a(t) = A_0 + 2A_1 \cos(\omega t) + 2A_2 \cos(2\omega t). \tag{8.10}$$

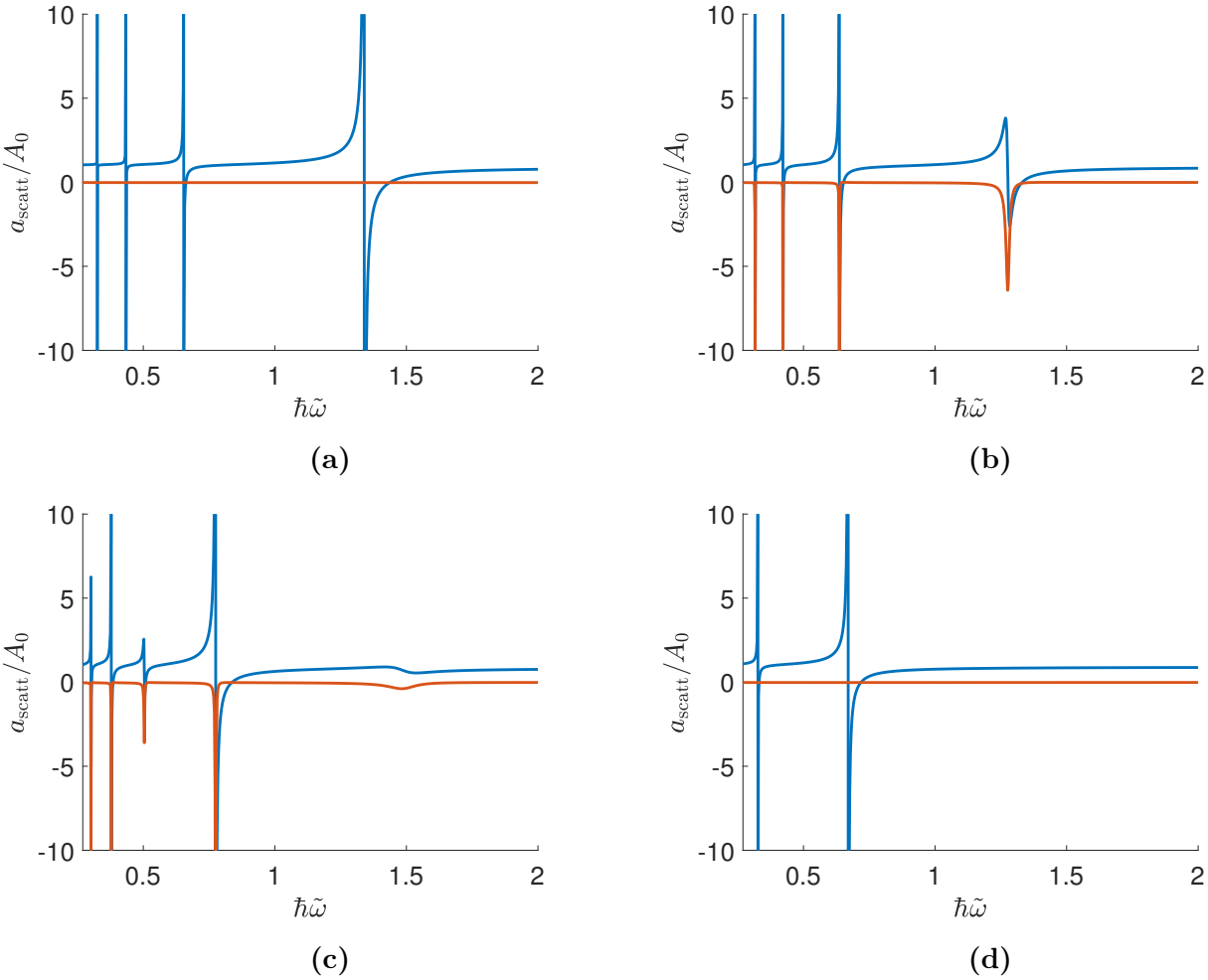

Figure 8.1.: Plots of real (blue) and imaginary (red) part of the time-averaged scattering length a_{scatt} for $\tilde{\epsilon} = 0$ and the following parameters:
(a): $\tilde{A}_1 = 0.2$, $\tilde{A}_2 = 0.0$, **(b)**: $\tilde{A}_1 = 0.2$, $\tilde{A}_2 = 0.08$, **(c)**: $\tilde{A}_1 = 0.2$, $\tilde{A}_2 = 0.2$, **(d)**: $\tilde{A}_1 = 0.0$, $\tilde{A}_2 = 0.2$

For $A_2 = 0$ this equation reduces to (6.2) with $2A_1 = a_1$. In order to give an overview of the effects of the additional Fourier component $\tilde{A}_2$, we show in Figure 8.1 cuts along the $\tilde{\omega}$-axis of the time-averaged scattering length, i.e. we set $\tilde{\epsilon} = 0$, as in this case the resonances are strongest. Panel **(a)** shows the case of no additional Fourier component. There we observe scattering resonances

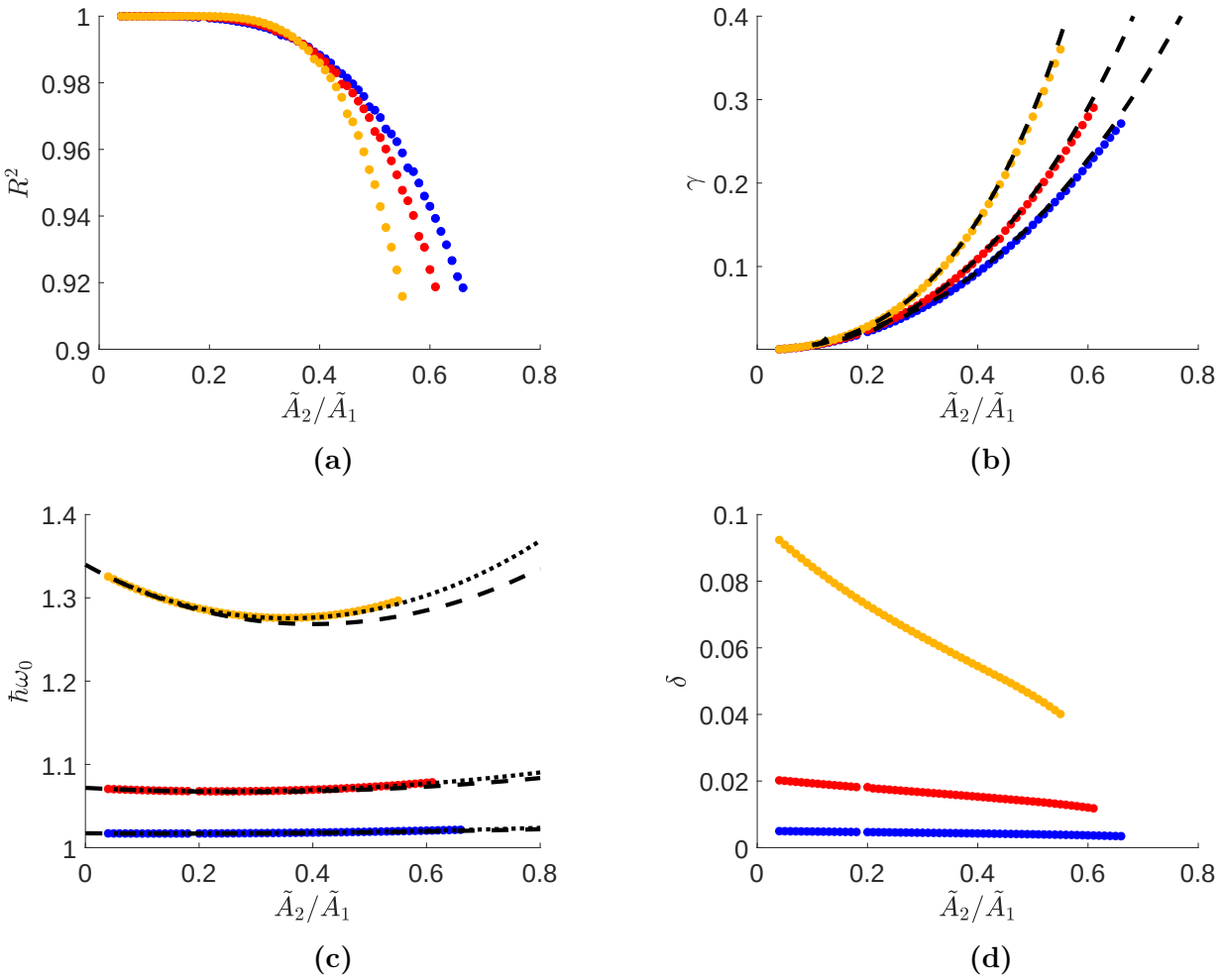

Figure 8.2.: Plots of the following fitting parameters for $\tilde{A}_1 = 0.05$ in blue, $\tilde{A}_1 = 0.1$ in red and $\tilde{A}_1 = 0.2$ in yellow:
(a): Coefficient of determination R^2 of the corresponding fitting procedure coloured for different $\tilde{A}_1$. **(b)**: Imaginary part γ coloured for different $\tilde{A}_1$, $1/\max|\mathrm{Im}\ a_{\mathrm{scatt}}|$ with black dashed line. **(c)**: Resonant frequency $\hbar\omega_0$ coloured for different $\tilde{A}_1$, $\hbar\omega_{\mathrm{side}}$ with black dashed line, position of maximal imaginary part with black dotted line, **(d)**: Width of the resonance δ coloured for different $\tilde{A}_1$.

with a large enhancement of the real part of the scattering amplitude, while the imaginary part is zero except of non-shown delta-peaks exactly at the resonance positions. In Panel **(b)** we switch on the Fourier component $\tilde{A}_2$ slightly and observe a non-vanishing imaginary part in the vicinity of all scattering resonances. This effect is strongest for the resonance with largest frequency, also the maximal real part is finite in this case. Panel **(c)** shows the case where $\tilde{A}_1$ and $\tilde{A}_2$ are equal. Here, this effect is stronger and involves a lower maximal real part for multiple resonances. This effect is enhanced only at every second resonance. Panel **(d)** shows the case for $\tilde{A}_1 = 0$, where only half of the resonances occur. This has been expected, as it should be recovered with the methods of Chapter 6 while driving with the double driving frequency. As a non-vanishing imaginary part of

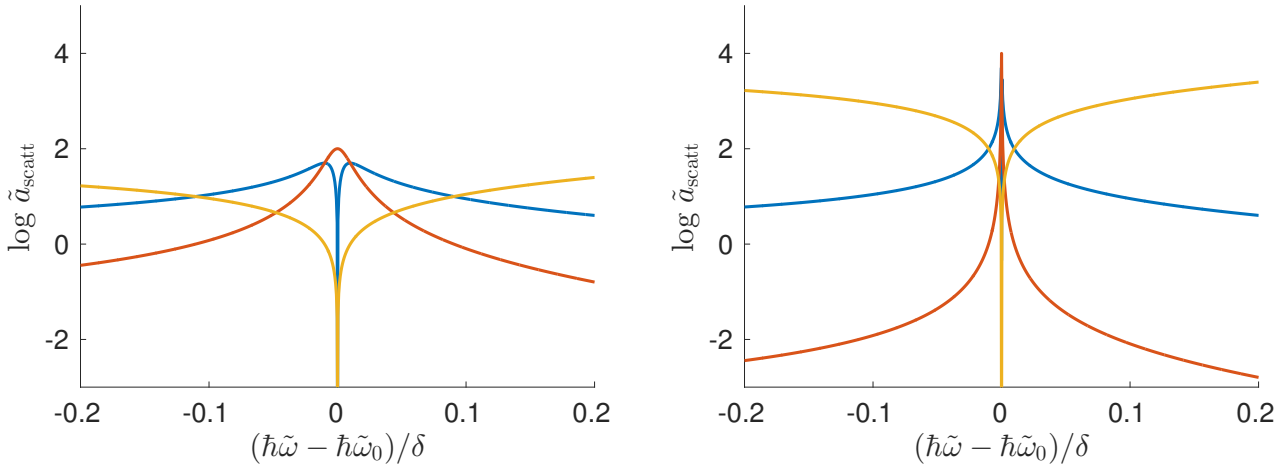

Figure 8.3.: Decade logarithm of modulus of real (blue) and imaginary (red) part of equation (8.11) for the parameters $a_{\text{BG}} = 1$, $\gamma = 10^{-2}$ **(a)** and $a_{\text{BG}} = 1$, $\gamma = 10^{-4}$ (**b**). The yellow curve in both panels shows the quantity $\log(|\text{Re}\ \tilde{a}_{\text{scatt}}/\text{Im}\ \tilde{a}_{\text{scatt}}|)$.

the scattering length $\tilde{a}_{\text{scatt}}$ is associated with particle loss, its occurrence limits the applicability of our method. In order to obtain a strong enhancement of elastic scattering without strong particle loss, one has to tune the frequency on the flank of the resonance, where the real part is much larger than the imaginary.

In the following we give a more quantitative insight in the dependency of the resonance with largest frequency on the Fourier component $\tilde{A}_2$. As the time-averaged scattering length $\tilde{a}_{\text{scatt}}$ looks in the presence of higher Fourier components of the potential similar to (7.54), we fit the numerical data to the following approximate formula

$$\frac{1}{a_{\text{scatt}}(\omega)} = \frac{1}{a_{\text{BG}}} \frac{\tilde{\omega} - \tilde{\omega}_0}{\tilde{\omega} - \tilde{\omega}_0 - \delta/\hbar} + i\gamma. \tag{8.11}$$

Figure 8.2 shows the dependency of the fitting parameters on the Fourier component $\tilde{A}_2$. As it is shown in Panel **(a)**, this fit works well for small values of $\tilde{A}_2$, while for higher $\tilde{A}_2$ the lowering of the coefficient of determination R^2 indicates a lower conformity of equation (7.54) and the numerical data. We only considered data with a coefficient of determination larger than $R^2 \geq 0.915$. In Panel **(b)** the imaginary part γ is shown. As expected it vanishes for small $\tilde{A}_2$ and reproduces the findings in Chapter 7. With increasing $\tilde{A}_1$ also γ increases following a power-law behaviour

$$\gamma = a \left(\frac{\tilde{A}_2}{\tilde{A}_1} \right)^b. \tag{8.12}$$

As the imaginary part of the scattering length $\tilde{a}_{\text{scatt}}$ can be related by (5.68) to inelastic scattering, the occurrence of higher harmonics in the driving scheme leads to a lossy driving induced resonance. These losses occur, as for $\tilde{A}_2 \neq 0$ the side systems is no more decoupled from the open channels and

therefore no bound state in the continuum occurs. Instead higher Floquet channels obtain a non-vanishing occupation leading to inelastic scattering. In Figure 8.3 we display the decade logarithm of real and imaginary part of equation (8.11) and see that in the vicinity of a resonance the imaginary is larger than the real part. The yellow curve shows the quantity $\log(|\mathrm{Re}\ \tilde{a}_{\mathrm{scatt}}/\mathrm{Im}\ \tilde{a}_{\mathrm{scatt}}|)$ which has a minimum exactly at resonance position. In order to get a large real part with a relatively small imaginary part, one has to tune the driving frequency on the flank of the resonance, and, as the comparison between Figure 8.3 **(a)** and **(b)** shows, lower the parameter γ. In Figure 8.2 **(b)** we show in a black dashed line the quantity $1/\max|\mathrm{Im}\ \tilde{a}_{\mathrm{scatt}}|$, which should equal γ in the ideal case. Indeed, we get a good agreement of both quantities verifying the correctness of the fitting procedure. Figure 8.2 **(c)** shows, that the change of $\tilde{A}_2$ also changes the resonant frequency slightly compared to $\tilde{A}_2 = 0$. The black dashed lines are calculated by evaluating the eigenenergies of the side system while assuming condition (7.18). We generalised the calculation presented in Section 7.3 to the case where $\tilde{A}_2$ is non-zero by introducing next-nearest neighbour coupling $\tilde{A}_2$ of the side systems channels while assuming that the coupling to the open channels completely vanishes. Although both lines posses similar qualitative behaviour, they deviate from each other especially in the case of large $\tilde{A}_2$. This deviation can shows that the assumption of an uncoupled side system is not true in this case. The non-vanishing next-nearest neighbour coupling of closed and open channels by $\tilde{A}_2$ leads in the sense of equation (3.8) to a shift of the resonance position. The black dotted lines show the frequency position of maximal enhanced scattering and it fits well to the data obtained by the fitting procedure. Figure 8.2 **(d)** shows that the width δ of the resonances lower with increasing $\tilde{A}_1$.

We saw by this investigation that position and width of the scattering resonances are altered by the value of $\tilde{A}_2$. But most important is that a non-vanishing $\tilde{A}_2$ implies a finite maximal scattering length, which is manifested at zero energy $\tilde{\epsilon} = 0$ by a non-vanishing width γ. This findings are important for the discussion in the next Section.

8.3. Periodically Driven Magnetic Feshbach Resonance

In this Section we consider the case of a periodically driven magnetic Feshbach resonance. As introduced in the beginning of this Chapter we consider a contact potential with a time-periodic scattering length following equation (8.2). Its Fourier components are defined by

$$A_n = \frac{1}{T}\int_0^T dt e^{in\omega t}\left(1 - \frac{\Delta}{B_2\cos(\omega t) + B_1 - B_0}\right). \tag{8.13}$$

This integral can be mapped by the substitution $z = e^{i\mathrm{sign}(n)\omega t}$ to a line integral on the complex unit sphere. Using the residue theorem and assuming $B_2 < |B_1 - B_0|$ equation (8.13) is evaluated to

$$A_n = a_{\mathrm{bg}}\left\{\delta_{n,0} - \frac{\Delta}{(B_1 - B_0)\sqrt{1^2 - y^2}}\left[\frac{\sqrt{1-y^2}-1}{y}\right]^{|n|}\right\}, \tag{8.14}$$

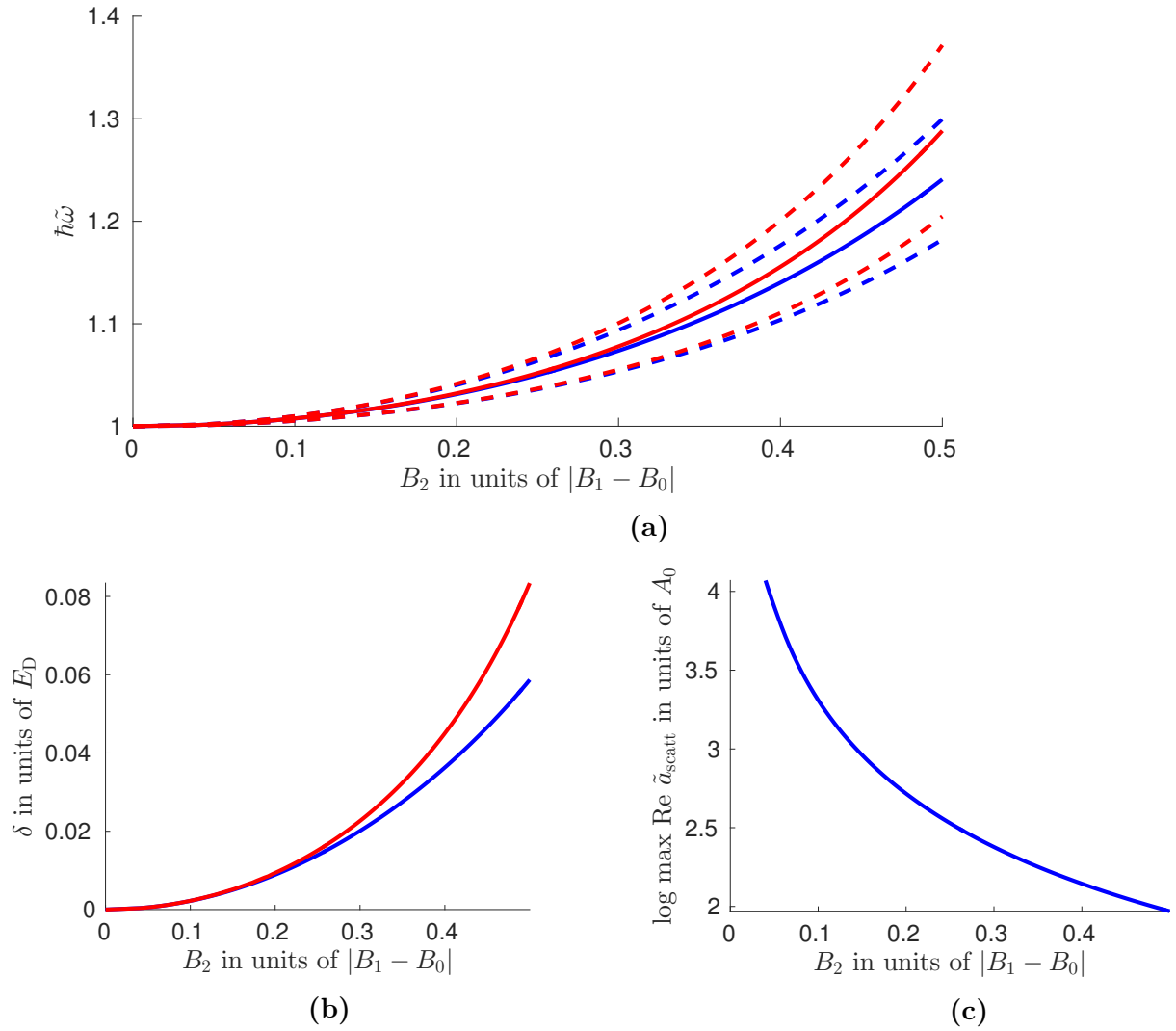

Figure 8.4.: (a): Plot of position and width (dashed lines) of the driven magnetic Feshbach resonance in dependency of the ac-magnetic field B_2. In blue the results, where the maximal considered Fourier component of the potential is $m_1 = 10$, are shown, while in red we consider $m_1 = 1$. **(b)**: Dependency of the width δ of the resonance on the ac-magnetic field B_2 **(c)**: Maximal enhancement of elastic scattering $\max \mathrm{Re}\, a_{\mathrm{scatt}} = \frac{1}{2\gamma}$ over the ac-magnetic field B_2. All plots have been done with $\Delta = -2(B_1 - B_0)$, while $B_1 - B_0 < 0$.

while we introduced

$$y = \frac{B_2}{B_1 - B_0}. \tag{8.15}$$

Its structure reveals that A_n drops polynomially with increasing Fourier index n in the case of $|y| < 1$ and the truncation method defined in Section 8.1 is applicable in this case. As a result we plot in Panel **(a)** of Figure 8.4 in blue position and width of the resonance with largest frequency over the strength of the ac-magnetic field B_2. It can be seen that both resonance position and

width grow with the strength of the ac-magnetic field B_2. This is also the case for the results of a calculation considering only one Fourier mode and can thus be explained qualitatively with the findings of Subsection 7.5.2. The differences of both results can be understood by the results of Section 8.2, as the higher Fourier components increase with larger y. In Panel **(c)** we show that the maximal enhancement of the real part of the time-averaged scattering amplitude decreases with the ac-magnetic field B_2. It is infinite if only one Fourier channel of the potential is considered. In the consideration of higher harmonics it becomes infinitely large only in the case of $B_2 = 0$, while the width vanishes at $B_2 = 0$. This effect might be important for experiments, where a large width and a large enhancement of scattering are favourable. We see in Figure 8.4 that the maximal enhancement of scattering decreases with the ac-magnetic field B_2, while the width increases. Therefore in practice one has to do a trade-off between both quantities and might chose a value of B_2, which allows a notable enhancement of scattering while the width is not too small.

8.4. Frequency and Length Scale for Scattering of Ultracold Atoms

At the end of this Chapter we give an overview of the frequency and length scales occurring in a driven magnetic Feshbach resonance in the case of bosonic ^{85}Rb and ^{133}Cs atoms. For ^{85}Rb we specialise on the resonance at $B_0 = 155.04$ G with the width $\Delta = 10.7$ G and a background scattering length of $a_{\mathrm{bg}} = -443\ a_{\mathrm{Bohr}}$ [102]. For ^{133}Cs we consider the resonance with $B_0 = 547$ G, $\Delta = 7.5$ G and $a_{\mathrm{bg}} = 2500\ a_{\mathrm{bohr}}$ [38]. As all of these resonances are so-called entrance channel dominated [38], the contact potential is a valid approximation of the actual inter-atomic interaction over a wide range of magnetic fields within the width of the magnetic Feshbach resonance. The frequency scale of the driving induced scattering resonance, as displayed in Figure 8.4 **(a)**, is given by the dimer energy divided by $\hbar$, while the length scale is given by the zeroth Fourier component A_0 of the driven contact potential. Therefore Figure 8.5 can be used in order to convert the dimensionless y-axis of Figure 8.4 into physical units in order to estimate the value of the frequency or the field strength, which has to be applied in order to investigate the scattering resonances. In Figure 8.5 we calculate the dimer energy by

$$E_{\mathrm{D}} = \frac{\hbar^2}{2\mu} \frac{1}{[A_0(B_2 = 0)]^2}, \tag{8.16}$$

where μ denotes the reduced mass and $A_0(B_2 = 0)$ is calculated with equation (8.14). Panel **(a)** of Figure 8.5 shows that the dimer energy of the considered Rb resonance lies in the MHz range and increases if $|B_1 - B_0|$ increases. Due to equation (6.5) the results are only valid for driving frequencies below the energy scale of the potential, which is for ^{85}Rb given by the van der Waals energy $E_{\mathrm{vdW}} \approx 6$ MHz [38]. This is indicated in Figure 8.5 by the red dashed line and reveals that this approximation is only valid for small deviations of B_1 from B_0. In combination with Figure 8.4 **(b)** this shows that the width of the resonance lies in the regime of 100 kHz. For ^{133}Cs the situa-

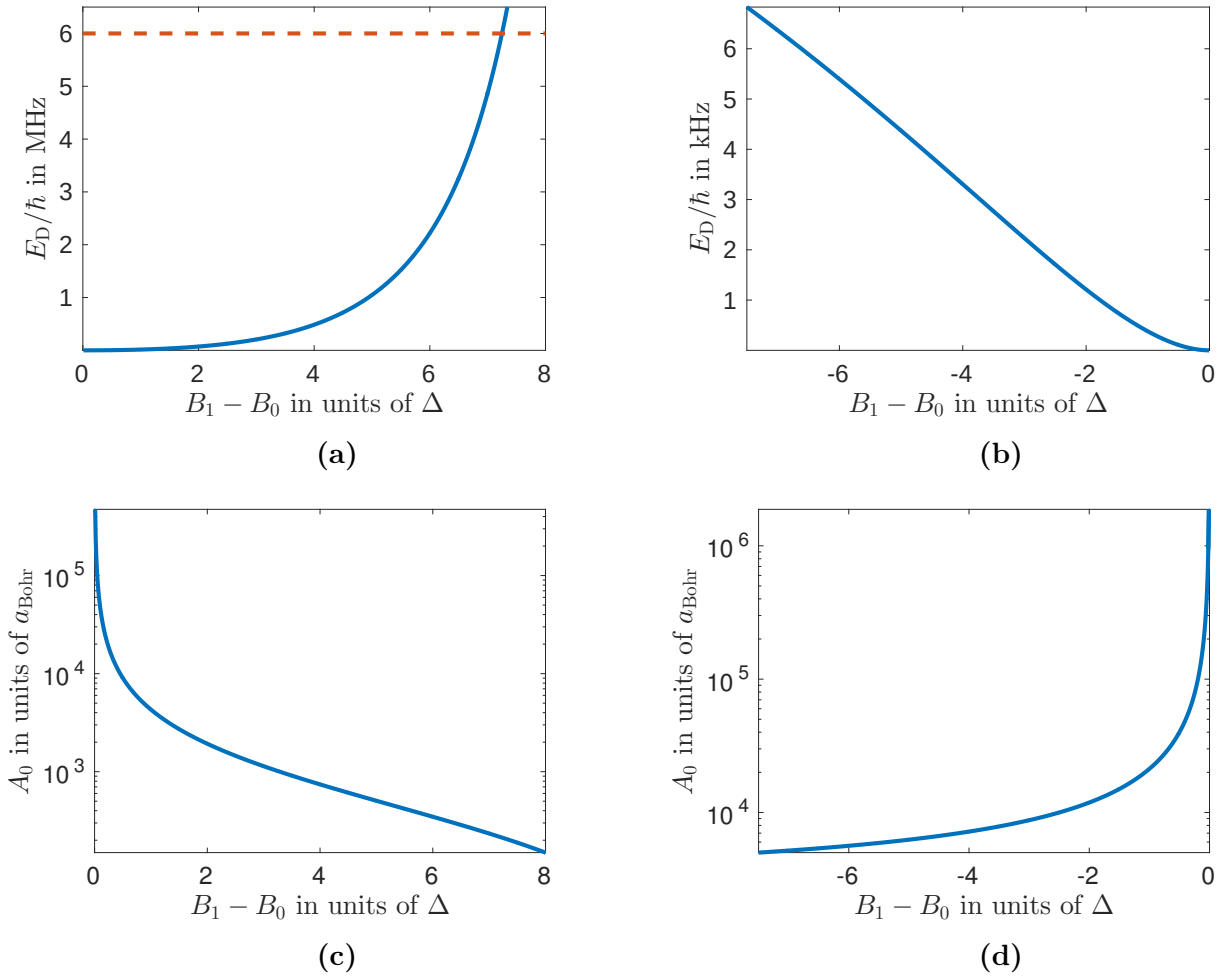

Figure 8.5.: **(a)**: Plot of the dimer energy E_D (blue line) and the van der Waals energy scale (dashed red line) for ^{85}Rb
(b): Plot of the dimer energy E_D for ^{133}Cs
(c): Plot of $A_0(B_2 = 0)$ in Bohr radii a_{Bohr} for ^{85}Rb
(b): Plot of $A_0(B_2 = 0)$ in Bohr radii a_{Bohr} for ^{133}Cs

tion is different, as the dimer energy lies in the kHz regime and thus way below the van der Waals energy of $E_{vdW} = 2.666$ MHz [38]. The width of the resonance is of the order of 100 Hz. Panel **(c)** and **(d)** can be used to express the maximal enhancement of scattering shown in Figure 8.4 **(c)** in Bohr radii. In order to validate the approximation of $\tilde{\epsilon} = 0$, the dimer energy has to be larger than the temperature of the Bose-Einstein condensate. Assuming a temperature of $T \approx 10^{-9}$ nK, we arrive at a frequency scale of 100 Hz. If this condition is not fulfilled, the maximal enhancement of elastic scattering is lower due to the finite energy $\tilde{\epsilon}$ as discussed in Subsection 7.5.1.

9. Conclusion and Outlook

In Section 9.1 we summarise the most important findings of our work and give concluding remarks, while Section 9.2 is dedicated to the Outlook.

9.1. Conclusion

The tuning of the interaction strength enables a rich amount of experimental settings, especially in the case of ultracold quantum gases [1, 2, 38]. Due to low kinetic energies s-wave scattering is dominant and the interaction strength can be described by a single parameter, named scattering length. Magnetic Feshbach resonances provide a common tool of controlling the scattering length experimentally. A limiting factor of their application is that they occur only at certain characteristic magnetic field strengths. Recent works [3–5] showed that periodic driving can enhance the scattering of quantum particles in a dramatic way, opening new possibilities of controlling the scattering length.

This thesis investigated the two-body problem with a time-periodic interaction potential. Based on Floquet theory the Floquet-partial wave expansion was derived in Chapter 5 as a generalisation of scattering theory which is able to deal with time-periodic interaction potentials. It was used to calculate time-averaged scattering amplitudes, cross sections and Floquet states.

We applied in Chapter 6 the Floquet-partial wave expansion to a sinusoidally driven contact potential, which describes the two-body interactions of quantum particles in the regime of s-wave scattering. Due to the simple structure of the potential the time-dependent scattering problem (6.11) was mapped to the recursion relation (6.37), which connects different Fourier-components of its steady-state wave function. The solution of the recursion was used to calculate the time-averaged scattering amplitude. Although this recursion is non-linear in the Fourier index, it can be solved numerically for arbitrary driving frequencies. In addition we found an analytic solution for high and low driving frequencies. At low frequencies the resulting Floquet state follows adiabatically the time-evolution of the driven potential.

The main result of our investigation, displayed in Chapter 7, concerned the observation of driving induced scattering resonances, which occur along lines in the parameter space of driving strength and frequency. In the vicinity of these resonances scattering is dramatically enhanced, which allows the tuning of the time-averaged scattering amplitude to large positive or negative values. The width of these resonances can be adapted by the driving strength, while the enhancement is controlled by the

driving frequency. It turned out that they are lossless, as no inelastic scattering due to absorption of energy quanta from the drive field is present in their vicinity.

The occurrence of these scattering resonances was related to the emergence of bound states in the continuum and explained in Section 7.2 as Fano-Feshbach resonances involving these bound states located in a Floquet side-band. With this finding we were able to calculate the resonance position for arbitrary driving strength and frequency. For weak driving a resonance occurs, if the frequency matches with a transition between the scattering state and the universal dimer state of the contact potential. We spotted that these resonances only emerge if the driving frequency is larger than the particle energy divided by $\hbar$.

The time-averaged scattering amplitude can be approximately described by simple formulas (7.43) and (7.54), where equation (7.54) was derived in Section 7.4.2 from scattering by a two-channel model and approximates the numerical data slightly better than (7.43). These formulas were used in Section 7.5 in order to extract position and width of scattering resonances for almost arbitrary driving strengths. Their width increases with the driving strength and vanishes in the limit of small driving. In addition we found in Section 7.6 a Kramers-Kronig like relation between real and imaginary part of the time-averaged scattering amplitude, which is also fulfilled by the approximative formulas.

A possible experimental realisation of this theory is the periodically driven magnetic Feshbach resonance [3]. In order to describe this setting with a better accuracy, the scattering by a contact potential with a more general time-periodic driving was investigated in Chapter 8. In this case inelastic scattering is present in the vicinity of the resonance, but by tuning the frequency slightly away from it, elastic scattering can be still enhanced without suffering a large amount of losses. We were able to calculate position and width of the periodically driven magnetic Feshbach resonance in a wide range of driving strengths.

In summary we conclude that it is possible to tune the scattering length and therefore the interaction strength of particles by periodic driving. This driving induced scattering resonance has the benefit of being almost lossless and tunable solely by the driving parameters. This allows a larger experimental flexibility, as unlike in the case of a magnetic Feshbach resonance the magnetic field strength can be set relative far away from the resonance without loosing the enhancement of scattering. In comparison to an optical Feshbach resonance it has the advantage of being almost lossless. In addition, it might be applied to tune the interaction in ultracold gas experiments, where no magnetic or optical Feshbach resonance is available.

9.2. Outlook

Although the contact potential is a simple model of the more complicated inter-atomic interaction potential, its study in a driven case is highly non-trivial. Despite the fact that a quite general form of the solution is given in this thesis, several points remain unsolved.

At first we want to mention, that it would be of large interest, if also in the case of a periodically driven scattering resonance general formulas for calculating position and width like equations (3.8) and (3.9), which are applicable for magnetic Feshbach resonances, exist. Such formulas would give a clear definition and allow a calculation of these quantities without relying on a fitting procedure or being restricted to approximative solutions.

Secondly, a detailed study of the case, where the driving amplitude a_1 extends the value of the time-averaged one, has not been done. It would be of interest, as it can be reached in experimental setups [2]. Our investigations revealed that scattering resonances only exist in the case of a positive scattering length of the contact interaction, as their emergence is connected with the existence of a bound dimer state. In the case of $a_1 > \bar{a}$ this dimer state is only present in a part of the driving period. Therefore it would be interesting, if the occurrence of scattering resonances is also possible in this case or if the partial absence of the bound state destroys the possibility of the system to enhance elastic scattering. In order to do this investigation it would be advantageous to find a formalism, where $1/a$ is treated as a smallness parameter or use a different scattering potential.

We only dealed with two body physics, but experimental realisations of Feshbach resonances are also limited by losses due to three-body collisions. Due to their experimental relevance and based on [4] it would be interesting to investigate the occurrence of three body losses in the case of a periodically driven inter-particle interaction. Also the investigation of higher partial waves in Floquet scattering would be interesting.

A natural extension of the findings of Chapter 8 would be the investigation of more sophisticated driving schemes. This includes the case of applying a general time-periodic driving, like a sawtooth, on a periodically driven magnetic Feshbach resonance. A more complicated setting would include the driving of the system with two incommensurate frequencies.

As we observed driving induced scattering resonances by using the methods of theoretical physics, an interesting next step would be implementation of these resonances in an experimental setup. In the following we discuss two possible fields of application for driving induced Feshbach resonances and give an introduction in wave-guide arrays, where Floquet physics can be made visible directly.

9.2.1. Periodically Driven Optical Feshbach Resonance

Optical Feshbach resonances are induced by laser light, which is near resonant to a transition between a scattering state and a molecular bound state. As the bound state is usually not a ground state, it decays spontaneously. This decay limits the applicability of the optical Feshbach resonance, as it results in strong losses in its vicinity. As shown in Figure 9.1, there are processes which lead to a limited amount of elastic scattering, as the shift of the scattering length is proportional to the displayed interaction shift, which can be enhanced up to 30%. In order to get a larger enhancement of elastic scattering we suggest to apply the driving induced Feshbach resonance in this setting. A feasible protocol would locate the bias of the periodic drive at the side of the optical Feshbach resonance, where the losses are negligible, but the rate of elastic scattering can be changed noticeably.

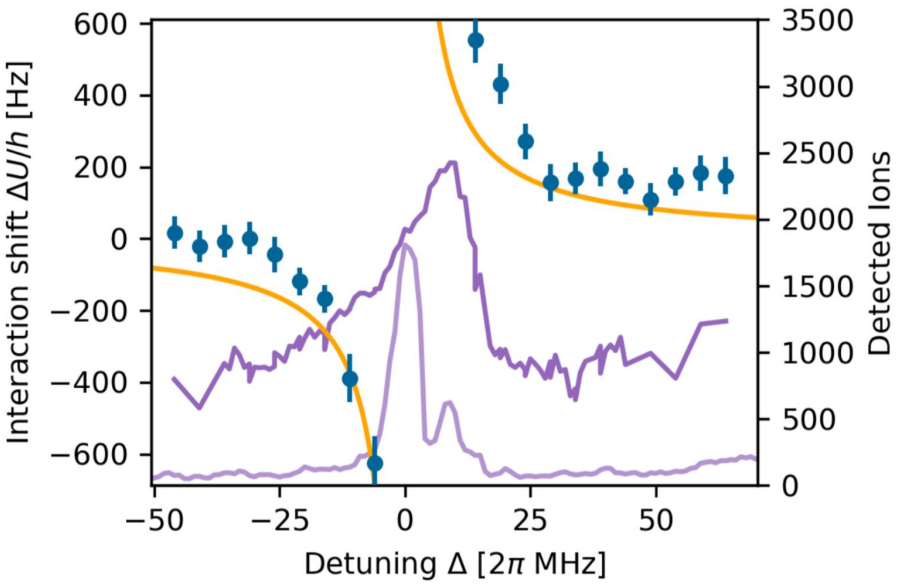

Figure 9.1.: Plot of an optical Feshbach resonance in ultra long-range Rydberg molecules. Blue dots represent the interaction shift over the detuning of the laser, which created the optical Feshbach resonance. The orange curve has been calculated using an approximate theoretical model. The purple curves are ion signals used for measuring the resonance structure. The Figure was created by Thomas et al. [69], where a detailed explanation of the emerging quantities is found.

In this region it could be possible to enhance the scattering amplitude without suffering a large amount of losses. The question is, if it is possible to minimise both losses from the optical Feshbach resonance and the driving induced one in such a way that the method is applicable. Equation (3.14) suggests that driving scheme can be implemented by either altering the intensity or the detuning of the laser used for creating the optical Feshbach resonance periodically.

This possible implementation of the driving induced Feshbach resonance is also of theoretical interest, as it combines the field of periodic driving with the investigation of dissipative systems. In order to deal with it correctly, losses have to be included in the formalism. A straight-forward way of obtaining this theoretically is the extension of Floquet-scattering theory to non-hermitian potentials. The investigation of scattering by a non-hermitian potential in an one-dimensional tight-binding chain [103] revealed fascinating results as the complete invisibility of the potential in scattering configurations. This effect brings up the question, how dissipation can change or even suppress resonant features and therefore dramatically redraft the behaviour of the driven system. As the simplest non-trivial scattering potential we suggest the contact interaction with a complex scattering length. A second compelling and very general approach would be the scattering by a square well potential with a complex potential strength. As in the case of a driven hermitian square well potential there exists a solution in a closed form [80], it is the hope that this might be extended to a driven-dissipative case in an intuitive manner.

9.2.2. Scattering in Quantum Gases with Internal Degree of Freedom

The development of the optical dipole trap [104] enabled to trap Bose-Einstein condensates in different hyperfine states and therefore with a spin-like internal degree of freedom. These spinor Bose-Einstein condensates possess a rich phase diagram especially in the presence of an external magnetic field [105]. For example, by changing the magnetic field across a critical value, one is able to observe a quantum phase transition to a ferromagnetic phase [106]. Magnetic Feshbach resonances are limited for the control of the interaction strength in these systems, as they cannot be tuned independently from the magnetic field and only occur at restricted field strengths. The driving induced scattering resonance can be induced in a wide range of magnetic field strengths and the enhancement of scattering is controlled by use of the driving frequency and strength. It would allow the enhancement of scattering while simultaneously tuning the magnetic properties of the spinor gas by changing the magnetic field.

One specific example, on which the driving induced scattering resonance can be applied, is the control of scattering rates of spin impurities with a bath. In a recent experiment [107] impurities of neutral ^{133}Cs atoms with total internal angular momentum of $F_\mathrm{i} = 3$ are immersed into a Bose-Einstein condensate of ^{87}Rb atoms with $F_\mathrm{b} = 1$ and are used to probe properties of the condensate. For example it is possible to detect the hyperfine-Zeeman level of the condensate by investigating spin-exchange dynamics between impurity and bath. Additionally, this setup enables the observation of coherent dynamics by preparing the impurity in a quantum superposition state. The de-phasing of the dynamics is influenced by the actual value of the elastic scattering length. Theoretical and experimental investigations indicate the presence of a magnetic Feshbach resonance [108], which allows to enhance both elastic and spin-exchange scattering rates for collisions between impurity and bath. In practice the scattering can only be enhanced for collisions in one Zeeman level, because the resonances for different levels are located at different magnetic field strengths.

This restriction can be overcome by the application of the driving induced scattering resonance [108]. If possible, one has to choose a bias magnetic field B_1 in a region, where all magnetic resonances provide a positive scattering length. By applying a sinusoidally modulated magnetic field with strength B_2 one would be able to create a driving induced scattering resonance in all Zeeman levels simultaneously. This would enhance scattering in total and fasten up the interaction process between impurity and bath, which would be a benefit in investigations probing the Bose-Einstein condensate in a non-equilibrium state.

In order to model the situation in a better way, the spin-like internal degree of freedom has to be included in the interaction potential. The most basic way to do this is to use the contact potential as spatial degree of freedom and add an internal matrix structure, which couples different channels of the wave function [105, 109]. This can be expressed using the spin operators of the scatterers [109]. It would be interesting to observe how this additional degree of freedom and the matrix structure of the potential is able to alter the properties of scattering resonances or if it can even be used in order to create new ones. Another direction would be the investigation, if periodic driving can be used in order to control collisions with a spin-exchange efficiently. This would make it possible to prepare or conserve a favoured hyperfine state in a system, which is interacting with

its environment.

9.2.3. Driven Impurities in Coupled Wave-Guide Arrays

Another path of further research goes back to one-dimensional systems with periodically driven impurities. A profound experimental setup for investigating single particle dynamics in those systems are dielectric [110, 111] and plasmonic [112] wave-guide arrays. The paraxial Helmholtz equation [110]

$$i\frac{\partial}{\partial z}\psi(x,y,z) = -\frac{1}{2k_{\mathrm{wg}}}\left[\frac{\partial^2}{\partial x^2} + \frac{\partial^2}{\partial y^2} + V(x,y)\right]\psi(x,y,z) \tag{9.1}$$

describes the propagation of light in these wave-guides and is mathematically equivalent to the Schrödinger equation [113]. Therefore the behaviour of light can be used in order to mimic quantum mechanics. As it can be seen in equation (9.1), time in quantum mechanics corresponds to the propagation direction of light in the wave-guides, which is here considered as z-direction, the mass is given by the wave vector in the wave-guide k_{wg} and the wave function ψ is given by the light field. A non-vanishing potential can be induced by tuning the refractive index.

If the wave-guides are arranged in a lattice in x or y direction, the dynamics of light in such an array is governed by a lattice Hamiltonian similar to the tight-binding model [114]. The hopping constant J in this case is determined by the overlap of the evanescent light-modes in the wave-guides. Figure 9.2 sketches a possible experimental setup, which consists of a tight-binding model with a periodically modulated site.

As wave-guide arrays are accessible and allow tuning of parameters, they are suitable for the investigation of defect states [110] and the realisation of topological models. A recently created experimental setup [115] deals with the stability of topological protected edge states under periodic modulation. The experimental situation is modelled by two one-dimensional Su-Schrieffer-Heeger chains [116], which are coupled via a central site acting as an impurity. A sketch of this setting is done in Figure 9.3.

The Su-Schrieffer-Heeger model consist of a chain with staggered hopping amplitudes and as a model with a non-trivial topology it possesses topological protected edge states. A band structure of the experimentally realised Hamiltonian is shown in Figure 9.4. It consists of two bulk bands related to states with finite momentum and a bound edge state emerging at the central site.

In order to probe the robustness of the system against local perturbations, the position of the wave-guide corresponding to the central site is periodically modulated perpendicular or parallel to the direction of the SSH-chain. As the distance to the neighbouring lattice sites is modulated periodically, this results in a periodically modulated hopping amplitude to and from the impurity site. The curvature of the wave-guide can be related to a time-dependent on-site potential [115]. As an initial condition light is only located in this impurity site. The question is, if the edge state remains localised in the presence of periodic modulation or if a transition to the bulk band is occurring.

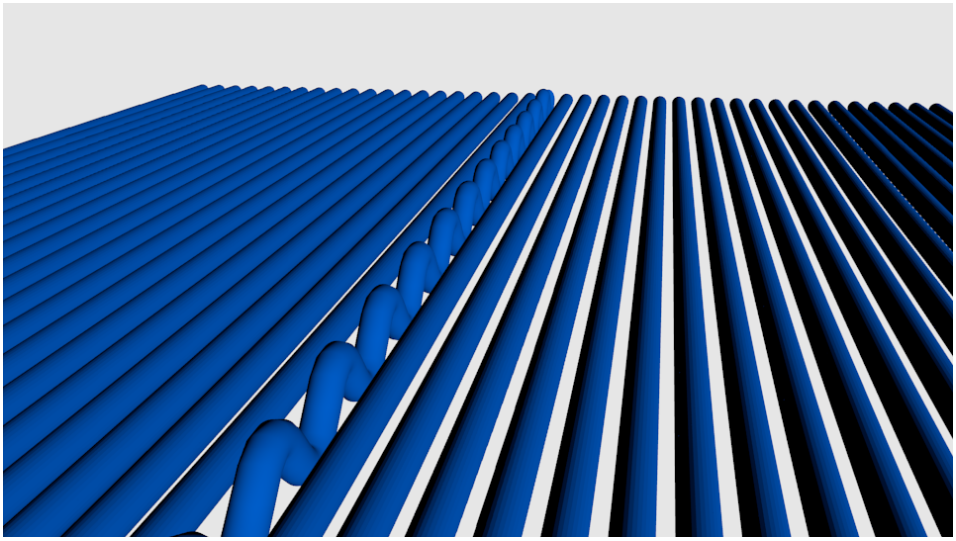

Figure 9.2.: Possible experimental setup of dielectric wave-guide arrays realising an one dimensional tight-binding model. All arrays are oriented in z-direction, which corresponds to the time in quantum mechanics, while the lattice is formed in x-direction. As an impurity one wave-guide is periodically modulated perpendicular to the direction of the lattice, inducing a time-dependend term in the tight-binding model. The picture was created by C. Jörg [115].

In order to complement the experimental results [117], the corresponding time-periodic Schrödinger equation is solved using Floquet theory. The full time-evolution of the system at arbitrary driving strength can be determined by diagonalising the Floquet Hamiltonian (4.10), which yields Floquet modes and energies. With Floquet theory we can calculate the probability, that a state with momentum k and energy E is occupied.

In addition it would be intriguing to invert the setting by looking at scattering by the driven impurity in a model with a topological background and investigate the influence of the periodically modulated hopping amplitude on the scattering process. A goal of this research direction would be to find a relation between the excitation of the defect state and the transmission amplitude through the driven barrier.

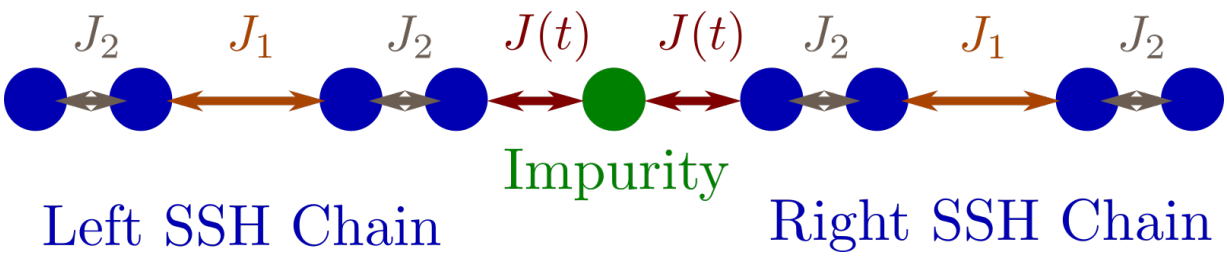

Figure 9.3.: Sketch of the theoretical model being realised in experiment. It consists of two SSH chains, which have staggered hopping amplitudes J_1 and J_2, and are connected by the impurity site. The hopping $J(t)$ to and from the impurity is periodically modulated.

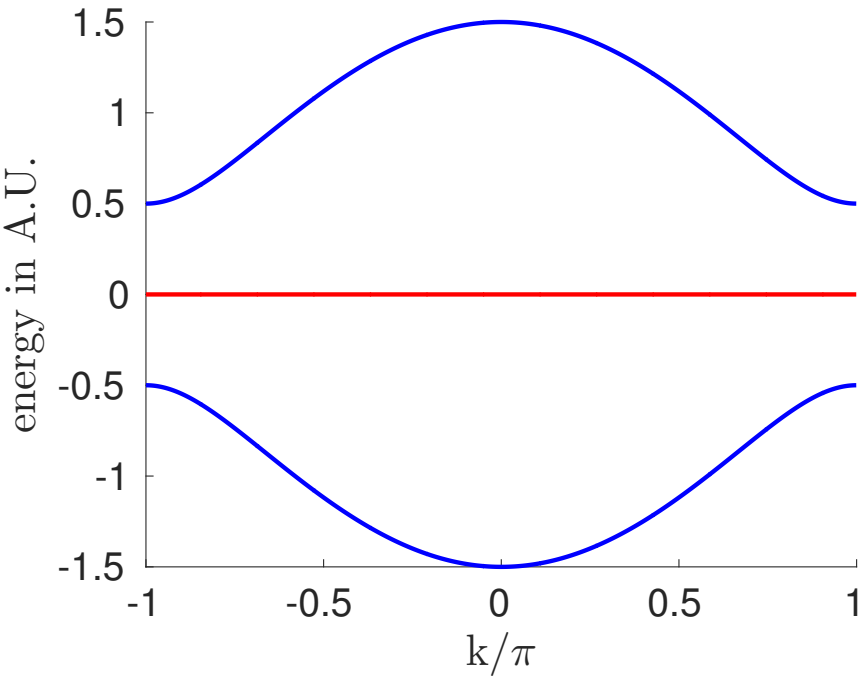

Figure 9.4.: Band structure of the SSH model. In blue the dispersion of the bulk bands is drawn, while the energy of the defect state is visualised as a straight line at an energy of zero.

A. Contact Potential

The idea of the contact potential, also named pseudo potential, is to approximate a complicated potential by a simple one. This approximation is valid in the case of scattering with low energies, where the de-Broglie wavelength is much larger than the range of the actual potential and the potential is effectively present only in the origin. This idea has been discussed in literature of earlier days of quantum mechanics [118, 119] and considered as a simplification of the scattering by a hard-sphere potential. We present a derivation in the case of s-wave scattering [55]. Starting point is the wave function solving the scattering by a hard-sphere potential

$$R_0(r) = A_0[j_0(kr) - \tan(\delta_0) y_0(kr)], \tag{A.1}$$

which has been introduced in Section 2.3. As the contact potential is designed to act on the wave function only in the origin, we extend equation (A.1) to be also valid inside the hard sphere and integrate the radial Schrödinger equation (2.9) over a sphere of radius r_0 around the origin using Gauss theorem

$$\int_{B_{r_0}(0)} d^3r [\Delta + k^2] R_0(r) = \int_{\partial B_{r_0}(0)} \mathbf{dA} \boldsymbol{\nabla} R_0(r_0) + \int_{B_{r_0}(0)} d^3r \; k^2 R_0(r) \tag{A.2}$$

In the limit of $r_0 \to 0$ the last term vanishes, while the first is evaluated by using $\mathbf{dA} = d\Omega r_0^2 \hat{\mathbf{e}}_r$ and $\boldsymbol{\nabla} R_0(r_0) \cdot \hat{\mathbf{e}}_r = \partial_r R_0(r)\big|_{r=r_0}$ to $-\frac{4\pi}{k}\tan(\delta_0) A_0$. The amplitude A_0 can be rewritten as the operator $\lim_{r\to 0} \frac{\partial}{\partial r} r R_0(r)$, if $R_0(r)$ is of the Form (A.1). The identity $1 = \int d^3r \delta^3(r)$ is used in order to drop the integral

$$[\Delta + k^2 + \frac{4\pi}{k \cot(\delta_0)} \delta^3(\mathbf{r}) \frac{\partial}{\partial r} r] R_0(r) = 0. \tag{A.3}$$

If equation (A.3) is compared to the radial Schrödinger equation, the contact potential can be identified to

$$V_{\text{contact}}(r) = \frac{-2\pi\hbar^2}{\mu k \cot(\delta_0)} \delta^3(\mathbf{r}) \frac{\partial}{\partial r} r, \tag{A.4}$$

with μ as the reduced mass. For the case of scattering with low energies the scattering length a (2.20) can be used to further simplify the potential to

$$V_{\text{contact}}(r) = \frac{2\pi\hbar^2 a}{\mu} \delta^3(\mathbf{r}) \frac{\partial}{\partial r} r. \tag{A.5}$$

In the following we discuss some properties of the contact potential: At first, the difference to a

bare delta-function potential is made clear. Therefore the wave function is expressed by a Laurent series

$$R(r) = \sum_{n=-\infty}^{\infty} c_n r^n. \tag{A.6}$$

The evaluation of the delta function integral, using equation (6.6), leads to the result

$$\int_0^\infty dr\delta(r)R(r) = \frac{c_0}{2} + \frac{1}{2}\underbrace{\sum_{n=-\infty}^{-1} c_n r^n\big|_{r=0}}_{\text{divergent terms}}. \tag{A.7}$$

The divergent terms only disappear, if the coefficients c_n vanish for all $n \leq -1$. The same calculation is also done in the case of the contact potential

$$\int_{-\infty}^\infty dr\delta(r)\frac{\partial}{\partial r}[rR(r)] = \int_{-\infty}^\infty dr\delta(r)\sum_{n=-\infty}^{\infty} c_n(n+1)r^n = \frac{c_0}{2} + \frac{1}{2}\underbrace{\sum_{n=-\infty}^{-2} c_n r^n\big|_{r=0}}_{\text{divergent terms}}. \tag{A.8}$$

If there are no divergent terms in the test function, the result of both calculations is the same. But if only divergent terms of the order $\frac{1}{r}$ are present, they will not appear in the contact potential calculation, but in the one using the delta function. This vanishing of divergences is necessary in order to obtain useful scattering properties in case of s-wave scattering by a short range interaction, as the ansatz functions (6.12) posses an $1/r$ divergence in the origin.

A.1. Scattering by a Contact Potential

In the following we derive the scattering properties of the pseudo potential by assuming a scattering state of the form

$$R_0(r) = \frac{\sin(kr)}{kr} + f\frac{e^{ikr}}{r} \tag{A.9}$$

and using the formalism introduced above. The first part of (A.9) is the s-wave part of the plane wave, the second the scattered spherical wave. Equation (A.9) solves the free radial Schrödinger equation for each $r \neq 0$. In order to evaluate the Dirac delta-function, an integration on a sphere of radius r_0 around the origin similar to (A.2) is done

$$\int_{B_{r_0}(0)} d\Omega dr\ r^2[\Delta R_0(r) + k^2 R_0(r)] + 4\pi a\delta^3(\mathbf{r})[\frac{\partial}{\partial r}rR_0(r)] \tag{A.10}$$

Inserting (A.9) into (A.10) yields the equation $-f - a(1 + ikf) = 0$. From this the scattering amplitude f can be derived to

$$f = \frac{-1}{\frac{1}{a} + ik}. \tag{A.11}$$

A.2. Bound State

At last, we mention that the contact potential possesses a bound state in the case of positive scattering length a. This can be found out by solving the Schrödinger equation

$$\left[\Delta - 4\pi a \delta^3(\mathbf{r}) \frac{\partial}{\partial r} r\right] \psi(\mathbf{r}) = \frac{2m}{\hbar^2} E \psi(\mathbf{r}) \tag{A.12}$$

with the ansatz

$$\psi(\mathbf{r}) = C e^{-\kappa |\mathbf{r}|}. \tag{A.13}$$

Similar to (A.10) an integration around the origin leads to the result $\kappa = \frac{1}{a}$, which inserted into equation (A.12) for $r \neq 0$ yields the bound state energy of $E = -E_\mathrm{D}$. Here we introduced the dimer energy

$$E_\mathrm{D} = \frac{\hbar^2}{2\mu} \frac{1}{a^2}. \tag{A.14}$$

We followed [3] and named this bound state energy dimer energy, as its wave function corresponds to a bound dimer state.

B. Kramers-Kronig Relations for Anti-Causal Susceptibilities

In literature [120–122] Kramers-Kronig relations are derived for causal response functions like the electric susceptibility $\chi(t)$, which describes the material property how the polarisation $P(t)$ is influenced by an external field $E(t)$

$$P(t) = \int_{-\infty}^{\infty} dt' \chi(t - t') E(t'). \tag{B.1}$$

In several references [4, 75, 79, 80] and this thesis the driving frequency dependent scattering length obeys relations, which will now to be derived as the Kramers-Kronig relations for anti-causal susceptibilities. As the driving frequency dependent scattering length cannot be interpreted as a susceptibility, there is no violation of causality if the Kramers-Kronig relations are not fulfilled in this case. In order to derive the Kramers-Kronig relations in the case of an anti-causal susceptibility $\chi(t)$ and its Fourier-transform $\tilde{\chi}(\omega) = \int_{-\infty}^{\infty} dt\ \chi(t) e^{i\omega t}$, we first have to discuss about the requirements. Mentioned first and most important is the anti-causality of $\chi(t)$ in the sense of (B.1), which reads

$$\chi(t) = 0\ \forall t > 0. \tag{B.2}$$

Additionally $\chi(t)$ and its Fourier transform $\tilde{\chi}(\omega)$ have to fulfil certain convergence conditions:

$$\lim_{t \to -\infty} \chi(t) = 0 \text{ faster than } \frac{1}{t}, \tag{B.3}$$

$$\lim_{\omega \to \infty} \tilde{\chi}(\omega) = 0 \text{ faster than } \frac{1}{\omega}. \tag{B.4}$$

With (B.1) the Fourier transform can be simplified to $\tilde{\chi}(\omega) = \int_{-\infty}^{0} dt \chi(t) e^{i\omega t}$ and generalised to complex omega. For $\mathrm{Im}\,\omega < 0$ the Fourier transform $\tilde{\chi}(\omega)$ exists, as the negative imaginary frequency and the condition (B.3) ensures the convergence of the Fourier transform. This argument can be generalised to all derivatives of $\tilde{\chi}(\omega)$ and therefore it is analytic in the lower half plane. With the residue theorem the integral along the path shown in Figure B.1 must vanish

$$\oint d\omega \frac{\tilde{\chi}(\omega)}{\omega - \omega_0} = 0, \tag{B.5}$$

as no poles of $\tilde{\chi}(\omega)$ lie inside. By taking the radius of the larger half-sphere to infinity, only the parts of the integral near the real axis remain

$$\int_{\mathbb{R} \setminus \partial B_\gamma(\omega)} d\omega \frac{\tilde{\chi}(\omega)}{\omega - \omega_0} + \frac{1}{2} \oint_{\partial B_\gamma(\omega)} d\omega \frac{\tilde{\chi}(\omega)}{\omega - \omega_0} = 0. \tag{B.6}$$

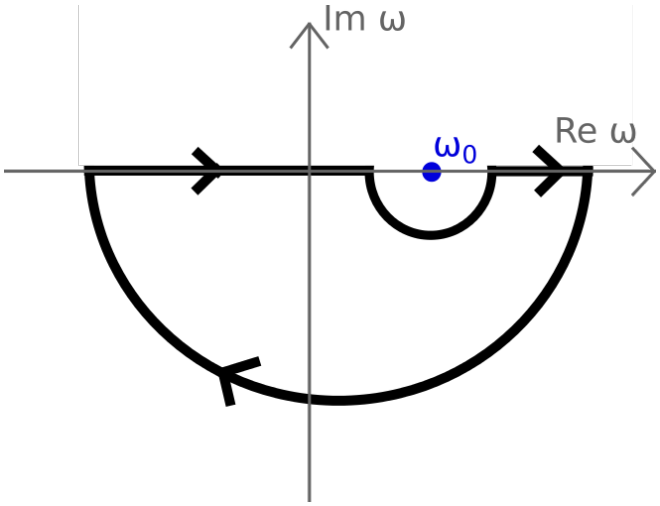

Figure B.1.: Plot of integration path used to derive the Kramers-Kronig relations in the case of an anti-causal susceptibility. The arrows along the line indicate the integration direction.

Note that the factor 1/2 stems from only going half the small circle around ω_0 in the integration path in Figure B.1. With the residue theorem the last term simplifies to $\pi i \chi(\omega_0)$. Taking the limit of vanishing γ and rewriting equation (B.6) in real and imaginary part, we arrive at Kramers-Kronig relations for an anti-causal susceptibility:

$$\text{Re } \tilde{\chi}(\omega_0) = -\frac{1}{\pi}\mathbb{P}\int_{-\infty}^{\infty} d\omega \frac{\text{Im } \tilde{\chi}(\omega)}{\omega - \omega_0} \tag{B.7}$$

$$\text{Im } \tilde{\chi}(\omega_0) = \frac{1}{\pi}\mathbb{P}\int_{-\infty}^{\infty} d\omega \frac{\text{Re } \tilde{\chi}(\omega)}{\omega - \omega_0}. \tag{B.8}$$

We introduce the principal value integral as

$$\mathbb{P}\int_{-\infty}^{\infty} dx \frac{\tilde{\chi}(x)}{x - x_0} = \lim_{\gamma \to 0} \left(\int_{-\infty}^{x_0 - \gamma} dx + \int_{x_0 + \gamma}^{\infty} dx \right) \frac{\tilde{\chi}(x)}{x - x_0}. \tag{B.9}$$

We name these equations as anti-Kramers Kronig relations. They equal the Kramers-Kronig relations for causal susceptibilities [120] except of the change of a minus sign in front of the principal value integrals.

C. Derivation of Scattering Amplitude of a Simple Coupled-Channel Model

In this Appendix we calculate the scattering of a two-component wave function

$$\psi(r) = \begin{pmatrix} \psi_0(r) \\ \psi_1(r) \end{pmatrix} \tag{C.1}$$

by the coupled-channel Hamilton operator (7.50). The radial Schrödinger equation $H(r)\psi(r) = \mathcal{E}\psi(r)$ for the coupled-channel scattering problem reads

$$\left[-\frac{1}{r^2}\frac{\partial}{\partial r} r^2 \frac{\partial}{\partial r} + \frac{2a_0}{r^2}\delta(r)\frac{\partial}{\partial r} r \right] \psi_0(r) + \frac{2a_{\mathrm{WW}}}{r^2}\delta(r)\frac{\partial}{\partial r} r\psi_1(r) = \mathcal{E}\psi_0(r), \tag{C.2}$$

$$\left[-\frac{1}{r^2}\frac{\partial}{\partial r} r^2 \frac{\partial}{\partial r} + \frac{2a_1}{r^2}\delta(r)\frac{\partial}{\partial r} r + v \right] \psi_1(r) + \frac{2a_{\mathrm{WW}}}{r^2}\delta(r)\frac{\partial}{\partial r} r\psi_0(r) = \mathcal{E}\psi_1(r). \tag{C.3}$$

We use as an ansatz

$$\psi_0(r) = e^{i\mathbf{kr}}\big|_{\mathrm{s-wave}} + f\frac{e^{ikr}}{r} = \frac{\sin(kr)}{kr} + f\frac{e^{ikr}}{r} \tag{C.4}$$

in the open channel, which is considered to be channel zero, and

$$\psi_1(r) = C\frac{e^{-\kappa r}}{r} \tag{C.5}$$

in the closed one. The quantity f denotes the s-wave scattering amplitude and C is the normalisation constant of the closed channel wave function.

Inserting both ansatz-wave functions in the respective coupled-channel equations for $r \neq 0$, we obtain the dispersion relation

$$k^2 = \mathcal{E} \tag{C.6}$$

for the free solution ψ_0 and

$$\kappa^2 = v - k^2 \tag{C.7}$$

for the closed channel solution ψ_1. We assume v to be positive and of a strength necessary in order to make ψ_1 a bound state, i.e. $v > k^2$. In order to determine the constants C and f we multiply both equation (C.2) and (C.3) by r^2 and integrate from 0 to a small radius ϵ_r similar to Section 6. At last, we take the limit of vanishing ϵ_r. Equation (C.2) can thus be rewritten as

$$(1 + ika_0)f + a_0 - a_{\mathrm{WW}}\kappa C = 0. \tag{C.8}$$

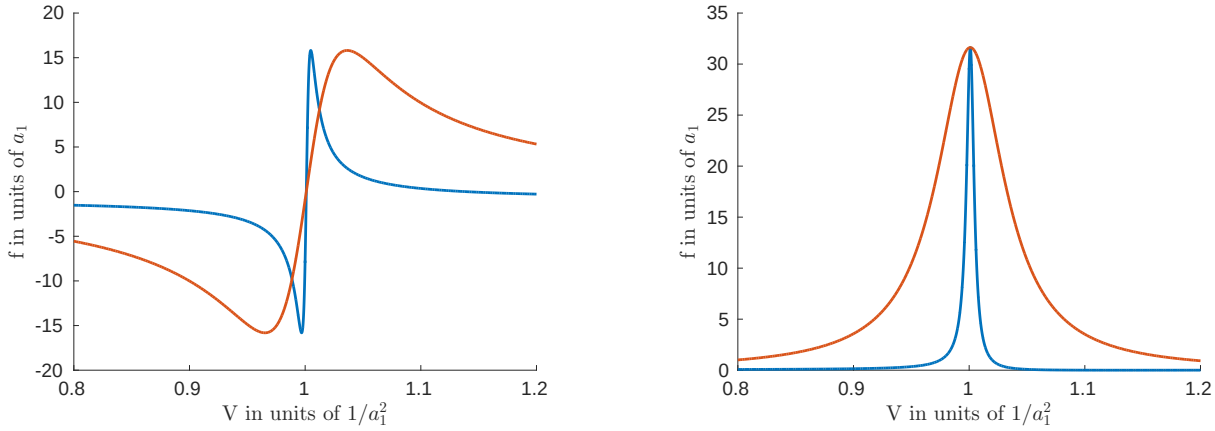

Figure C.1.: Plot of real **(a)** and imaginary **(b)** part of the scattering amplitude f for the case of $a_{\mathrm{WW}} = 0.25a_1$ (blue) and $a_{\mathrm{WW}} = 0.75a_1$ (red), $\mathcal{E} = 10^{-3}/a_1^2$ and $a_0 = a_1$.

With the same argumentation equation (C.3) is simplified to

$$(1 - a_1\kappa)C + a_{\mathrm{WW}}(1 + ikf) = 0. \tag{C.9}$$

These two equations are linear in f and C. The amplitude C is given by

$$C = \frac{a_{\mathrm{WW}}}{a_1\kappa - 1 + ik(a_{\mathrm{WW}}^2\kappa + a_0a_1\kappa - a_0)}, \tag{C.10}$$

while the scattering amplitude f can be written in the form

$$f = \frac{-1}{\frac{1}{a} + ik}. \tag{C.11}$$

Hereby we define the scattering length

$$a = a_0\left(1 + \frac{a_{\mathrm{WW}}^2\kappa/a_0}{1 - a_1\kappa}\right) \tag{C.12}$$

depending on the coupling strength a_{WW} and the offset potential v of the closed channel. The κ dependence of equation (C.12) is similar to the magnetic field dependency of equation (3.12). For $\kappa = 1/a_1$ the scattering length diverges and leads to a resonantly enhanced scattering amplitude of value $f = \frac{i}{k}$. This condition is equivalent to the equality of the energy of the scattered wave in the first channel $\mathcal{E}$ and the energy of the bound state $\mathcal{E}_{\mathrm{bound}} = V - \frac{1}{a_1^2}$ in the second one. Figure C.1 shows the dependence of the scattering amplitude on the offset potential v for different coupling strengths a_{WW}. The width of the resonance increases with growing coupling strength a_{WW}. The shape of the scattering amplitude is similar to the results obtained in the case of the driven scattering problem if one plots it over the driving frequency. Therefore it is suggestive to replace the offset potential v by an integer multiple of the driving frequency $|n|\hbar\tilde{\omega}$ in order to get a formula to fit the two-channel model on the more complicated case of the driven scattering problem

$$-\frac{1}{f}=\frac{1}{a_0}\frac{1-a_1\sqrt{|n|\hbar\tilde{\omega}-\mathcal{E}}}{1-a_1\sqrt{|n|\hbar\tilde{\omega}-\mathcal{E}}+a_{\mathrm{WW}}^2/a_0\sqrt{|n|\hbar\tilde{\omega}-\mathcal{E}}}+ik. \tag{C.13}$$

This formula can be simplified near a resonant frequency $\tilde{\omega}_0$ fulfilling the resonance condition

$$\mathcal{E}=-\frac{1}{a_1^2}+|n|\hbar\tilde{\omega}_0. \tag{C.14}$$

We approximate the square root by a linear expression

$$\sqrt{|n|\hbar\tilde{\omega}-\mathcal{E}}=\sqrt{|n|\hbar(\tilde{\omega}-\tilde{\omega}_0)+\frac{1}{a_1^2}}\approx\frac{1}{a_1}+\frac{a_1|n|\hbar}{2}(\tilde{\omega}-\tilde{\omega}_0). \tag{C.15}$$

In this case the inverse scattering amplitude can be brought to the form

$$-\frac{1}{f}=\frac{1}{a_{\mathrm{BG}}}\frac{\tilde{\omega}-\tilde{\omega}_0}{\tilde{\omega}-\tilde{\omega}_0-\delta/\hbar}+i\gamma, \tag{C.16}$$

where we have introduced by

$$a_{\mathrm{BG}}=a_0\left(1-\frac{a_{\mathrm{WW}}^2}{a_0a_1}\right), \tag{C.17}$$

the background scattering length, which determines the scattering amplitude in the case of an infinitely large frequency ω. The width of the real part of the scattering amplitude corresponds to

$$\delta=\frac{2a_{\mathrm{WW}}^2}{a_0a_1|n|}\frac{1}{1-\frac{a_{\mathrm{WW}}^2}{a_0a_1}}\frac{1}{a_1^2}. \tag{C.18}$$

The quantity

$$\gamma=k \tag{C.19}$$

characterises the width of the imaginary part and its inverse corresponds to the maximal value of the scattering amplitude. Although having a much simpler structure than (C.11), Figure C.2 shows that the approximation (C.13) fits quite well to the correct value of (C.11). Formula (C.13) has been reported recently by [80], but without the derivation above.

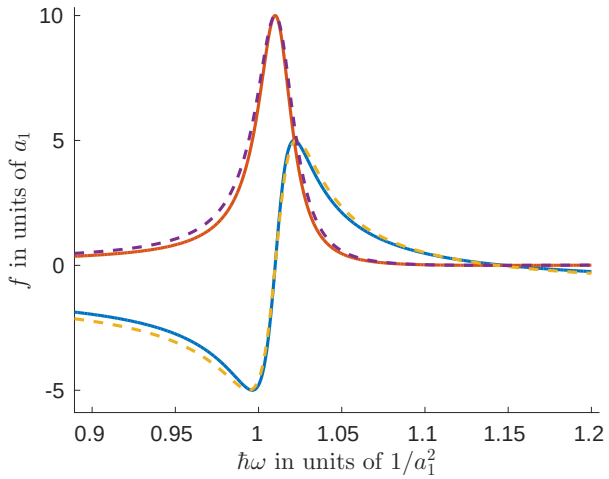

Figure C.2.: Comparison of real (blue) and imaginary (red) part of the scattering amplitude (C.12) with real (yellow dashed) and imaginary (purple dashed) part of approximate formula (C.16). This plot shows the case of $\mathcal{E} = 0.01/a_1^2$, $a_{\mathrm{WW}} = 0.25a_1$ and $a_0 = a_1$.

D. Limit of Vanishing γ of Approximative Formula (7.54)

In this Section we evaluate the limit of γ going to 0 of the formula (7.54). For the real part (7.63) the limit can be straight-forwardly evaluated to

$$-\lim_{\gamma\to 0}\mathrm{Re}\ f = a_{\mathrm{BG}}\left(1-\frac{\delta}{\hbar\tilde{\omega}-\hbar\tilde{\omega}_0}\right). \tag{D.1}$$

This equals to the limit of $\Gamma\to 0$ of equation (7.43), if we identify $a_{\mathrm{bg}}=a_{\mathrm{BG}}$ and $\Delta=\delta$. The imaginary part (7.64) converges in this limit to a Dirac-delta function, which is peaked at the resonance frequency $\tilde{\omega}_0$. This can be made clear by showing that the quantity $-\mathrm{Im}\ f(\tilde{\omega})$ fulfils the properties of the delta distribution in this limit. These are [123]

$$\delta(x)=\begin{cases}0,\ \forall x\neq 0\\ \infty,\ x=0\end{cases} \tag{D.2}$$

and

$$\int_{-\infty}^{\infty}dx\delta(x)=1. \tag{D.3}$$

We start with (D.2) and let $x=\tilde{\omega}-\tilde{\omega}_0$ be unequal to zero. Then the imaginary part of the scattering amplitude evaluates to

$$\mathrm{Im}\ f(\tilde{\omega})=\frac{\gamma a_{\mathrm{BG}}^2(x-\delta)^2}{\gamma^2 a_{\mathrm{BG}}^2(x-\delta)^2+x^2}+\frac{\gamma a_{\mathrm{BG}}^2}{1+\gamma^2 a_{\mathrm{BG}}^2}. \tag{D.4}$$

The last term equals $\mathrm{Im}\ \tilde{f}_0(\infty)$ and the whole imaginary part (D.4) vanishes in the limit $\gamma\to 0$ if $\tilde{\omega}\neq\tilde{\omega}_0$. For the case of $\tilde{\omega}=\tilde{\omega}_0$ the imaginary part (D.4) equals $1/\gamma$, which tends to infinity for vanishing γ.

The proof of condition (D.3) is a bit more involved, as it includes an integration over a non-trivial function. The integral $\int_{-\infty}^{\infty}d\tilde{\omega}\,[-\mathrm{Im}\ f(\tilde{\omega})+\mathrm{Im}\ f(\infty)]$ can be evaluated using partial integration to

$$\begin{aligned}&\int_{-\infty}^{\infty}d\tilde{\omega}\,[-\mathrm{Im}\ f(\tilde{\omega})+\mathrm{Im}\ f(\infty)]\\ &=\lim_{R\to\infty}-a_{\mathrm{BG}}^2\gamma\frac{\delta\left(-\sqrt{c}\log\left[c(\delta-x)^2+x^2\right]-(c-1)\arctan\left(\frac{c(x-\delta)+x}{\sqrt{c}\delta}\right)\right)}{\sqrt{c}(c+1)^2}\Bigg|_{-R}^{R}\\ &=-a_{\mathrm{BG}}\pi|\delta|\frac{1-c}{(1+c)^2}.\end{aligned} \tag{D.5}$$

Here we introduced the abbreviation $c = \gamma^2 a_{\mathrm{BG}}^2$ and added Im $f(\infty)$, which is zero in the case of vanishing γ and does therefore not contribute to the result. Equation (D.5) evaluates in the limit of vanishing γ to

$$-\lim_{\gamma \to 0} a_{\mathrm{BG}} \pi |\delta| \frac{1-c}{(1+c)^2} = -a_{\mathrm{BG}} |\delta| \pi. \tag{D.6}$$

Using the delta-distribution definition (D.3) we conclude that

$$-\lim_{\gamma \to 0} \mathrm{Im}\ f(\tilde{\omega}) = -a_{\mathrm{BG}} |\delta| \pi \delta(\tilde{\omega} - \tilde{\omega}_0). \tag{D.7}$$

This also equals the expression in the limit of vanishing Γ (7.49) in the case of equation (7.43) in the case of $\delta > 0$.

E. Gross-Pitaevskii Equation with Time Dependent Interaction Strength

E.1. Derivation of a Gross-Pitaevskii Equation

In this Appendix we derive the Gross-Pitaevskii equation in the case of a time-periodic inter-particle interaction $V(\mathbf{r},t)$. The Gross-Pitaevskii equation describes an interacting non-uniform and dilute Bose-Einstein condensate in mean-field approximation. Following [59], we start with the many-body Hamiltonian

$$\begin{aligned}\hat{H} = &\int d^3r \left(\frac{\hbar^2}{2m} \boldsymbol{\nabla}\hat{\Psi}^\dagger(\mathbf{r},t)\boldsymbol{\nabla}\hat{\Psi}(\mathbf{r},t) + \hat{\Psi}^\dagger(\mathbf{r},t)V_{\text{ext}}(\mathbf{r})\hat{\Psi}(\mathbf{r},t) \right) \\ &+\frac{1}{2}\int\int d^3r' d^3r \hat{\Psi}^\dagger(\mathbf{r},t)\hat{\Psi}^\dagger(\mathbf{r}',t)V(\mathbf{r}-\mathbf{r}',t)\hat{\Psi}(\mathbf{r},t)\hat{\Psi}(\mathbf{r}',t).\end{aligned} \tag{E.1}$$

The first part describes the kinetic energy of the gas and a possible external potential $V_{\text{ext}}(\mathbf{r})$, whereas the second one takes account of two-particle interactions with the inter-particle potential $V(\mathbf{y},t)$. It is assumed to be time-periodic with period T. In the further derivation we assume the condensate to be dilute. The diluteness at low temperature can be quantified by the condition

$$|a|n^{\frac{1}{3}} \ll 1. \tag{E.2}$$

The quantity $|a|n^{\frac{1}{3}}$ is called the gas parameter and it includes the density of the gas n and the s-wave scattering length a. Additionally the inequality

$$ka \ll 1 \tag{E.3}$$

for the wave vector k holds in the case of small temperatures. The Gross-Pitaevskii equation can be derived from the corresponding Heisenberg equation following from (E.1) for the field operator:

$$i\hbar\frac{\partial}{\partial t}\hat{\Psi}(\mathbf{r},t) = \left[-\frac{\hbar^2}{2m}\Delta + V_{\text{ext}}(\mathbf{r}) + \int d^3r' \hat{\Psi}^\dagger(\mathbf{r}',t)V(\mathbf{r}-\mathbf{r}',t)\hat{\Psi}(\mathbf{r}',t) \right] \hat{\Psi}(\mathbf{r},t). \tag{E.4}$$

The crucial point lies in the two-particle interaction: At low energies the wavelength of the particles is much larger than the range of the inter-atomic potential. Therefore the explicit form of the potential is not important, we can replace it by an effective or a pseudo potential leading to the same scattering length. An example is the contact interaction

$$V(\mathbf{y},t) = g(t)\delta(\mathbf{y}), \tag{E.5}$$

where the interaction strength is given by $g(t) = \int d^3r V(\mathbf{r}, t)$. We further assume that both potential and interaction strength can be written as a Fourier series. Instead of using the original Born approximation [52], we introduce the Floquet-Born approximation in zeroth order. Starting point is the assumption of $|\phi^n\rangle = \delta_{n,0}|k\rangle$ in [80, (5.10)], which connects the Fourier components of $g(t)$ to the Floquet-scattering length (5.59) by

$$g_n = \frac{2\pi\hbar^2 a_n^{\mathrm{Fl}}}{\mu}, \tag{E.6}$$

where μ is the effective mass of the particles and a_n^{Fl} the Floquet-scattering length of the n-th channel. The effective potential (E.5) is inserted into equation (E.4) and the quantum operator $\hat{\Psi}(\mathbf{r}, t)$ is replaced by the classical field $\Phi_0(r)$ in order to derive the Gross-Pitaevskii equation [59] for a time-periodic interaction potential

$$i\hbar\frac{\partial}{\partial t}\Phi_0(r,t) = \left(-\frac{\hbar^2}{2m}\Delta + V_{\mathrm{ext}}(r) + g(t)|\Phi_0(r,t)|^2\right)\Phi_0(r,t). \tag{E.7}$$

The Gross-Pitaevskii equation has the form of the Schrödinger equation with an additional nonlinear term stemming from the two-body interactions. As a time-periodic potential implies a time-periodic Floquet-scattering length, this non-linearity is time-dependent. As we show in Chapter 7 and 8 that the driving induced scattering resonance is in a good approximation lossless, it is a valid approximation to consider only the time averaged Floquet scattering length $a_{\mathrm{scatt}} = a_0^{\mathrm{Fl}}$ as the interaction strength in equation (E.7)

$$g(t) \approx \frac{2\pi\hbar^2}{\mu} a_{\mathrm{scatt}}(\omega). \tag{E.8}$$

Therefore $g(t)$ gets constant in this approximation and is tunable by the frequency ω of the periodic driving.

E.2. Continuity Equation and Effect of Imaginary Scattering Length

The similarity to the Schrödinger equation permits us to calculate the continuity equation of the Gross-Pitaevskii equation (E.7), which is capable of describing the effect of a complex scattering length a_{scatt} as occurring in Chapter 8. The starting point of the deviation is to calculate the time derivative of the local density $\frac{\partial}{\partial t}n(r,t) = \frac{\partial}{\partial t}|\Phi_0(r,t)|^2 = \Phi_0^*(r,t)\frac{\partial}{\partial t}\Phi_0(r,t) + \frac{\partial}{\partial t}\Phi_0^*(r,t)\Phi_0(r,t)$ and to replace the time derivative of the order parameter by the right-hand side of the Gross-Pitaevskii equation. The calculation is straightforward and results in the continuity equation for a Bose-Einstein condensate

$$\frac{\partial}{\partial t}n(r,t) = -\boldsymbol{\nabla}\mathbf{j}(r,t) + \frac{8\pi\hbar\ \mathrm{Im}\ a_{\mathrm{scatt}}}{\mu}n^2(r,t), \tag{E.9}$$

where the current density is given by

$$\mathbf{j} = -\frac{i\hbar}{2m}(\Phi_0^*\boldsymbol{\nabla}\Phi_0 - \Phi_0\boldsymbol{\nabla}\Phi_0^*). \tag{E.10}$$

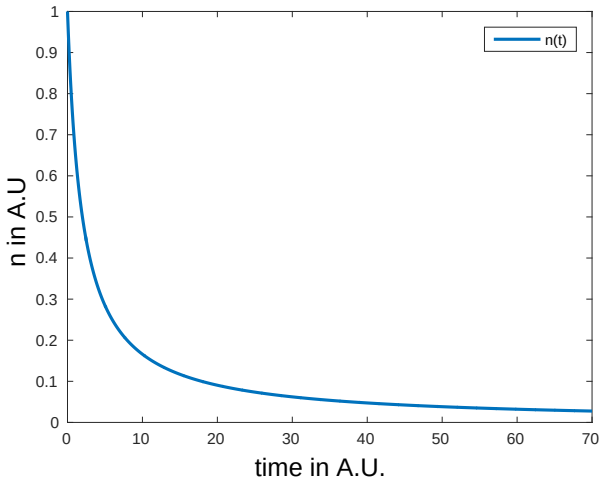

Figure E.1.: Plot of the homogeneous condensate density over the time with the values $\frac{\hbar a}{\mu} = -1$ and $n_0 = 1$.

Equation (E.9) states that the density of a Bose-Einstein condensate in a volume can be changed by either a current flow through its surface or a decay due to an imaginary part of the scattering length a_{scatt}. The decay rate is proportional to the imaginary part of the scattering length and the square of the density of the condensate. This can be made visible in the case of a homogeneous density in equation (E.9). As the current vanishes in this case and the space dependency can be dropped, equation (E.9) simplifies to the ordinary differential equation

$$\frac{\partial}{\partial t} n(t) = \frac{8\pi\hbar \text{ Im } a_{\text{scatt}}}{\mu} n^2(t). \tag{E.11}$$

The solution of this equation is derived straightforwardly by using the method of separation of variables to

$$n(t) = \frac{1}{\frac{1}{n_0} - \frac{8\pi\hbar \text{ Im } a_{\text{scatt}}}{\mu}(t - t_0)}. \tag{E.12}$$

Here n_0 describes the density at initial time t_0. As due to the optical theorem the imaginary part of the scattering length is negative, (E.12) converges to zero for large times. A plot of equation (E.12) is seen in Figure E.1. Here the shape of the decay due to the imaginary part of the scattering length is visible.

Bibliography

[1] S. E. Pollack, D. Dries, R. G. Hulet, K. M. F. Magalhães, E. A. L. Henn, E. R. F. Ramos, M. A. Caracanhas, and V. S. Bagnato. *Collective excitation of a Bose-Einstein condensate by modulation of the atomic scattering length.* Phys. Rev. A **81** 053627 (2010).

[2] L. W. Clark, A. Gaj, L. Feng, and C. Chin. *Collective emission of matter-wave jets from driven Bose-Einstein condensates.* Nature Publishing Group **551** 356–359 (2017).

[3] D. H. Smith. *Inducing Resonant Interactions in Ultracold Atoms with a Modulated Magnetic Field.* Phys. Rev. Lett **115** 193002 (2015).

[4] A. G. Sykes, H. Landa, and D. S. Petrov. *Two- and three-body problem with Floquet-driven zero-range interactions.* Phys. Rev. A **95** 062705 (2017).

[5] D. Thuberg, S. A. Reyes, and S. Eggert. *Quantum resonance catastrophe for conductance through a periodically driven barrier.* Phys. Rev. B **93** 180301 (2016).

[6] L. Dimou and F. H. M. Faisal. *New class of resonance in the $e + H^+$ scattering in an excimer laser field.* Phys. Rev. Lett. **59** 872–875 (1987).

[7] H. Xian-Quan, X. Jie, L. Guang, and M. Yan. *Introduction of the Coulomb dressed potential into atomic scattering.* Chin. Chys. **16** 3631 (2007).

[8] A. Emmanouilidou and L. E. Reichl. *Floquet scattering and classical-quantum correspondence in strong time-periodic fields.* Phys. Rev. A **65** 033405 (2002).

[9] M. Terao-Dunseath and K. M. Dunseath. *R -matrix Floquet theory for laser-assisted electron-atom scattering.* J. Phys B **35** 125 (2002).

[10] L. P. Rapoport and A. S. Kornev. *Resonances and dichroism in the scattering of an electron in an intense laser field by the Coulomb potential.* Journal of Experimental and Theoretical Physics **89** 664–668 (1999).

[11] P. Kapitza. *Dynamic stability of a pendulum when its point of suspension vibrates.* Sov. Phys. JETP **21** 588–592 ((1951)).

[12] P. Kapitza. *Pendulum with a vibrating suspension.* Usp. Fiz. Nauk **44** 7–15 (1951).

[13] M. E. Semenov, D. V. Shevlyakova, and P. A. Meleshenko. *Inverted pendulum under hysteretic control: Stability zones and periodic solutions.* Nonlinear Dynamics **75** 247–256 (2014).

[14] N. Ashcroft and N. Mermin. *Solid state physics.* Cengage Learning (2008).

[15] N. Goldman and J. Dalibard. *Periodically driven quantum systems: Effective Hamiltonians and engineered gauge fields.* Phys. Rev. X **4** 1–29 (2014).

[16] A. Eckardt, C. Weiss, and M. Holthaus. *Superfluid-Insulator Transition in a Periodically Driven Optical Lattice.* Phys. Rev. Lett. **95** 260404 (2005).

[17] A. Eckardt and M. Holthaus. *AC-induced superfluidity.* Europhys. Lett. **80** 50004 (2007).

[18] A. Zenesini, H. Lignier, D. Ciampini, O. Morsch, and E. Arimondo. *Coherent Control of Dressed Matter Waves.* Phys. Rev. Lett. **102** 100403 (2009).

[19] Dunlap, D. H. and Kenkre, V. M. *Dynamic localization of a charged particle moving under the influence of an electric field.* Phys. Rev. B **34** 3625 (1986).

[20] B. J. Keay, S. Zeuner, S. J. Allen, K. D. Maranowski, A. C. Gossard, U. Bhattacharya, and M. J. W. Rodwell. *Dynamic Localization, Absolute Negative Conductance, and Stimulated, Multiphoton Emission in Sequential Resonant Tunneling Semiconductor Superlattices.* Phys. Rev. Lett. **75** 4102–4105 (1995).

[21] G. Lenz, R. Parker, M. Wanke, and C. de Sterke. *Dynamical localization and AC Bloch oscillations in periodic optical waveguide arrays.* Optics Communications **218** 87 – 92 (2003).

[22] F. Dreisow, M. Heinrich, A. Szameit, S. Döering, S. Nolte, A. Tüennermann, S. Fahr, and F. Lederer. *Spectral resolved dynamic localization in curved fs laser written waveguide arrays.* Optics express **16** 3474–3483 (2008).

[23] H. Lignier, C. Sias, D. Ciampini, Y. Singh, A. Zenesini, O. Morsch, and E. Arimondo. *Dynamical Control of Matter-Wave Tunneling in Periodic Potentials.* Phys. Rev. Lett. **99** 220403 (2007).

[24] C. Sias, H. Lignier, Y. P. Singh, A. Zenesini, D. Ciampini, O. Morsch, and E. Arimondo. *Observation of Photon-Assisted Tunneling in Optical Lattices.* Phys. Rev. Lett. **100** 040404 (2008).

[25] A. Eckardt, M. Holthaus, H. Lignier, A. Zenesini, D. Ciampini, O. Morsch, and E. Arimondo. *Exploring dynamic localization with a Bose-Einstein condensate.* Phys. Rev. A **79** 013611 (2009).

[26] G. Jotzu, M. Messer, R. Desbuquois, M. Lebrat, T. Uehlinger, D. Greif, and T. Esslinger.

Experimental realization of the topological Haldane model with ultracold fermions. Nature **515** 237–240 (2014).

[27] N. Fläschner, D. Vogel, M. Tarnowski, B. S. Rem, D. S. Lühmann, M. Heyl, J. C. Budich, L. Mathey, K. Sengstock, and C. Weitenberg. *Observation of dynamical vortices after quenches in a system with topology*. Nature Physics **14** 1–4 (2017).

[28] B. Wang, F. N. Unal, and A. Eckardt. *Floquet engineering of optical solenoids and quantized charge pumping along tailored paths in two-dimensional Chern insulators*. arXiv:1802.06815 (2018).

[29] J. Struck, C. Ölschläger, M. Weinberg, P. Hauke, J. Simonet, A. Eckardt, M. Lewenstein, K. Sengstock, and P. Windpassinger. *Tunable Gauge Potential for Neutral and Spinless Particles in Driven Optical Lattices*. Phys. Rev. Lett. **108** 225304 (2012).

[30] P. Hauke, O. Tieleman, A. Celi, C. Ölschläger, J. Simonet, J. Struck, M. Weinberg, P. Windpassinger, K. Sengstock, M. Lewenstein, and A. Eckardt. *Non-Abelian Gauge Fields and Topological Insulators in Shaken Optical Lattices*. Phys. Rev. Lett. **109** 145301 (2012).

[31] A. Eckardt. *Colloquium: Atomic quantum gases in periodically driven optical lattices*. Rev. Mod. Phys. **89** 1–30 (2017).

[32] M. Grifoni and P. Hänggi. *Driven quantum tunneling*. Phys. Rep. **304** 229–354 (1998).

[33] M. Holthaus. *Floquet engineering with quasienergy bands of periodically driven optical lattices*. J. Phys. B **49** 013001 (2016).

[34] J. J. O´ Connor and E. F. Robertson. *Gaston Floquet*. In *MacTutor History of Mathematics archive*. JOC/EFR, http://www-history.mcs.st-andrews.ac.uk/Biographies/Floquet.html (2005).

[35] G. Floquet. *Sur les équations différentielles linéaires à coefficients périodiques*. Annales scientifiques de l´École Normale Supérieure **12** 47–88 (1883).

[36] H. Sambe. *Steady states and quasienergies of a quantum-mechanical system in an oscillating field*. Phys. Rev. A **7** 2203–2213 (1973).

[37] I. Bloch, J. Dalibard, and W. Zwerger. *Many-body physics with ultracold gases*. Rev. Mod. Phys. **80** 885–964 (2008).

[38] C. Chin, R. Grimm, P. Julienne, and E. Tiesinga. *Feshbach resonances in ultracold gases*. Rev. Mod. Phys. **82** 1225–1286 (2010).

[39] I. Bloch. *Ultracold quantum gases in optical lattices*. Nature Physics **1** 23–30 (2005).

[40] C. C. Bradley, C. A. Sackett, and R. G. Hulet. *Bose-Einstein Condensation of Lithium: Observation of Limited Condensate Number.* Phys. Rev. Lett. **78** 985–989 (1997).

[41] S. L. Cornish, N. R. Claussen, J. L. Roberts, E. A. Cornell, and C. E. Wieman. *Stable* ^{85}Rb *Bose-Einstein Condensates with Widely Tunable Interactions.* Phys. Rev. Lett. **85** 1795–1798 (2000).

[42] T. Bourdel, L. Khaykovich, J. Cubizolles, J. Zhang, F. Chevy, M. Teichmann, L. Tarruell, S. J. J. M. F. Kokkelmans, and C. Salomon. *Experimental Study of the BEC-BCS Crossover Region in Lithium 6.* Phys. Rev. Lett. **93** 050401 (2004).

[43] M. Bartenstein, A. Altmeyer, S. Riedl, S. Jochim, C. Chin, J. H. Denschlag, and R. Grimm. *Crossover from a Molecular Bose-Einstein Condensate to a Degenerate Fermi Gas.* Phys. Rev. Lett. **92** 120401 (2004).

[44] Q. Chen, J. Stajic, S. Tan, and K. Levin. *BCS-BEC crossover: From high temperature superconductors to ultracold superfluids.* Phys. Rep **412** 1 – 88 (2005).

[45] E. A. Donley, N. R. Claussen, S. T. Thompson, and C. E. Wieman. *Atom-molecule coherence in a Bose-Einstein condensate.* Nature **417** 529–533 (2002).

[46] S. T. Thompson, E. Hodby, and C. E. Wieman. *Ultracold Molecule Production via a Resonant Oscillating Magnetic Field.* Phys. Rev. Lett. **95** 190404 (2005).

[47] W. Cairncross and A. Pelster. *Parametric resonance in Bose-Einstein condensates with periodic modulation of attractive interaction.* Europhys. J. D **68** 106 (2014).

[48] I. Vidanović, A. Balaž, H. Al-Jibbouri, and A. Pelster. *Nonlinear Bose-Einstein-condensate dynamics induced by a harmonic modulation of the s-wave scattering length.* Phys. Rev. A **84** 013618 (2011).

[49] S. A. Reyes, D. Thuberg, D. Pérez, C. Dauer, and S. Eggert. *Transport through an AC-driven impurity: Fano interference and bound states in the continuum.* New J. Phys. **19** 043029 (2017).

[50] U. Fano. *Effects of Configuration Interaction on Intensities and Phase Shifts.* Phys. Rev. **124** 1866–1878 (1961).

[51] A. E. Miroshnichenko and Y. S. Kivshar. *Engineering Fano resonances in discrete arrays.* Phys. Rev. E **72** 056611 (2005).

[52] C. Pethick and H. Smith. *Bose-Einstein Condensation in Dilute Gases.* Cambridge University Press (2002).

[53] C. Timm. *Quantentheorie 2.* TU Dresden, Institut für Theoretische Physik (2015). Abgerufen am 29.09.2017, 12:18.

[54] H. Korsch. *Mathematische Ergänzungen zur Einführung in die Physik.* Binomi (2004).

[55] A. Pelster. *Bose-Einstein-Kondensation.* Universität Duisburg-Essen, http://users.physik.fu-berlin.de/ pelster/Vorlesungen/WS1213/bec.pdf (2004).

[56] H. Friedrich. *Scattering Theory.* Springer Berlin Heidelberg (2015).

[57] N. Mott and H. Massey. *The Theory of Atomic Collisions, by N.F. Mott and H.S.W. Massey. 3rd Edition.* Clarendon Press (1965).

[58] R. Newton. *Scattering theory of waves and particles.* International series in pure and applied physics. McGraw-Hill (1966).

[59] L. Pitaevskii and S. Stringari. *Bose-Einstein Condensation.* International Series of Monographs on Physics. Clarendon Press (2003).

[60] B. Bransden and C. Joachain. *Physics of Atoms and Molecules.* Pearson Education. Prentice Hall (2003).

[61] H. Feshbach. *Unified theory of nuclear reactions.* Ann. Phys. (New York) **5** 357 390 (1958).

[62] H. Feshbach. *A unified theory of nuclear reactions. II.* Ann. Phys. (New York) **19** 287–313 (1962).

[63] A. J. Moerdijk, B. J. Verhaar, and A. Axelsson. *Resonances in ultracold collisions of* ^{6}Li, ^{7}Li, *and* ^{23}Na. Phys. Rev. A **51** 4852–4861 (1995).

[64] E. Timmermans, P. Tommasini, M. Hussein, and A. Kerman. *Feshbach resonances in atomic Bose-Einstein condensates.* Phys. Rep. **315** 199 – 230 (1999).

[65] S. Inouye, M. R. Andrews, J. Stenger, H.-J. Miesner, D. M. Stamper-Kurn, and W. Ketterle. *Observation of Feshbach resonances in a Bose-Einstein condensate.* Nature **392** 151 (1998).

[66] P. Courteille, R. S. Freeland, D. J. Heinzen, F. A. van Abeelen, and B. J. Verhaar. *Observation of a Feshbach Resonance in Cold Atom Scattering.* Phys. Rev. Lett. **81** 69–72 (1998).

[67] P. O. Fedichev, Y. Kagan, G. V. Shlyapnikov, and J. T. M. Walraven. *Influence of Nearly Resonant Light on the Scattering Length in Low-Temperature Atomic Gases.* Phys. Rev. Lett. **77** 2913–2916 (1996).

[68] F. K. Fatemi, K. M. Jones, and P. D. Lett. *Observation of Optically Induced Feshbach Resonances in Collisions of Cold Atoms.* Phys. Rev. Lett. **85** 4462–4465 (2000).

[69] O. Thomas, C. Lippe, T. Eichert, and H. Ott. *Experimental realization of a Rydberg optical Feshbach resonance in a quantum many-body system.* arXiv:1712.05263 (2017).

[70] M. Theis, G. Thalhammer, K. Winkler, M. Hellwig, G. Ruff, R. Grimm, and J. H. Denschlag. *Tuning the Scattering Length with an Optically Induced Feshbach Resonance.* Phys. Rev. Lett. **93** 123001 (2004).

[71] A. J. Moerdijk, B. J. Verhaar, and T. M. Nagtegaal. *Collisions of dressed ground-state atoms.* Phys. Rev. A **53** 4343 (1996).

[72] A. M. Kaufman, R. P. Anderson, T. M. Hanna, E. Tiesinga, P. S. Julienne, and D. S. Hall. *Radio-frequency dressing of multiple Feshbach resonances.* Phys. Rev. A **80** 050701 (2009).

[73] S. V. Alyabyshev, T. V. Tscherbul, and R. V. Krems. *Microwave-laser-field modification of molecular collisions at low temperatures.* Phys. Rev. A **79** 060703 (2009).

[74] T. M. Hanna, E. Tiesinga, and P. S. Julienne. *Creation and manipulation of Feshbach resonances with radio-frequency radiation.* New J. Phys. **12** (2010).

[75] T. V. Tscherbul, T. Calarco, I. Lesanovsky, R. V. Krems, A. Dalgarno, and J. Schmiedmayer. *RF-field-induced Feshbach resonances.* Phys. Rev. A **81** 1–4 (2010).

[76] T. Xie, G.-R. Wang, Y. Huang, W. Zhang, and S.-L. Cong. *The radio frequency field modulation of magnetically induced heteronuclear Feshbach resonance.* J. Phys. B **45** 145302 (2012).

[77] D. J. Papoular, G. V. Shlyapnikov, and J. Dalibard. *Microwave-induced Fano-Feshbach resonances.* Phys. Rev. A **81** 041603 (2010).

[78] D. J. Owens, T. Xie, and J. M. Hutson. *Creating Feshbach resonances for ultracold molecule formation with radio-frequency fields.* Phys. Rev. A **94** 023619 (2016).

[79] Y. Ding, J. P. D'Incao, and C. H. Greene. *Effective control of cold collisions with radio-frequency fields.* Phys. Rev. A **95** 022709 (2017).

[80] D. H. Smith. *Resonant Floquet scattering of ultracold atoms.* Ph.D. thesis, The Ohio State University (2016).

[81] A. Mohapatra and E. Braaten. *Harmonic and subharmonic association of universal dimers in a thermal gas.* Phys. Rev. A **92** 013425 (2015).

[82] T. Dittrich. *Quantum transport and dissipation.* Wiley-VCH (1998).

[83] H. Ibach, Harald; Lüth. *Festkörperphysik*. Springer Verlag Heidelberg, 7 edition (2009).

[84] R. Shankar. *Principles of Quantum Mechanics*. Springer US, 2. edition edition (2008).

[85] M. Abramowitz and I. A. Stegun, editors. *Handbook of Mathematical Functions with Formulas, Graphs, and Mathematical Tables*. New York: Dover, 9th printing edition (1972).

[86] J. R. Taylor. *Scatterning Theory: The Quantum Theory on Nonrelativistic Collisions*. John Wiley & Sons, Inc. (1972).

[87] A. Russomanno and G. E. Santoro. *Floquet resonances close to the adiabatic limit and the effect of dissipation*. J Stat. Mech. **2017** 103104 (2017).

[88] H. Haken. *Laser Theory*. Springer Berlin Heidelberg (1970).

[89] *MATLAB Documentary: Backslash Operator*. https://de.mathworks.com/help/matlab/ref/mldivide

[90] D. Thuberg. *AC-Driven Impurities in Nanoscale Systems*. Ph.D. thesis, Pontifical Catholic University of Chile, Institute of Physics (2017).

[91] C. W. Hsu, B. Zhen, A. D. Stone, J. D. Joannopoulos, and M. Soljačić. *Bound states in the continuum*. Nature Rev. Mat. **1** 16048 (2016).

[92] J. von Neumann and E. Wigner. *Über Merkwurdige Diskrete Eigenwerte*. Phys. Z. **30** 465–467 (1929).

[93] F. H. Stillinger and D. R. Herrick. *Bound states in the continuum*. Phys. Rev. A **11** 446–454 (1975).

[94] H. Friedrich and D. Wintgen. *Physical realization of bound states in the continuum*. Phys. Rev. A **31** 3964–3966 (1985).

[95] H. Friedrich and D. Wintgen. *Interfering resonances and bound states in the continuum*. Phys. Rev. A **32** 3231–3242 (1985).

[96] C. González-Santander, P. A. Orellana, and F. Domínguez-Adame. *Bound states in the continuum driven by AC fields*. Europhys. Lett. **102** 17012 (2013).

[97] S. Longhi and G. D. Valle. *Floquet bound states in the continuum*. Scient. Rep. **3** (2013).

[98] P. F. Bagwell and R. K. Lake. *Resonances in transmission through an oscillating barrier*. Phys. Rev. B **46** 15329–15336 (1992).

[99] D. F. Martinez and L. E. Reichl. *Transmission properties of the oscillating δ-function potential.* Phys. Rev. B **64** 245315 (2001).

[100] *MATLAB Documentary: Evaluating Goodness of Fit.* https://de.mathworks.com/help/curvefit/evaluating-goodness-of-fit.html.

[101] E. W. Weisstein. *"Square Root." From MathWorld–A Wolfram Web Resource.*

[102] N. R. Claussen, S. J. J. M. F. Kokkelmans, S. T. Thompson, E. A. Donley, E. Hodby, and C. E. Wieman. *Very-high-precision bound-state spectroscopy near a* ^{85}Rb *Feshbach resonance.* Phys. Rev. A **67** 060701 (2003).

[103] S. Longhi. *Non-Hermitian Floquet invisibility.* Europhys. Lett. **117** 10005 (2017).

[104] D. M. Stamper-Kurn, M. R. Andrews, A. P. Chikkatur, S. Inouye, H.-J. Miesner, J. Stenger, and W. Ketterle. *Optical Confinement of a Bose-Einstein Condensate.* Phys. Rev. Lett. **80** 2027–2030 (1998).

[105] Y. Kawaguchi and M. Ueda. *Spinor Bose-Einstein condensates.* Phys. Rep. **520** 253 – 381 (2012). Spinor Bose–Einstein condensates.

[106] L. . E. Sadler, J. M. Higbie, S. R. Leslie, M. Vengalattore, and D. M. Stamper-Kurn. *Spontaneous symmetry breaking in a quenched ferromagnetic spinor Bose-Einstein condensate*. Nature 5 **443** 312–315 (2006).

[107] F. Schmidt, D. Mayer, Q. Bouton, D. Adam, T. Lausch, N. Spethmann, and A. Widera. *Quantum spin dynamics of individual neutral impurities coupled to a Bose-Einstein condensate*. arXiv:1802.08702v1 (2018).

[108] F. Schmidt. *Private Communications.* TU Kaiserslautern, AG Widera (2018).

[109] P. Soltan-Panahi. *Thermodynamic Properties of F=1 Spinor Bose-Einstein Condensates.* Diplomarbeit, Freien Universität Berlin (2006).

[110] C. Jörg, F. Letscher, M. Fleischhauer, and G. von Freymann. *Dynamic defects in photonic Floquet topological insulators.* New J. Phys. **19** 083003 (2017).

[111] C. Jörg. *Erste Schritte in Richtung optischer topologischer Isolatoren durch direktes Laserschreiben.* Diplomarbeit, Technische Universität Kaiserslautern (2015).

[112] F. Bleckmann, Z. Cherpakova, S. Linden, and A. Alberti. *Spectral imaging of topological edge states in plasmonic waveguide arrays.* Phys. Rev. B **96** 045417 (2017).

[113] M. C. Rechtsman, J. M. Zeuner, Y. Plotnik, Y. Lumer, D. Podolsky, F. Dreisow, S. Nolte, M. Segev, and A. Szameit. *Photonic Floquet topological insulators.* Nature **496** 196–200 (2013).

[114] F. Letscher. *Topologische Zustände in Bosonischen Gittermodellen.* Diplomarbeit, Technische Universität Kaiserslautern (2014).

[115] C. Jörg and F. Letscher. *Privat Communications.* Technische Universität Kaiserslautern, AG von Freymann and AG Fleischhauer (2018).

[116] J. K. Asbóth, L. Oroszlány, and A. Pályi. *A Short Course on Topological Insulators.* Springer International Publishing (2016).

[117] Z. Cherpakova, C. Jörg, C. Dauer, F. Letscher, M. Fleischhauer, S. Eggert, S. Linden, and G. von Freymann. *Private Communications* (2018).

[118] G. Breit. *The Scattering of Slow Neutrons by Bound Protons. I. Methods of Calculation.* Phys. Rev. **71** 215–231 (1947).

[119] K. Huang and C. N. Yang. *Quantum-Mechanical Many-Body Problem with Hard-Sphere Interaction.* Phys. Rev. **105** 767–775 (1957).

[120] A. Zangwill. *Modern Electrodynamics.* Modern Electrodynamics. Cambridge University Press (2013).

[121] K. R. Waters, J. Mobley, and J. G. Miller. *Causality-imposed (Kramers-Kronig) relationships between attenuation and dispersion.* IEEE Transactions on Ultrasonics, Ferroelectrics, and Frequency Control **52** 822–833 (2005).

[122] V. Lucarini, J. Saarinen, K. Peiponen, and E. Vartiainen. *Kramers-Kronig Relations in Optical Materials Research.* Springer Series in Optical Sciences. Springer Berlin Heidelberg (2006).

[123] A. Messiah. *Quantenmechanik.* Walter de Gruyter, 1. edition (1976).

Acknowledgement

At this point I want to say thanks to people, who supported me during my studies. At first I want to show my gratitude to Prof. Dr. Sebastian Eggert for the deep discussions and the supervision, which helped me to find a good path. I also want to thank Priv. Doz. Dr. habil. Axel Pelster for his great support, his fast answer to questions, the large amount of helpful discussions and his huge enthusiasm, which encouraged me during the time of the thesis. I also thank Dr. Imke Scheider for her helpful opinion in discussions. I thank all members of the group Eggert for the inspiring discussions and fast and helpful answer of questions that occurred. I want to thank Hamidreza Kazemi, Martin Bonkhoff, Polina Matveeva, Dr. Shaon Sahoo, Dr. Milan Radonjic, Dr. Shijie Hu, Enrico Stein and Kevin Jägering for being friendly colleagues.

I show my gratitude to Christina Jörg, Fabian Letscher and Zlata Cherpakova for for the initiation and valuable collaboration in a joint research project. I also want to thank Felix Schmidt, Daniel Adam and Prof. Dr. Artur Widera for the interest in my investigations, which showed up in trend-setting discussions during the time of my thesis. I also want to thank Daniel Thuberg for the valuable discussions during his visit.

I show deepest appreciation to Enrico, who I know since the beginning of my studies. We had detailed physical discussions during our studies and he helped me with many problems. I want to thank all my friends for the great time we had and the nice events we visited.

I say thanks to my parents Jutta and Günter for the never-ending support and the always open ear for my problems. I can only extend this to the whole family and thank all of them for their heartening in the last years. At last I want thank Katharina for always being on my side also in hard times.